

Determination of Supersymmetric Particle Masses at the LHC using Kinematic Fits

Dissertation

zur Erlangung des Doktorgrades

des Department Physik

der Universität Hamburg

vorgelegt von

Benedikt Mura

aus Recklinghausen

Hamburg

2011

Gutachter der Dissertation:	Prof. Dr. Peter Schleper Prof. Dr. Johannes Haller
Gutachter der Disputation:	Prof. Dr. Peter Schleper Dr. Philip Bechtle
Datum der Disputation:	02.09.2011
Vorsitzender des Prüfungsausschusses:	Dr. Georg Steinbrück
Vorsitzender des Promotionsausschusses:	Prof. Dr. Peter Hauschildt
Leiterin des Fachbereichs Physik:	Prof. Dr. Daniela Pfannkuche
Dekan der Fakultät für Mathematik, Informatik und Naturwissenschaften	Prof. Dr. Heinrich Graener

Abstract

Supersymmetry is a theoretically well-motivated extension of the currently established model of particle physics. It introduces a new symmetry between bosonic and fermionic fields and predicts a large number of new particles. If supersymmetry is discovered at the LHC, a measurement of the new particle masses will be an important contribution to the determination of the fundamental model parameters.

In this thesis a novel method for mass determination is presented, which is based on the assumption of R-parity conserving supersymmetry and makes use of events with identical decay topologies. Combining a mass scan with an event-by-event kinematic fit a complete event reconstruction is possible despite two undetected lightest supersymmetric particles, and a likelihood map for the mass space is obtained.

The method is demonstrated for the mSUGRA benchmark point SPS1a and is shown to work in principle. A weakness concerning the measurement of the undetected particle at the end of the decay chain is observed, which is related to the measurement resolution of particles in the detector. Additional information from the measurement of a kinematic endpoint is applied to improve the determination of the lightest particle mass. If backgrounds are small a precise mass measurement is feasible with this method. A large amount of LHC data is required to isolate sufficient events with a suitable topology.

Zusammenfassung

Supersymmetrie ist eine theoretisch gut motivierte Erweiterung des aktuellen Modells der Teilchenphysik und führt eine neue Symmetrie zwischen bosonischen und fermionischen Feldern ein, welche zur Vorhersage vieler neuer Teilchen führt. Im Falle einer Entdeckung von Supersymmetrie am LHC wird die Massenmessung der neuen Teilchen einen wichtigen Beitrag zur Bestimmung der grundlegenden Modellparameter bilden.

In dieser Arbeit wird eine neue Methode zur Bestimmung dieser Teilchenmassen präsentiert, welche auf der Annahme von R-Paritäts erhaltender Supersymmetrie und der Analyse von Ereignissen mit identischen Zerfallskaskaden beruht. Ein Scan über mögliche Teilchenmassen wird mit einem ereignisweisen kinematischen Fit kombiniert, wodurch eine vollständige Ereignisrekonstruktion, trotz zweier ungemessener Teilchen, möglich wird und eine Likelihoodverteilung für die Massen erstellt werden kann.

Die Methode wird am Beispiel des mSUGRA Benchmarkpunktes SPS1a demonstriert und ihre prinzipielle Funktionstüchtigkeit gezeigt. Eine Schwäche in der Messung des ungemessenen Teilchens am Ende der Kaskade wurde festgestellt, welche mit der Messauflösung von Teilchen im Detektor in Zusammenhang steht. Zusätzliche Information aus der Messung eines kinematischen Endpunktes wird genutzt um die Bestimmung der leichtesten Masse zu verbessern. Eine präzise Massenmessung ist möglich, falls der Untergrund klein ist. Es ist eine große Menge an LHC Daten notwendig, um genügend Ereignisse mit geeigneter Zerfallstopologie zu isolieren.

Contents

1. Introduction	1
2. Theory and Phenomenology of Supersymmetry	3
2.1. The Standard Model	3
2.1.1. Open Questions of the Standard Model	6
2.2. Supersymmetry	7
2.2.1. Basic Ideas	7
2.2.2. Supersymmetry Breaking	8
2.2.3. The MSSM	9
2.3. SUSY at the LHC	15
2.3.1. Event Properties in R-parity Conserving Supersymmetry	15
2.3.2. Searches for Supersymmetry	17
3. The CMS Experiment at the LHC	21
3.1. The Large Hadron Collider	21
3.1.1. The LHC Design	21
3.2. The CMS Detector	23
3.2.1. Coordinate System and Conventions	25
3.2.2. Superconducting Solenoid	25
3.2.3. Tracking Detectors	25
3.2.4. Electromagnetic Calorimeter	27
3.2.5. Hadronic Calorimeter	28
3.2.6. Forward Detectors	29
3.2.7. Muon System	30
3.2.8. Trigger System and Data Acquisition	31
3.2.9. Data Storage and Processing	32
3.3. Physics Objects Reconstruction	34
3.3.1. Jets and Missing Energy	35
3.3.2. Missing Transverse Energy	37
3.3.3. Electrons	37

3.3.4. Muons	38
3.3.5. Event Simulation	40
4. The Mass Determination Problem	41
4.1. Motivation	41
4.2. Approaches to Mass Determination	42
4.2.1. Decay Chain Reconstruction and Mass Determination	43
4.2.2. The Kinematic-Fits-Method	46
5. Physics Scenario	49
5.1. SUSY Benchmark Scenario	49
5.1.1. Suitable (Leptonic) Decay Chains	50
5.2. Simulated Events Sample	53
5.2.1. Detector Simulation Objects	54
5.2.2. Event Selection	64
5.3. Toy Detector Simulation	72
6. Kinematic Fit Implementation and Setup	75
6.1. Kinematic Fitting	75
6.1.1. Method of Lagrangian Multipliers	75
6.1.2. Momentum Parametrization	77
6.1.3. Implementation of constraints	78
6.2. Choice of Initial Values for Unmeasured Parameters	79
6.2.1. Options for Choice of Initial Values	79
6.2.2. Comparison	82
6.2.3. Conclusions	85
6.3. Error Treatment	86
6.3.1. Particle Momentum Resolutions	86
6.3.2. Mass Widths	86
7. Results	89
7.1. Validation of the Fit Algorithm	89
7.2. Combining Events	98
7.3. Visualization	100
7.4. Mass Determination	102
7.4.1. Mass Scan on Signal Events	102
7.4.2. Toy MC Study of Measurement Resolutions	109
7.4.3. Further Signal and Background Contributions	110
7.5. Inclusion of the Dilepton Mass Edge	118
7.6. Comparison to Other Studies	122

7.7. Conclusions	127
8. Summary	129
8.1. Outlook	131
A. Linearization and Iterative Solution in the Kinematic Fit	133
B. Calculations for a Two-Body-Decay	137
C. Additional Pull Distributions	145

List of Figures

2.1. Example Feynman diagrams for gluino and squark production at the LHC	16
2.2. Exclusion limits from CDF and CMS discovery reach	19
3.1. Schematic view of the LHC layout	22
3.2. Schematic view of the CMS detector	24
3.3. Cross-section through the the silicon tracker	26
3.4. ECAL quarter showing crystal orientation	28
3.5. HCAL components in CMS quarter view	29
3.6. Drawing of position and type of muon chambers	30
3.7. Architecture of the L1 trigger	32
3.8. CMS Computing Model	33
3.9. Muon p_T resolution	39
4.1. Feynman diagram of example SUSY decay chain	44
4.2. Mass determination method scheme	47
5.1. Particle mass spectrum at the SPS1a	50
5.2. Feynman diagram of signal event	52
5.3. Electron and muon isolation distribution for SPS1a	56
5.4. Lepton isolation efficiency vs. fake rate	57
5.5. Jet angular resolution	60
5.6. Electron transverse momentum and pseudorapidity resolution	61
5.7. Muon transverse momentum and pseudorapidity resolution	62
5.8. Electron and muon azimuthal angle resolution	63
5.9. Jet p_T and missing E_T spectra after preselection	66
5.10. Lepton p_T spectra after preselection	67
5.11. First and second hardest jet transverse momentum after lepton selection	68
5.12. Jet p_T and missing E_T spectra after full selection	69
5.13. Lepton p_T spectra after full selection	70
5.14. Jet transverse momentum in discarded Toy MC events	74

6.1.	Difference between true LSP momenta and starting values in the fit	83
6.2.	Initial values of kinematic constraints	84
6.3.	LSP momentum approximation in Toy MC and detector simulation	85
7.1.	Fit probability and pulls for signal events in Toy MC	91
7.2.	Determination of LSP momenta in fit with true masses in Toy MC	92
7.3.	Fit probability for signal and background including combinatorics	94
7.4.	Fit probability and pulls for signal events in detector simulation sample	96
7.5.	Determination of LSP momenta in fit with true masses	97
7.6.	Fit probability for signal and background including combinatorics	97
7.7.	Projection of 2-dimensional likelihood	101
7.8.	2D error ellipse for explanation of uncertainties.	101
7.9.	Mass scan for $\tilde{q}_L\tilde{q}_L$ signal events in detector simulation sample	106
7.10.	Dilepton invariant mass distribution on generator level	107
7.11.	Mass scan without combinatorics.	107
7.12.	Mass scan for different luminosities	108
7.13.	Missing transverse energy response in Toy MC	109
7.14.	Mass scan for different jet p_T and missing E_T resolutions in Toy MC	112
7.15.	Mass scan for \tilde{b}_1 signal events	113
7.16.	Mass scan for all signal events	114
7.17.	Mass scan for background events	115
7.18.	Mass scan for signal and background events	117
7.19.	Mass scan for signal events with dilepton mass edge requirement	120
7.20.	Mass scan for full sample with dilepton mass edge requirement	121
7.21.	Mass scan for comparison of methods in Toy MC	125
7.22.	Mass scan with reduced backgrounds for comparison of methods	126
C.1.	η and ϕ pull distributions in Toy MC	146
C.2.	η and ϕ pull distributions in detector simulation sample	147

List of Tables

2.1. Overview of particle fields in the MSSM	10
3.1. Particle-flow anti-kt jet p_T resolution parameters	37
5.1. SPS1a parameters	49
5.2. Masses of signal cascade particles	53
5.3. Values of Standard Model input parameters for Monte Carlo event generation.	54
5.4. CMS Software Object Identifiers	55
5.5. Fitted jet angular resolution parameters	58
5.6. Electron resolution parameters	59
5.7. Muon resolution parameters	59
5.8. Event selection cutflow for detector simulation sample.	65
5.9. Classification of background events	72
5.10. Toy Monte Carlo Event Selection Cuts	73
6.1. Constraint widths for kinematic fit	87
7.1. Combinatorics after kinematic fit in Toy MC	93
7.2. Combinatorics after kinematic fit in detector simulation sample	95
7.3. Confidence intervals for joint estimation of parameters	100
7.4. Grid of mass hypotheses for scan.	102
7.5. Average χ^2 at optimum of mass scan	110
7.6. Results of the mass determination using the mass edge measurement.	119
7.7. Results of the mass determination method by Webber	122
7.8. Result of the mass determination method by Cheng et al.	123
7.9. Event selection result with b-tagging emulation	124

Chapter 1

Introduction

For decades the Standard Model of particle physics has provided a precise description of all elementary particles and their interactions, observed in experiments. With the start of the Large Hadron Collider (LHC), eventually delivering proton-proton collisions at a center-of-mass energy of 14 TeV, this model is challenged again in a new energy regime. For the first time particle interactions at an energy scale in the TeV region can be studied in high numbers in a laboratory. Expectations are high that new particles signatures will be observed in the detectors of the LHC experiments, be it the long searched Higgs-boson, or more exotic phenomena, suggested by conceptual problems of the Standard Model when approaching the TeV-scale.

Among the ideas for phenomena beyond the Standard Model, Supersymmetry (SUSY) plays a prominent role. This additional symmetry relates bosonic and fermionic fields and predicts a variety of new particles, yielding a rich collider phenomenology. Many SUSY models have appealing features, like a unification of forces and a suitable candidate particle to explain the amount of dark matter found in cosmological observations.

The experimental setup at the LHC is well suited to discover supersymmetry, if it exists and has the desired properties. Clearly, a mere deviation from Standard Model predictions is not a proof for supersymmetry, but properties of new particles have to be investigated to conclude on the underlying mathematical description. Among these properties are the new particle masses, whose determination will be challenging, since the preferred SUSY models always include undetectable particles in the final state of collisions and a direct reconstruction of invariant masses is impossible. Nevertheless, different approaches to mass determination of supersymmetric particles were studied in recent years.

In this thesis a novel method for mass determination is presented, which exploits a prominent feature of R-parity conserving supersymmetry. Heavy new particles are produced in pairs and decay via several intermediate mass states into the lightest and stable supersymmetric state, yielding several jets and leptons in the final state. An approach based on the reconstruction of such decay cascades via a kinematic fit, the combination of many topologically identical events, and a scan of possible mass values is developed and demonstrated

for a particular SUSY scenario. Experimental conditions at the LHC are simulated in good approximation by using the detector simulation of the CMS experiment, which provides a realistic modeling of the detector performance. Masses of SUSY particles in a Monte Carlo Simulation are determined and statistical uncertainties as well as systematic effects are studied.

This thesis begins with a short review of the Standard Model and an introductory overview on the supersymmetric theory. SUSY phenomenology and the discovery potential at the LHC as well as recent exclusion limits from the CMS experiment are summarized in the following. In chapter 3 the LHC and the CMS experiment and its performance in particle reconstruction are described. The next chapter reviews the topic of mass determination in SUSY events and the principal ideas behind the new mass determination method are explained. Starting with Chapter 5, details on the setup in terms of physics scenario and technical realization are presented and Chapter 7 then treats the application of the kinematic-fits-method for mass determination. Finally, results are compared to other methods and conclusions are drawn.

Chapter 2

Theory and Phenomenology of Supersymmetry

This chapter provides the theoretical background for the physics phenomena investigated in this thesis. A very brief review of the main structures of the Standard Model of particle physics, and a sketch of its shortcomings are followed by an overview on Supersymmetry, with some focus on the investigated mSUGRA model and sparticle masses. Expectations and properties for SUSY at the LHC are covered in combination with existing exclusion limits. Argumentation for the theoretical part (Sec. 2.1 and 2.2) is mainly based on existing summaries and educational articles [1–5], which contain further references to the original work.

2.1 The Standard Model

The Standard Model of particle physics (SM) [6–14] describes all elementary particles which have been observed in experiments so far and their strong, weak and electromagnetic interactions. The SM was tested in many precision collider experiments and no significant deviation from its predictions were found [15,16]. Two ingredients enter the Standard Model, on the one hand the observed particles, and on the other hand the interactions amongst them, which are described by means of a renormalizable quantum field theory. Fermionic Particles, i.e. quarks and leptons, are classified by their behaviour in the gauge boson mediated interactions.

The mathematical description is based on a non-Abelian gauge group, given by the inner product $SU(3)_C \times SU(2)_L \times U(1)_Y$, and the Poincaré group of space-time transformations as an outer symmetry. The color gauge group $SU(3)_C$ from Quantum Chromodynamics (QCD) specifies the strong interactions, while electroweak interactions are based on the unified $SU(2)_L \times U(1)_Y$ group. The generators of each group are hermitian matrices which fulfill the following commutation relations, where T^a ($a = 1, \dots, 8$), I^i ($i = 1, \dots, 3$) and

Y are the generators of $SU(3)_C$, $SU(2)_L$ and $U(1)_Y$, respectively.

$$[T^a, T^b] = if^{abc}T^c, \quad [I^i, I^j] = i\epsilon^{ijk}I^k, \quad [Y, Y] = 0. \quad (2.1)$$

The structure constants of the gauge groups are given by the totally antisymmetric tensors f^{abc} and ϵ^{ijk} .

The particles' quantum numbers corresponding to these generators are color charge (T^a), weak isospin (I^i), and weak hypercharge (Y). The electric charge of a particle is given by the Gell-Mann-Nishijima relation $Q = I^3 + Y/2$.

Particles are described by relativistic quantum fields and can be divided into three groups, matter, gauge, and Higgs boson fields.

Matter is build of spin-1/2 fermions which are either color charged quarks ($SU(3)_C$ triplets) or leptons without strong interactions ($SU(3)_C$ singlets). Six flavors of quarks have been observed carrying an electric charge of either $Q = +2/3$ (u, c, t) or $Q = -1/3$ (d, s, b). The electron (e) and its heavier copies muon (μ) and tau-lepton (τ) are accompanied by three electrically neutral neutrinos (ν). Quarks and leptons group into three families of left- and right-handed chiral fermions.

$$\begin{aligned} & \begin{pmatrix} \nu_e \\ e \end{pmatrix}_L, \quad \begin{pmatrix} \nu_\mu \\ \mu \end{pmatrix}_L, \quad \begin{pmatrix} \nu_\tau \\ \tau \end{pmatrix}_L, \quad e_R, \quad \mu_R, \quad \tau_R \\ & \begin{pmatrix} u \\ d \end{pmatrix}_L, \quad \begin{pmatrix} c \\ s \end{pmatrix}_L, \quad \begin{pmatrix} t \\ b \end{pmatrix}_L, \quad u_R, \quad d_R, \quad c_R, \quad s_R, \quad t_R, \quad b_R \end{aligned} \quad (2.2)$$

Left-handed fermions transform under $SU(2)_L$ as doublets while right-handed particles are $SU(2)_L$ singlets, i.e. they do not carry weak isospin. If neutrinos are not massless, right handed neutrinos (ν_R) can in principle be included in this scheme.

The number of particles from a generation of quarks or leptons is (approximately) conserved in the SM, as well as the total baryon and lepton number. This empiric observation is not related to any of the fundamental symmetries the theory is based on.

Gauge boson fields, corresponding to the generators of the gauge groups, are spin-1 particles, which mediate the interactions among fermions. From the QCD $SU(3)_C$ group 8 gluons emerge and the electroweak symmetry yields three W bosons from $SU(2)_L$ and the $U(1)_Y$ B boson.

All these gauge bosons would be massless, if the symmetries of the SM were exact. However, while gluons are in fact massless, massive bosons were observed in electroweak processes.

Since the invariance of the Lagrangian under $SU(2) \times U(1)$ transformations breaks if explicit mass terms for bosons and fermions are introduced, another mechanism is necessary to add particle masses to the theory. The Higgs mechanism [11–14] is one possibility

to give masses to gauge bosons and fermions. With this mechanism, masses enter in a gauge invariant way and renormalizability is preserved. It exploits spontaneous symmetry breaking, i.e. additional fields are introduced which keep the invariance of the Lagrangian under gauge transformations but break the invariance of its ground state.

A complex scalar field $\Phi = (\phi^+, \phi^0)^T$ is added to the theory, which transforms as a $SU(2)_L$ doublet with hypercharge $Y = 1$ and has a scalar potential $V(\Phi) = \mu^2 \Phi^\dagger \Phi + \lambda (\Phi^\dagger \Phi)^2$. It shows that it obtains a non-vanishing vacuum expectation value (VEV) $\langle 0 | \Phi | 0 \rangle = \sqrt{-\mu^2 / (2\lambda)}$ for $\mu < 0$. By expanding Φ around its VEV and inserting in the Lagrangian one finds that three degrees of freedom are absorbed in the longitudinal polarizations of the weak gauge bosons, which become massive particles. The remaining field constitutes a new scalar particle, the higgs boson H , which is yet to be found in nature.

The field Φ is chosen such, that the $SU(2)_L \times U(1)_Y$ symmetry is spontaneously broken but a $U(1)_Q$ symmetry related to the charge $Q = I^3 + Y/2$ is preserved. The corresponding massless gauge boson is identified as the photon (A_μ).

Mass eigenstates of the gauge bosons after electroweak symmetry breaking (EWSB) are given by linear combinations of the gauge fields W_μ^i and B_μ and described by a rotation with the so called weak mixing angle θ_W .

$$\begin{pmatrix} Z_\mu \\ A_\mu \end{pmatrix} = \begin{pmatrix} \cos \theta_W & -\sin \theta_W \\ \sin \theta_W & \cos \theta_W \end{pmatrix} \begin{pmatrix} W_\mu^3 \\ B_\mu \end{pmatrix} \quad (2.3)$$

$$W_\mu^\pm = \frac{1}{\sqrt{2}} (W_\mu^1 \mp i W_\mu^2) \quad (2.4)$$

The mixing angle is determined from the coupling constants corresponding to the $SU(2)_L$ and $U(1)_Y$ gauge groups, g and g' , as $\cos \theta_W = g / \sqrt{g^2 + g'^2}$. The masses of the W and Z bosons are proportional to the higgs VEV v , $m_W = vg/2$ and $m_Z = (v/2)\sqrt{g^2 + g'^2}$ and the weak mixing angle can be expressed in terms of these masses as $\cos \theta_W = m_W / m_Z$.

In order to achieve fermion masses Yukawa interaction terms are added to the Lagrangian, which couple fermions to the higgs field. These terms are invariant under electroweak symmetry but produce masses due to their non-vanishing VEV.

Also fermion mass eigenstates are obtained by rotation of the weak eigenstates. In the quark sector this is described by the Cabibbo-Kobayashi-Maskawa (CKM) matrix [17,18] whose entries are determined experimentally. In case of massless neutrinos the lepton mass and electroweak eigenstates are identical. Nowadays, evidence for non-zero neutrino masses and neutrino mixing exists and the Pontecorvo-Maki-Nakagawa-Sakata (PMNS) matrix describes the neutrino mixing in analogy to the CKM matrix [19].

The Higgs boson is the only SM particle which has not yet been observed in experiments. Its mass ($m_H = 2\lambda v^2 = -2\mu^2$) is a free parameter of the theory. However, theoretical and experimental constraints on its mass exist. A positive and finite Higgs self-coupling is necessary to ensure a Higgs potential that is bounded from below. In combination with a

cut-off scale of e.g. 10^3 TeV up to which one assumes the SM to be valid the higgs mass should e.g. lie in the interval $50 \text{ GeV} \lesssim m_H \lesssim 800 \text{ GeV}$ [20].

The strongest experimental limits were set by the LEP experiments and exclude a Higgs mass $m_H > 114 \text{ GeV}$ at 95% confidence level [21]. More recently the Tevatron experiments further excluded the mass region between 158 and 175 GeV at 95% confidence level [22].

2.1.1 Open Questions of the Standard Model

The Standard Model was successfully verified in many experiments and with very high precision [16]. Despite its tremendous success there are conceptual problems which indicate that new physics beyond the SM exists. The SM can be seen as an effective theory valid up to some higher energy scale and might in the future be considered the low energy limit of an underlying theory.

First of all the SM does not incorporate gravity, which will become important when approaching the Planck scale $\Lambda_{\text{Planck}} \sim 10^{18} \text{ GeV}$. Another question is why the electroweak scale is so much smaller than the Planck scale with $m_W/\Lambda_{\text{Planck}} \sim 10^{-16}$. Related to this fact is the fine-tuning or naturalness problem [1]. One expects the higgs mass to be of the order of the electroweak scale. However, radiative corrections to the higgs mass from fermions and massive gauge bosons are important, since these loop contributions to the self-energy are huge. If regularized with anal momentum cut-off Λ_{UV} they read

$$\Delta m_H^2 = \Lambda_{UV}^2 \sum_{n=0}^{\infty} c_n \log^n \left(\frac{\Lambda_{UV}}{\mu_R} \right), \quad (2.5)$$

where μ_R is the renormalization scale and the coefficients c_n depend on the masses of the particles in the loop and their couplings to the higgs boson. Note the quadratic divergence with the cut-off scale, i.e. the scale up to which the SM is valid. If the cut-off scale is very large, corrections must be adjusted precisely at each order in perturbation theory to yield a higgs mass around the electroweak scale.

A desired feature of a more fundamental theory is the unification of all forces. That means the description with a single gauge group (e.g. $SU(5)$ and $SO(10)$ were proposed) and a single coupling. In the SM the electroweak and strong interaction are not truly unified and keep their own coupling with different strength.

The evolution of the coupling constants with the energy scale is described by renormalization group equations. For unification the constants need to meet at a high scale, which is not given with the particle content of the SM. New physics entering at an intermediate scale might however change the running of the couplings and lead to unification.

A third argument for physics beyond the SM comes from cosmological observations. Rotation curves of galaxies as well as the cosmic microwave background indicate that a large amount of dark matter exists [23,24], i.e. non-baryonic, only weakly interacting

matter. Yet unknown particles must be the constituents of this cold dark matter, since the only SM candidates, neutrinos, are ruled out as a single source because their small masses and relativistic velocities cannot explain large scale structure formation.

The large number of parameters in the SM is sometimes regarded as unsatisfactory, especially the existence of unpredicted parameters which are related to the origin of particle masses, the hierarchical structure of fermion masses and CP violation.

In the next section supersymmetry is introduced, which is a popular theory beyond the Standard Model, which addresses some of the above issues.

2.2 Supersymmetry

2.2.1 Basic Ideas

Supersymmetry [25,26] was proposed as an extension of the internal gauge- and outer space-time symmetry of the SM. In the SM the generators of the SM gauge group commute with those of the Poincaré space-time symmetry and each particle is defined by its quantum numbers corresponding to the internal symmetries (color, weak isospin, hypercharge) as well as mass, spin and momentum. There is no way to combine these two symmetries other than as a direct product for a theory like the SM with chiral fermions.

In order to extend the Poincaré symmetry in a non-trivial way a new ansatz must be chosen: anti-commutation instead of commutation relations are postulated for the generators (Q) of the new symmetry. These must then be fermionic operators.

In a schematic form these anti-commutation relations of the SUSY Poincaré algebra read [1]

$$\{Q, Q^\dagger\} = P^\mu \quad (2.6)$$

$$\{Q, Q\} = \{Q^\dagger, Q^\dagger\} = 0 \quad (2.7)$$

$$[P^\mu, Q] = [P^\mu, Q^\dagger] = 0 \quad (2.8)$$

where the first line relates the SUSY generator Q with the generator of space-time translations P_μ .

In particle physics, SUSY relates bosonic and fermionic fields. The generator Q^1 as a fermionic operator changes the spin of a particle

$$Q|\text{boson}\rangle = |\text{fermion}\rangle \quad Q|\text{fermion}\rangle = |\text{boson}\rangle. \quad (2.9)$$

Bosonic and fermionic fields form a (irreducible) supermultiplet. The SUSY transformation only changes the spin, while all other quantum numbers are not altered. Since the known

¹In principle there can be more than one SUSY (with generator Q^N). However, the construction of $N > 1$ theories in particle physics leads to significant problems.

elementary particles do not fit into this scheme, the assumption of a supersymmetry implies the existence of new, yet undiscovered particles.

If SUSY was exact, these new particles would be mass degenerate with the known SM particles as one can see from the on-shell relation of a fermion f and a boson b

$$P^2|b\rangle = P^2Q|f\rangle = QP^2|f\rangle = Qm^2|f\rangle = m^2|b\rangle. \quad (2.10)$$

However, no supersymmetric particles were observed yet, so SUSY must be broken at low energies.

The operator Q relates one bosonic to one fermionic state, leading basically to a duplication of the particle content. Because left- and right handed fermions have different transformation behavior under $SU(2)_L$ a bosonic partner for each helicity state has to exist. Furthermore a second Higgs doublet needs to be introduced in the theory, as will be discussed later.

No theoretical constraints exist regarding the scale at which SUSY is broken, but low SUSY masses are phenomenologically preferred to keep some desirable properties of the model. As discussed before, the large radiative corrections to the Higgs mass in the Standard Model depend quadratically on the cut-off scale and need to be fine-tuned in order to obtain a Higgs mass around the electroweak scale. In SUSY the loop contributions of fermionic and bosonic partners cancel, due to their opposite sign. Cancellation is exact only in the case of unbroken SUSY, while logarithmic terms, proportional to the mass difference $m_F^2 - m_B^2$ remain in the broken case. Hence, the masses of the superpartners should not be too large ($\sim O(1 \text{ TeV})$) in order to retain the solution for the fine-tuning problem.

Another consequence of new SUSY particles, entering around the TeV-scale, is that they affect the running of the coupling constants and make a unification at a high scale (e.g. GUT scale) possible. Even an incorporation of gravity in the theory is feasible.

An attractive feature of SUSY models with R -parity conservation (c.f. Sec 2.2.3) is the existence of a stable, electrically neutral and weakly interacting particle, which is a good dark matter candidate.

2.2.2 Supersymmetry Breaking

In analogy to electroweak symmetry breaking, SUSY can also be broken spontaneously in order to provide the mass terms for the new SUSY partners. In this case the Lagrangian remains invariant under SUSY transformation, but the ground state acquires a non-vanishing vacuum expectation value.

Usually an indirect or radiative SUSY breaking is considered, in order to avoid theoretical problems. Explicit symmetry breaking terms are added at the breaking scale, which still respect the gauge and Poincaré invariance and are *soft* in order not to spoil the positive properties concerning e.g. the hierarchy problem. Possible terms in the Lagrangian are

mass terms for the gauginos (partners of gauge bosons) and scalars (fermion partners), as well as trilinear couplings of scalar fields. Chiral (SM) fermions still obtain masses by electroweak symmetry breaking in order to keep the gauge invariance. The spontaneous SUSY breaking takes place at a high scale in a hidden sector and is communicated to the visible particle sector via an interaction. The phenomenology in the visible sector depends mostly on the way of transmission and less on the breaking mechanism itself.

In super gravity models (SUGRA) the transmission takes place via gravity. Such models are widely studied and we will introduce a minimal SUGRA model in Sec. 2.2.3, which makes further assumptions on the universality of the couplings and the soft breaking terms at the GUT scale, thus reducing the large number of new parameters in more general SUSY models to just five. The transmitting gravitational strength interaction does not play a role in collider experiments. Other possibilities to realize SUSY breaking are gauge or anomaly mediation (GMSB/AMSB models).

2.2.3 The Minimal Supersymmetric Extension of the Standard Model (MSSM)

The minimal supersymmetric extension of the standard model (MSSM) contains the minimal set of particles, necessary to build a $N = 1$ SUSY model, which is softly broken at low energies and has conserved R -parity (see below).

Each bosonic state is grouped with a fermionic state in an irreducible representation, a supermultiplet. These partners have the same number of degrees of freedom (dof) and identical quantum numbers, except for the spin, which differs by one half. SUSY partners of the SM fermions are called sfermions and the left- and right-handed components of the SM fermions obtain a superpartner each. Gauge bosons have fermionic counterparts which are labeled gauginos (gluino, wino, bino). In the Higgs sector a second Higgs doublet is needed to provide masses for up- and down-type quarks, while keeping the gauge invariance and stay free of anomalies. The field content of the MSSM is summarized in Tab. 2.1.

R-Parity

The interactions among scalars and fermions in the MSSM are described by the superpotential, which is compatible with super- and gauge symmetry. In its most general form the superpotential contains lepton and baryon number violating terms, which lead to a fast and unrealistic proton decay. One possibility to cure this problem is the requirement of R -parity conservation, where R -parity is defined for each particle as

$$P_R = (-1)^{3(B-L)+2s}, \quad (2.11)$$

Here L is the lepton number, B the baryon number and s the spin of the particle. All SM particles, including the Higgs boson have positive R -parity $P_R = +1$, while all SUSY

Superfield	Boson	Fermion	$(SU(3)_C, SU(2)_L, U(1)_Y)$	Name
Q	$\tilde{q}_L = (\tilde{u}_L, \tilde{d}_L)^T$	$q_L = (u_L, d_L)^T$	$(3, 2, +\frac{1}{3})$	(s)quark
\bar{U}	\tilde{u}_R^*	u_R^\dagger	$(\bar{3}, 1, -\frac{4}{3})$	
\bar{D}	\tilde{d}_R^*	d_R^\dagger	$(\bar{3}, 1, +\frac{2}{3})$	
L	$\tilde{\ell}_L = (\tilde{\nu}, \tilde{e}_L)^T$	$\ell_L = (\nu, e_L)^T$	$(1, 2, -1)$	(s)lepton
\bar{E}	\tilde{e}_R^*	e_R^\dagger	$(\bar{1}, 1, +2)$	
H_u	$h_u = (h_u^+, h_u^0)^T$	$\tilde{h}_u = (\tilde{h}_u^+, \tilde{h}_u^0)^T$	$(1, 2, +1)$	Higgs(-ino)
H_d	$h_d = (h_d^0, h_d^-)^T$	$\tilde{h}_d = (\tilde{h}_d^0, \tilde{h}_d^-)^T$	$(1, 2, -1)$	
G^a	g	\tilde{g}	$(8, 1, 0)$	gluon(-ino)
W^i	W^\pm, W^0	$\tilde{W}^\pm, \tilde{W}^0$	$(1, 3, 0)$	W(-ino)
B	B	\tilde{B}	$(1, 1, 0)$	B(-ino)

Table 2.1.: Overview of particle fields in the MSSM. The superfields (capital letters) have a bosonic and a fermionic component, which share the same behavior under gauge transformations, indicated in column four. SUSY partners carry a tilde. The L, R indices of the scalar SUSY particle indicate the helicity of the SM partner. Generation and color indices are omitted for readability. The first generation initials are used. Names of the (new) particles are given in the last column.

particles have $P_R = -1$. For conservation all vertices must yield a positive product of the involved particle parities.

The assumption of R-parity conservation has several consequences. All SUSY particles can only be produced associated or in pairs, their decay must yield an odd number of SUSY particles, and the lightest supersymmetric particle (LSP) is stable since it cannot decay into a lighter one.

In general any SUSY particle can be the LSP but usually regions with a charged LSP (e.g. a stau) are excluded in phenomenological studies. In a large part of the (mSUGRA) parameter space the lightest neutralino is the LSP.

At hadron colliders strongly interacting SUSY particles, squarks and gluons, will be produced in pairs and initiate a chain of decaying SUSY particles, ending with the lightest and stable one. These possibly long decay chains will leave a signature of missing transverse energy and many jets and leptons in the detector. The properties of such supersymmetric events at hadron colliders are discussed further in Sec. 2.3.1.

The MSSM Lagrangian

The Lagrangian of a supersymmetric theory is obtained from the requirement that the action $\int d^4x \mathcal{L}(x)$ is invariant under a SUSY transformation. In a broken supersymmetry

it consists of SUSY invariant and (soft) SUSY breaking parts

$$\mathcal{L}_{MSSM} = \mathcal{L}_{SUSY} + \mathcal{L}_{soft} \quad (2.12)$$

The Lagrangian will not be discussed in detail here, but we will outline some aspects concerning particle masses in the following sections.

The SUSY invariant part can be divided into the superpotential, which specifies the interaction of scalars and fermions, a kinetic term for gauginos and gauge bosons, and a kinetic term for scalars and fermions. The gauge invariant soft breaking part of the Lagrangian in case of R -parity conservation is

$$\begin{aligned} \mathcal{L}_{soft} = & - \frac{1}{2}(M_1 \tilde{B} \tilde{B} + M_2 \tilde{W} \tilde{W} + M_3 \tilde{g} \tilde{g}) + h.c. \\ & - \tilde{q}_L^\dagger \mathbf{m}_Q^2 \tilde{q}_L - \tilde{u}_R^* \mathbf{m}_U^2 \tilde{u}_R - \tilde{d}_R^* \mathbf{m}_D^2 \tilde{d}_R - \tilde{\ell}_L^\dagger \mathbf{m}_L^2 \tilde{\ell}_L - \tilde{e}_R^* \mathbf{m}_E^2 \tilde{e}_R \\ & - m_{h_u}^2 h^\dagger h_u - m_{h_d}^2 h_d^\dagger h_d - (b h_u h_d + h.c.) \\ & - \left(\mathbf{a}_U \tilde{q}_L h_u \tilde{u}_R^* - \mathbf{a}_D \tilde{q}_L h_d \tilde{d}_R^* - \mathbf{a}_E \tilde{\ell}_L h_d \tilde{e}_R^* \right) + h.c. \end{aligned} \quad (2.13)$$

where fields are labeled according to Tab. 2.1 and $SU(2)_L$ as well as generation indices are suppressed. Several mass related parameters are introduced here. The first line consists of gaugino mass terms, depending on the complex mass parameters M_1 , M_2 and M_3 . In the second line squark and slepton mass terms occur, where \mathbf{m}^2 are hermitian mass matrices in family space. Line three includes Higgs boson mass terms with the real (squared) mass parameters $m_{h_{d/u}}^2$ and the complex Higgs coupling b . In the last line trilinear sfermion-sfermion-higgs interactions can be found. The couplings can also be expressed in terms of trilinear couplings \mathbf{A} and Yukawa couplings \mathbf{Y}

$$\mathbf{a}_{U,D,E} \equiv \mathbf{A}u, d, e \mathbf{Y}_{U,D,E}. \quad (2.14)$$

Constraints in Minimal Supergravity

The superpotential and the soft breaking terms (Eq. 2.13) introduce a total of 105 new parameters in the theory. Many of these couplings, masses and complex phases are constrained by experimental data on flavor changing neutral currents or CP violation. While flavor mixing is in general appearing in the soft breaking Lagrangian, it is common to assume minimal flavor violation, which means that the CKM matrix is the only source of CP violation. This implies that the SUSY mass matrices and trilinear couplings in the soft breaking terms are diagonal and no flavor changing neutral currents (FCNC) exist on tree

level.

$$\mathbf{m}_{\tilde{F}}^2 = \text{diag}(m_{\tilde{F}_1}^2, m_{\tilde{F}_2}^2, m_{\tilde{F}_3}^2), \quad \text{for} \quad \tilde{F} = \{\tilde{Q}, \tilde{\nu}, \tilde{D}, \tilde{L}, \tilde{E}\} \quad (2.15)$$

$$\mathbf{A}_f = \text{diag}(A_{f_1}, A_{f_2}, A_{f_3}), \quad \text{for} \quad f = \{u, d, e\} \quad (2.16)$$

As already mentioned the SUSY breaking in SUGRA scenarios is transmitted to the visible sector via gravitational interactions. In minimal supergravity models (mSUGRA) more constraints are used. Beside a unification of the gauge-couplings at the GUT scale, a simultaneous unification of the scalar and gaugino masses is assumed in minimal SUGRA (mSUGRA). This leads to common values for the gaugino masses ($M_{1/2}$), all scalar masses (M_0) and the trilinear couplings (A_0).

$$\mathbf{m}_{\tilde{Q}}^2 = \mathbf{m}_{\tilde{L}}^2 = \mathbf{m}_{\tilde{U}}^2 = \mathbf{m}_{\tilde{D}}^2 = \mathbf{m}_{\tilde{E}}^2 = M_0^2 \mathbf{1}_3 \quad (2.17)$$

$$m_{h_u}^2 = m_{h_d}^2 = M_0^2 \quad (2.18)$$

$$M_1 = M_2 = M_3 = M_{1/2} \quad (2.19)$$

$$\mathbf{a}_U = A_0 \mathbf{Y}_U, \quad \mathbf{a}_D = A_0 \mathbf{Y}_D, \quad \mathbf{E}_U = A_0 \mathbf{Y}_E \quad (2.20)$$

Starting from these boundary conditions for parameters at the GUT scale, all masses and couplings at lower energies are obtained by means of renormalization group equations. Two more independent parameters remain in mSUGRA. The Higgsino mass parameter (μ) and the bilinear coupling (b) which can be substituted by the ratio of the Higgs vacuum expectation values, $\tan \beta$ (see below), and the sign of μ at the weak scale. Together with $M_{1/2}$, M_0 and A_0 this sums to only five free parameters determining the entire phenomenology in mSUGRA models.

Particle Masses

The inclusion of particle masses in the MSSM also happens via the Higgs mechanism and the electroweak symmetry is broken spontaneously. A second higgs doublet has to be introduced to provide mass terms for up- and down-type quarks which are compatible with the gauge symmetries. Their neutral components have non-vanishing vacuum expectation values, v_d and v_u . Two complex doublet fields mean eight degrees of freedom, three of which are Goldstone bosons and are absorbed in the W and Z bosons. Five degrees of freedom remain, resulting in five physical spin-0 higgs bosons.

Two of them are neutral and CP-even (h^0, H^0), one is neutral but CP-odd (A^0) and the

remaining two are the charged bosons H^\pm . Their squared masses are given by

$$m_{A^0}^2 = m_{h_d}^2 + m_{h_u}^2 + 2|\mu|^2 = b(\tan \beta + \cot \beta) \quad (2.21)$$

$$m_{h^0/H^0}^2 = \frac{1}{2}(m_{A^0}^2 + m_Z^2) \mp \sqrt{(m_{A^0}^2 + m_Z^2)^2 - 4m_{A^0}^2 m_Z^2 \cos^2 2\beta} \quad (2.22)$$

$$m_{H^\pm}^2 = m_{A^0}^2 + m_Z^2 \quad (2.23)$$

with $\tan \beta = v_u/v_d$. The expressions for the electroweak gauge boson masses change slightly and contain the new VEVs

$$m_W^2 = \frac{g^2}{2}(v_d^2 + v_u^2), \quad m_Z^2 = \frac{g^2 + g'^2}{2}(v_d^2 + v_u^2). \quad (2.24)$$

As before, all SM fermions acquire their mass by Yukawa interactions with the Higgs fields.

For the fermion superpartners in mSUGRA it is assumed that mixing occurs only within one generation. The mass terms of the Lagrangian can be written

$$\mathcal{L}_{\text{Sfermionmass}} = -(\tilde{f}_{Li}^*, \tilde{f}_{Ri}^*) \mathcal{M}_{\tilde{f}_i}^2 \begin{pmatrix} \tilde{f}_{Li} \\ \tilde{f}_{Ri} \end{pmatrix} - \tilde{\nu}_i^* m_{\tilde{\nu}_i}^2 \tilde{n} u_i \quad (2.25)$$

where the mass matrix

$$\mathcal{M}_{\tilde{f}_i}^2 = \begin{pmatrix} m_{\tilde{f}_i}^2 + A_i^{LL} & m_{\tilde{f}_i} B_i^{LR} \\ m_{\tilde{f}_i} B_i^{LR} & m_{\tilde{f}_i}^2 + C_i^{RR} \end{pmatrix} \quad (2.26)$$

depends on the SM fermion masses m_{f_i} and the terms

$$A_i^{LL} = m_{\tilde{F}_{Li}}^2 - (I_{f_i}^3 - e_{f_i} \sin^2 \theta_W) m_Z^2 \cos 2\beta \quad (2.27)$$

$$B_i^{LR} = A_{f_i} - \mu \kappa \quad (2.28)$$

$$C_i^{RR} = m_{\tilde{F}_{Ri}}^2 + e_{f_i} \sin^2 \theta_W m_Z^2 \cos 2\beta. \quad (2.29)$$

In this notation $m_{\tilde{F}_{L/Ri}}^2$ are the soft-breaking parameters for the scalar partners of left- and right-handed chiral fermions. $I_{f_i}^3$ is the third component of the isospin of the corresponding SM fermion and e_{f_i} its electric charge. In the mSUGRA assumptions Eq. 2.15 the trilinear couplings A_{f_i} were introduced. For up-type squarks and charged leptons applies $\kappa = \cot \beta$ while $\kappa = \tan \beta$ for down-type squarks. For the sneutrino the matrix is one-dimensional

$$m_{\tilde{\nu}_i}^2 = m_{\tilde{F}_{Li}}^2 + \frac{1}{2} m_Z^2 \cos 2\beta \quad (2.30)$$

One can see that sfermion masses depend on parameters from the Higgs sector (β , m_Z , μ , θ_W) as well as on soft breaking parameters ($m_{\tilde{F}_{L/Ri}}^2$, A_{f_i}).

In order to obtain the mass eigenstates the mass matrix must be diagonalized with a unitary matrix $U_{\tilde{f}_i}$, which can be expressed in terms of a mixing angle $\theta_{\tilde{f}_i}$

$$U_{\tilde{f}_i} = \begin{pmatrix} \cos \theta_{\tilde{f}_i} & \sin \theta_{\tilde{f}_i} \\ -\sin \theta_{\tilde{f}_i} & \cos \theta_{\tilde{f}_i} \end{pmatrix}. \quad (2.31)$$

One finds the squared eigenvalues

$$m_{\tilde{f}_{1i,2i}}^2 = m_{f_i}^2 + \frac{1}{2} \left[(A_i^{LL} + C_i^{RR}) \mp \sqrt{(A_i^{LL} + C_i^{RR})^2 + 4m_{f_i}^2 (B_i^{LR})^2} \right] \quad (2.32)$$

for the eigenstates $\tilde{f}_{1i,2i}$, where the convention is that the index increments with increasing mass. From diagonalization it comes out that

$$\tan \theta_{\tilde{f}_i} = \frac{2m_{f_i} B_i^{LR}}{A_i^{LR} - C_i^{LR}}. \quad (2.33)$$

Hence the mixing of sfermions is proportional to the corresponding SM fermion mass, leading to a negligibly small amount of mixing in the first two generations. Therefore it is justified to keep the indices L and R when talking about 1st and 2nd generation sfermion masses in the following. Furthermore, the masses of up- and down-type squarks within one family are related and their difference is constrained. For the third generation squarks a significant mixing takes place and the mass eigenstates are usually labelled as \tilde{b}_1, \tilde{t}_1 for the lighter and \tilde{b}_2, \tilde{t}_2 for the heavier combination.

Also higgsinos and gauginos can mix after electroweak symmetry breaking. The electrically charged higgsinos and winos ($\tilde{h}_u^+, \tilde{h}_d^-, \tilde{W}^\pm$) constitute charginos ($\tilde{\chi}_{1,2}^\pm$), while the neutral higgsinos, wino and bino ($\tilde{h}_u^0, \tilde{h}_d^0, \tilde{W}^0, \tilde{B}$) form four neutralinos ($\tilde{\chi}_{1-4}^0$). In both cases the indices increase with particle mass.

Assuming real parameters only, one obtains the following expression for the chargino masses

$$m_{\tilde{\chi}_{1,2}^\pm}^2 = \frac{1}{2} (M_2^2 + \mu^2 + 2m_W^2) \mp \frac{1}{2} \sqrt{(M_2^2 + \mu^2 + 2m_W^2)^2 - 4(\mu M_2 - m_W^2 \sin 2\beta)^2} \quad (2.34)$$

The mass eigenvalues for the neutralinos cannot easily be written down in an analytic form. Neutralino masses depend on M_1, M_2, μ , and $\tan \beta$ and the mass matrix before

diagonalization reads

$$\mathcal{M}_{\tilde{\chi}^0} = \begin{pmatrix} M_1 & 0 & -m_Z \sin \theta_W \cos \beta & m_Z \sin \theta_W \sin \beta \\ 0 & M_2 & m_Z \cos \theta_W \cos \beta & -m_Z \cos \theta_W \sin \beta \\ -m_Z \sin \theta_W \cos \beta & m_Z \cos \theta_W \cos \beta & 0 & -\mu \\ m_Z \sin \theta_W \sin \beta & -m_Z \cos \theta_W \sin \beta & -\mu & 0 \end{pmatrix} \quad (2.35)$$

The eigenvalues have to be determined from quartic equations, which in general has to be done numerically. However, simplified expressions can be derived for particular scenarios.

The mSUGRA assumptions of a gaugino mass unification at the GUT scale is motivated by the running behavior of the gauge couplings. Gaugino masses run in the same way as (squared) gauge couplings

$$\frac{M_1}{g^2} \approx \frac{M_2}{g'^2} \approx \frac{M_3}{g_s^2} \quad (2.36)$$

and one finds, that at the weak scale the mass parameters M_1 and M_2 have approximately the relation

$$M_1(m_Z) = \frac{5}{3} \tan^2 \theta_W M_2(m_Z) \approx \frac{1}{2} M_2(m_Z). \quad (2.37)$$

If effects of EWSB can be considered as small perturbations on the mass matrix, i.e. if $m_Z \ll |\mu \pm M_1|, |\mu \pm M_2|$, then the lightest neutralino has a dominant bino content, the second lightest is "wino-like" and the heavy neutralinos are mainly higgsinos. Then their masses are approximately

$$m_{\tilde{\chi}_1^0} = M_1, \quad m_{\tilde{\chi}_2^0} = M_2, \quad m_{\tilde{\chi}_{3,4}^0} = |\mu| \quad (2.38)$$

In large regions of the mSUGRA parameter space the lightest neutralino is the LSP.

The last particle in this discussion is the gluino. Its mass is determined by the (complex) soft-breaking parameter M_3

$$m_{\tilde{g}} = |M_3|. \quad (2.39)$$

2.3 SUSY at the LHC

2.3.1 Event Properties in R-parity Conserving Supersymmetry

Assuming conservation of R-parity all supersymmetric particles must be produced in pairs. The production at the Large Hadron Collider (LHC, c.f. Sec. 3.1) proceeds dominantly via gluon-gluon and gluon-quark fusion, due to the high parton-luminosity of the gluon. Feynman diagrams for some possible processes on tree-level are shown in Fig. 2.1. They yield squarks and gluinos as final-state and starting point for the supersymmetric decay

chain.

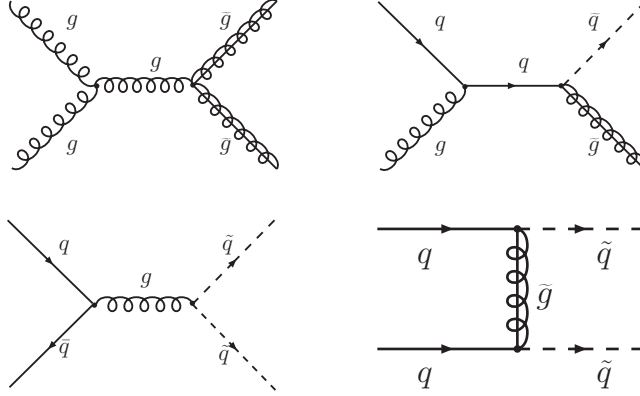


Figure 2.1.: Example Feynman diagrams of tree level processes for gluino (\tilde{g}) and squark (\tilde{q}) production by strong interactions.

Reactions with QCD strength can be summarized as

$$\begin{aligned}
 gg &\rightarrow \tilde{g}\tilde{g}, \tilde{q}_i\tilde{q}_j^* \\
 qg &\rightarrow \tilde{g}\tilde{q}_i \\
 q\bar{q} &\rightarrow \tilde{g}\tilde{g}, \tilde{q}_i\tilde{q}_j^* \\
 qq &\rightarrow \tilde{q}_i\tilde{q}_j.
 \end{aligned}$$

If squark and gluino masses are larger than about 1 TeV, direct chargino and neutralino production via quark annihilation into W - or Z -bosons can become the dominant processes [1].

As a second consequence of R-parity conservation, the decay of any SUSY particles yields an even number of superparticles. Due to their short lifetime, a cascade of instantly decaying particles develops, ending with the lightest and stable one (LSP).

Thus the generic signature of SUSY events is missing transverse energy resulting from the two LSPs escaping the detector. In addition a large number of jets and/or leptons in the final state might be found in mSUGRA or isolated photons in GMSB models.

However, in mSUGRA scenarios with a "bino-like" $\tilde{\chi}_1^0$, the largest fraction of right-handed squarks decays directly into the LSP and a quark, leading to a dijet signature for events with two such squarks.

Due to rather light third generation squarks their production is enhanced and an increased number of b -jets might be observed, originating from stop- and sbottom-decays.

Mixing may lead to a stau which is lighter than smuons and selectrons. Then the branching fraction for final states with tau leptons in chargino and neutralinos decays can become large, making tau identification a crucial component in the detection of SUSY events.

An important feature of SUSY are the large mass differences among the involved superparticles, in most cases allowing for their on-shell production in the decay chain. Therefore a determination of sparticle masses through a complete kinematic reconstruction of the event becomes possible. However, such an event reconstruction is challenging since two invisible LSPs escape the detector.

2.3.2 Searches for Supersymmetry

Current Mass Limits

Many searches for supersymmetric particles have been performed at particle colliders until today. While no evidence for new particles was found, limits on their masses were set. The most stringent limits come from the experiments at the LEP and Tevatron colliders [27–29].

In e^+e^- -collisions at LEP all particles had to be produced via electroweak interactions. While in principle all SUSY particles but gluinos can be produced this way, the available phase space decreases with increasing mass, such that the production cross-sections are highest for the light superparticles. In many SUSY scenarios these are sleptons and gauginos, rather than squarks. The most sensitive searches were performed in channels with leptons in addition to missing energy.

At the Tevatron ($p\bar{p}$) collider both, the production via electro-weak and via strong interactions, can have large cross-sections. If gluino and squarks are rather heavy ($\gtrsim 300$ GeV) the process of quark annihilation into a W - or Z -boson dominates the production and yields mainly charginos and neutralinos. If their masses are smaller, squarks and gluinos are produced in QCD processes. Consequently, searches were performed in channels with jets and missing transverse energy as well as in channels with up to three leptons.

A missing deviation from the standard model prediction in any of the search channels can only be translated into mass limits if assumptions on the SUSY breaking scenario and its parameters are made. However, summarizing current exclusion limits in a simplifying manner, one can say that all superpartners, except the gluino and LSP are constrained to masses larger than ~ 100 GeV. An indirect lower limit on the neutralino LSP mass of 47 GeV holds at 95% confidence level for the MSSM with gaugino and sfermion mass unification. For mSUGRA models with low $\tan\beta$ the Tevatron searches even restrict gluinos and squarks at 95% confidence level to masses above 308 GeV and 379 GeV, respectively [30].

Limits from the CDF experiment in the m_0 - $m_{1/2}$ -plane for an mSUGRA scenario with $A_0 = 0$, $\tan\beta = 5$ and $\mu < 0$ are shown Fig. 2.2

In addition to searches for supersymmetric particles a detection of neutral or charged higgs bosons could give a hint at SUSY. The higgs' masses depend on the SUSY parameters and their absence therefore allows an exclusion of parameter regions. So far no evidence for a higgs particle was found.

In recent month first SUSY limits based on LHC collision data at $\sqrt{s} = 7$ TeV were

published by the CMS collaboration and further restrict the parameter space (Fig. 2.2, bottom).

Prospects for a Discovery at the LHC

The LHC design center-of-mass energy of 14 TeV is more than seven times higher than the Tevatron energy. It allows for a production of squarks and gluinos in QCD-strength interactions for masses up to 1.5 TeV. As a result the total cross-section for a typical mSUGRA scenario can reach tens of picobarn, which is an increase by three orders of magnitude with respect to the Tevatron. In combination with the up to 30 times higher luminosity, the LHC will very likely lead to a discovery if TeV scale supersymmetry exists. SUSY particles must be in the accessible mass range to provide the solution to the hierarchy problem.

Both multi-purpose experiments at the LHC, Atlas and CMS (c.f. Sec. 3.2), have evaluated their discovery potential for various channels in Monte Carlo studies [31,32].

Fig. 2.2 illustrates the discovery reach for the CMS detector in the m_0 - $m_{1/2}$ -plane of the mSUGRA model for $\tan\beta = 10$, $A_0 = 0$ and $\mu > 0$. The inclusive hadronic channel with many jets and missing transverse energy covers the largest part of the parameter plane, while the power of channels including multiple leptons is more parameter dependent. However, the control of the standard model backgrounds is especially challenging for the hadronic searches and thus leptonic signatures might be easier to detect and yield a higher significance. A discovery of supersymmetry is possible already with low integrated luminosity of a few hundred pb^{-1} if its parameters are close to the current limits.

Chapter 3

The CMS Experiment at the LHC

3.1 The Large Hadron Collider

The Large Hadron Collider (LHC) [35] is a proton-proton and heavy-ion collider, located at CERN, the European Laboratory for Particle Physics, at the French-Swiss border near Geneva. It is designed for proton collisions at a center-of-mass energy of 14 TeV with a luminosity of $10^{34} \text{ cm}^{-2}\text{s}^{-1}$ and heavy ion collisions with 2.8 TeV per nucleon and a luminosity of $10^{27} \text{ cm}^{-2}\text{s}^{-1}$. After a decade of construction it started operations in September 2009, when the two rotating beams were first brought to collisions at the four interaction points around the ring.

Large particle detectors are build around these interaction points to record the reactions taking place. The Atlas (A Toroidal LHC ApparatuS) and CMS (Compact Muon Solenoid) experiments are multi-purpose detectors, especially designed for the search for the higgs boson and new phenomena. The LHCb detector is dedicated to B-physics, while Alice (A Large Ion Collider Experiment) aims at the investigation of heavy-ion collisions.

Although designed for a center-of-mass energy of 14 TeV, the 2010 LHC run was performed with only half of its maximum energy for machine protection reasons. After the collection of data corresponding to a few fb^{-1} of integrated luminosity, presumably by the end of 2012, the accelerator safety installations will be upgraded in a year-long stop to allow for design energy operations. Nevertheless the current center-of-mass energy already exceeds any previous collider and is more than 3.5 times higher than the Tevatron energy.

3.1.1 The LHC Design

The LHC is installed in the tunnel of the former LEP collider, 45 to 170 m below surface. It consists of eight arcs with dipole bending magnets and eight straight sections, where beam injection, acceleration, dumping or cleaning and beam collisions within the experiments take place (Fig. 3.1).

Each beam circulates in a separate ring, since beam particles have the same charge and cannot share the same dipole fields. The vacuum containers are only linked in the region

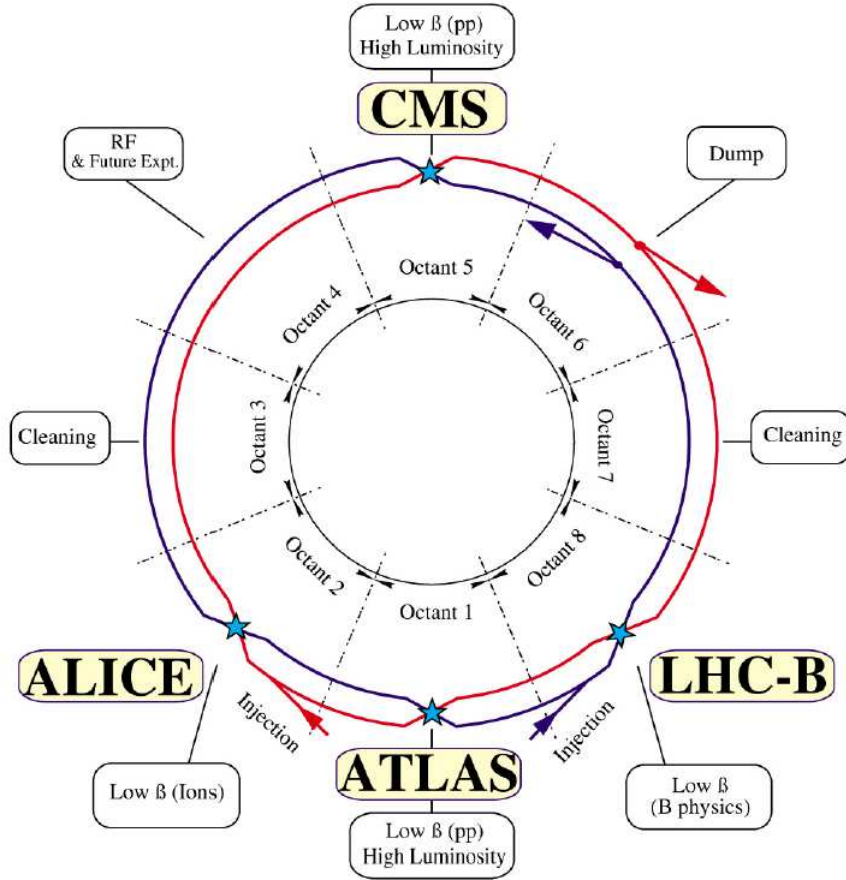


Figure 3.1.: Schematic view of the LHC layout [35].

around the interaction points. Superconducting dipole magnets with a field strength of 8.33 T are necessary to force the 7 TeV beams around the tunnel.

The accelerator chain starts with a linear accelerator (Linac), followed by the Proton Synchrotron Booster (PSB) and the Proton Synchrotron (PS), where proton bunches with an energy of 25 GeV are formed. They are passed to the Super Proton Synchrotron (SPS) and accelerated to the LHC injection energy of 450 GeV. After entering the LHC ring the beam energy is increased by about 0.5 MeV per turn until reaching the collision energy [36].

In maximum luminosity operations the proton beams will have $n_b = 2808$ bunches each, with $N_b = 1.15 \times 10^{11}$ protons per bunch and a spacing of 25 ns. At the interaction points they are squeezed to yield a beam spot with a transverse width of $\sigma^* = 16.7 \mu\text{m}$ [36].

The resulting instantaneous luminosity depends further on the revolution frequency f_{rev} , the relativistic gamma factor γ_r , the normalized transverse beam emittance ϵ_n and the beta function β^* at the collision point. Assuming a gaussian beam distribution, it is given

by

$$L = \frac{N_b^2 n_b f_{rev} \gamma_r}{4\pi \epsilon_n \beta^*} F, \quad (3.1)$$

where F is a geometric luminosity reduction factor, depending on the crossing angle, the bunch length and the transverse beam size. The LHC peak luminosity is $L = 10^{34} \text{ cm}^{-2} \text{ s}^{-1}$.

The event rate f is related to the luminosity and the cross-section σ

$$f = L \cdot \sigma. \quad (3.2)$$

About 20 collisions per bunch crossing and an event rate of around one billion events per second are expected, corresponding to a total cross-section of $\sigma_{tot} = 100 \text{ mb}$.

The luminosity decays during a fill as intensity degrades and emittance grows due to collisions, but also due to beam-gas and beam-beam interactions. For a high luminosity run, with collisions in the ATLAS and CMS experiments, the lifetime is approximately $\tau_L = 15 \text{ h}$. With a run of duration T_{run} an integrated luminosity of

$$L_{int} = L_0 \tau_L \left(1 - e^{-T_{run}/\tau_L} \right) \quad (3.3)$$

can be collected.

With an estimated turnaround time of 7 h for an entire accelerator cycle, including the filling of the machine, acceleration, collisions, and ramping down the magnets again, the integrated luminosity is maximized for a run time of 12 h. Assuming 200 days of operations the achievable integrated luminosity per year can reach up to 120 fb^{-1} .

3.2 The CMS Detector

The Compact Muon Solenoid (CMS) experiment [37] is one of the four large particle detectors at the LHC. It is placed in an underground cavern at Point 5 of the accelerator ring.

The CMS experiment consists of subdetectors for tracking and calorimetry placed inside a 3.8 T solenoid, and a muon system, embedded in the magnet return yoke (Fig. 3.2). Forward detectors complete its hermetic coverage of the interaction point. For the tracking device silicon pixel and strip components were chosen. Electromagnetic energy is measured in lead-tungstate crystals while the hadronic calorimeter uses brass absorber plates and layers of scintillating fibers. Three kinds of gaseous detectors are used in the muon system. CMS is 21.5 m high, has a diameter of 15 m and a total weight of 12500 tons. Its individual components are described in the following sections.

The challenging experimental environment at the LHC, with high collision rates and around 20 inelastic collisions per bunch crossing leads to high activity in the detector. Approximately 1000 charged particles enter the tracker every 25 ns. This requires a high

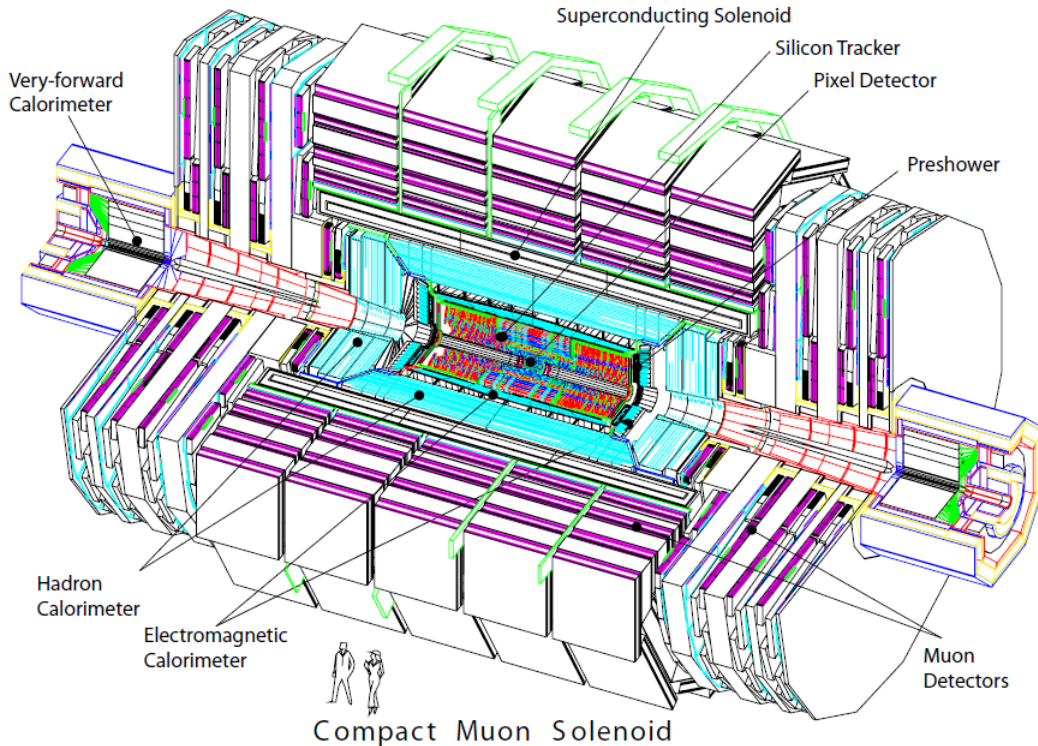


Figure 3.2.: Schematic view of the CMS detector [37]

detector granularity to reduce the average occupancy and reduce the impact of pile-up, a good time resolution to distinguish collisions, and a fast readout to minimize dead time. Triggers must select interesting events out of these 10^9 mainly low- p_T scatterings per second with a rate of ~ 100 Hz, which can be saved for further analysis. Radiation hardness of detector materials and electronics, especially close to the interaction point are mandatory to resist the large particle flux.

Aiming at a test of the standard model at the TeV scale, the discovery of the higgs-boson and other new phenomena like supersymmetry or extra dimensions, the detector must provide an excellent performance in particle reconstruction and identification.

Depending on the higgs mass a discovery is possible with signatures like four muons ($H \rightarrow Z^0 Z^0 \rightarrow \mu\mu\mu\mu$), 2 high energy photons ($H \rightarrow \gamma\gamma$), or in final states with b-jets ($H \rightarrow b\bar{b}$). Hence, muon reconstruction and charge identification with high efficiency and momentum resolution over the entire kinematic range, and in particular for high energetic muons is an important design goal. Further, the measurement of electromagnetic energy and diphoton masses must be excellent ($\sim 1\%$ at 100 GeV) and requires an efficient π^0 suppression.

Reconstruction of secondary vertices is crucial for the identification of b -jets and also of tau-leptons which may appear with high abundance in supersymmetric events. A high efficiency and precision in charged particle track reconstruction is essential for these purposes.

Still, the striking signature of supersymmetry is large missing transverse energy, which must be determined with good resolutions and further motivates the hermetic coverage of the interaction point. New resonances decaying via the strong interaction may be found in the dijet mass spectrum such that the dijet mass resolution, reached by a fine lateral segmentation, becomes important.

3.2.1 Coordinate System and Conventions

The coordinate system used in CMS is a right-handed system, centered at the nominal collision point, with the y -axis pointing vertically upward, the x -axis pointing radially inward to the center of the LHC ring, and the z -axis pointing in the beam-direction toward the Jura mountains.

The azimuthal angle ϕ is measured from the x -axis in the x - y -plane and the polar angle θ is measured from the z -axis. Pseudorapidity is then defined as $\eta = -\ln(\tan \frac{\theta}{2})$, the magnitude of the transverse momentum $p_T = (p_x, p_y)^T$ becomes $|p_T| = |\vec{p}| \cdot \sin \theta$, and the distance of two points in the η - ϕ -plane is given by $\Delta R = \sqrt{(\phi_1 - \phi_2)^2 + (\eta_1 - \eta_2)^2}$.

3.2.2 Superconducting Solenoid

The superconducting solenoid is 13 m long and with a diameter of 6 m it is large enough not only to accommodate the tracking device, but also the hadronic and electromagnetic calorimeter, such that the absorbing material in front of them is minimized. A field strength of 3.8 T in this dimensions can only be reached with a superconducting magnet. The strong field is necessary for the bending of charge particle trajectories, that allows a momentum measurement. Further more it saturates a sufficient amount of iron to embed the muon chambers in its flux return yoke.

3.2.3 Tracking Detectors

The inner most detector component is a silicon pixel detector, surrounded by a silicon strip tracker. Here the trajectories of charged particle are measured and their origins (vertices) are determined by analysis of the hits on the modules. The silicon detector combines a fine segmentation with radiation hardness and relatively low material budget, which is beneficial to reduce effects from multiple scattering, bremsstrahlung and photon conversion. Its layout is shown in figure 3.3.

With a length of 5.6 m and a radius of 1.25 m the tracker covers the pseudorapidity region up to $|\eta| < 2.5$. The total active area sums to about 200 m². A pixel structure was chosen for the innermost parts since an occupancy of single detector cells in the order of 1% had

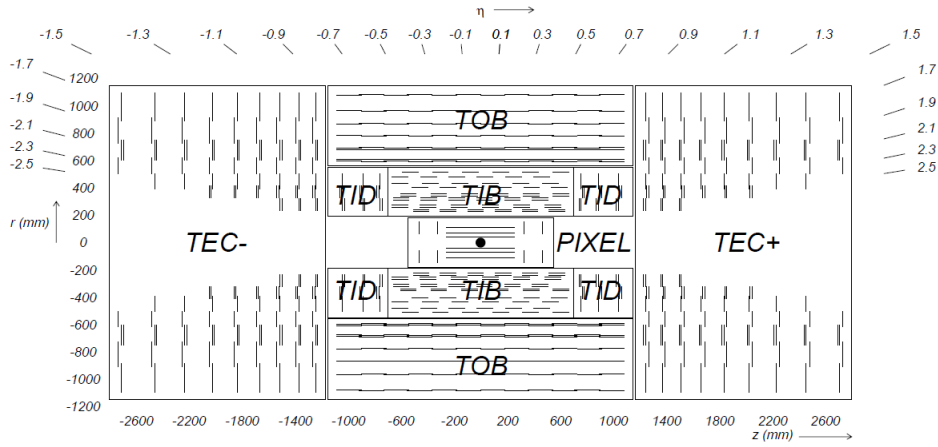


Figure 3.3.: Cross-section through the the silicon tracker [37]. Each line stands for a sensor module.

to be achieved, while having a hit rate density of e.g. 1 MHz/mm^2 at a radius of four centimeters.

Pixel Detector

The pixel tracker is divided into a 55 cm long barrel part with three layers of sensor modules, at radii of 4.4, 7.3, and 10.2 cm, and two layers of endcap modules, which are mounted on turbine-like wheels at $|z| = 34.5 \text{ cm}$ and $|z| = 46.5 \text{ cm}$ and have a radius of 15 cm. A total of 66 million pixels are distributed over the 1440 modules. Pixel dimensions are $100 \mu\text{m}$ in transverse and $150 \mu\text{m}$ in z -direction.

Its live time due to radiation damage is limited to approximately 2 years for the first pixel layer and greater than 10 years for the outermost in high luminosity LHC operations.

Strip Tracker

Further layers of active detector material are realized as silicon strip modules. In the central region 10 layers are arranged in inner (TIB) and outer barrel (TOB) with the strips oriented along the z -axis. The inner barrel is closed with the three layers of the inner disks (TID) and the tracker endcaps (TEC) provide additional 9 layers (disks) of sensor modules. Those in the inner disks and endcaps are placed perpendicular to the beam direction with strips pointing radially outwards.

Each substructure is partially equipped with back-to-back modules in which the strip directions of the two sensors are tilted by an angle of 100 mrad in order to allow for a measurement of the third hit coordinate.

Since the hit density falls with increasing distance to the interaction point, the pitch and length of the silicon strips can be increased accordingly to reduce the number of readout channels while keeping the occupancy low. The pitch increases from $80\ \mu\text{m}$ up to $180\ \mu\text{m}$ and the strip length from $10\ \text{cm}$ up to $25\ \text{cm}$. In order to keep the noise at a low level, the sensor thickness also increases from $320\ \mu\text{m}$ to $500\ \mu\text{m}$.

The tracker layout leads to approximately 3 hits in the pixel and 9 hits in the strip detector for a particle reaching the electromagnetic calorimeter. The amount of traverse material depends strongly on the pseudorapidity and reaches from $0.4\ X_0$ up to $1.8\ X_0$, with largest contributions, in decreasing order, from support structures, cables, cooling and electronics.

Tracker Performance

Transverse momenta of $100\ \text{GeV}$ are reconstructed with a resolution of 1-2% in the central region ($|\eta| < 1.6$). The reconstruction efficiency for single muons in this detector region reaches 99% and decreases in the forward region, where no layers of the inner disks are traversed. For pions the efficiency is degraded mainly due to multiple scattering to about 85%.

3.2.4 Electromagnetic Calorimeter

The electromagnetic calorimeter (ECAL) is build of lead-tungstate crystals (PbWO_4) and surrounds the tracker up to a pseudorapidity of $|\eta| = 3.0$. Lead-tungstate crystals were chosen because they have a short radiation length of $X_0 = 0.89\ \text{cm}$ and small Moliere radius ($2.2\ \text{cm}$), such that a compact geometry with fine granularity and good spatial resolution can be realized. Furthermore they are radiation hard and have a fast light emission.

In the barrel region ($|\eta| < 1.479$) crystals with surface dimensions of $2.2 \times 2.2\ \text{cm}^2$ and a length of $23\ \text{cm}$, corresponding to 25.8 radiation length, are mounted in a quasi-projective geometry (Fig. 3.4) with their surface pointing to toward the interaction point. The light emitted by the crystals is collected with avalanche photo diodes.

In the ECAL endcaps ($1.479 < |\eta| < 3.0$) the crystals have a length of $22\ \text{cm}$ ($24.7X_0$) and are connected to vacuum photo-triodes for readout. The endcap is partially shielded with a preshower detector, extending from $|\eta| = 1.653$ to $|\eta| = 2.6$. It consists of two lead plates of $2X_0$ and $3X_0$, respectively, interspersed with silicon strip detectors and allows for an identification of neutral pions.

For particle energies up to $500\ \text{GeV}$ the resolution σ is described by

$$\left(\frac{\sigma}{E}\right)^2 = \left(\frac{a}{\sqrt{E}}\right)^2 + \left(\frac{b}{E}\right)^2 + c^2$$

where a stands for a stochastic factor, b for the noise, depending e.g. on the luminosity,

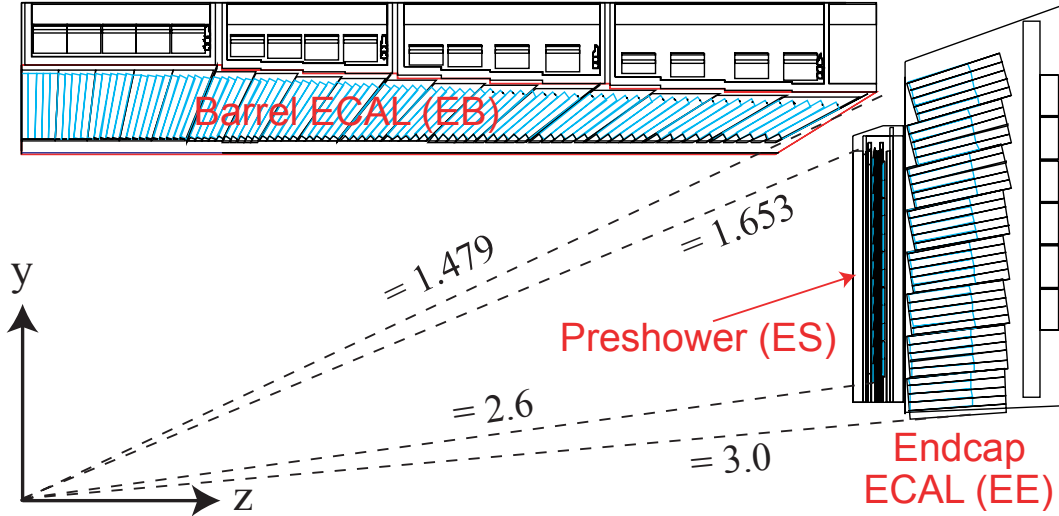


Figure 3.4.: One quarter of the ECAL showing the orientation of the crystals [37].

and c for an intrinsic constant contribution. Parameters were determined in an electron test beam setup of a barrel supermodule to $a = 2.8\%$, $b = 0.12$ and $c = 0.3\%$.

For higher energies showers leak out of the calorimeter's back and this parametrization becomes invalid.

3.2.5 Hadronic Calorimeter

The hadronic calorimeter (HCAL) consists of several detectors (Fig. 3.5). The barrel part (HB) is placed between the ECAL and the solenoid, which limits the amount of absorber material that can be used. The endcap (HE) detectors fit inside the remaining space at both ends of the magnet cylinder. The HCAL is completed by an additional active barrel layer outside the magnet (HO) and a forward component (HF).

Barrel and endcaps are both built from brass plates as absorber, plastic scintillator as active medium, wavelength shifting fibers and hybrid photo diodes for light detection.

In the barrel ($|\eta| < 1.3$) the absorber plates are about 5 cm thick and interleaved with layers of scintillator with a thickness of 3.7 cm each. The brass absorber material has an interaction length of 1.49 cm and a hadronic interaction length $\lambda = 16.42$ cm. At $\eta = 0$ the material sums up to only 5.82λ plus about 1.1λ from the ECAL, thus requiring the HO as a tail-catcher for higher energetic hadrons. The amount of traversed absorber material increases towards the forward region and reaches 10 interaction lengths. HB is segmented into 2304 towers with a size of $\Delta\eta \times \Delta\phi = 0.087 \times 0.087$.

In the endcaps ($1.3 < |\eta| < 3.0$) 8 cm thick absorber is used. The granularity is increased for $|\eta| > 1.6$ to $\Delta\eta \times \Delta\phi = 0.17 \times 0.17$ and towers have a longitudinal segmentation into

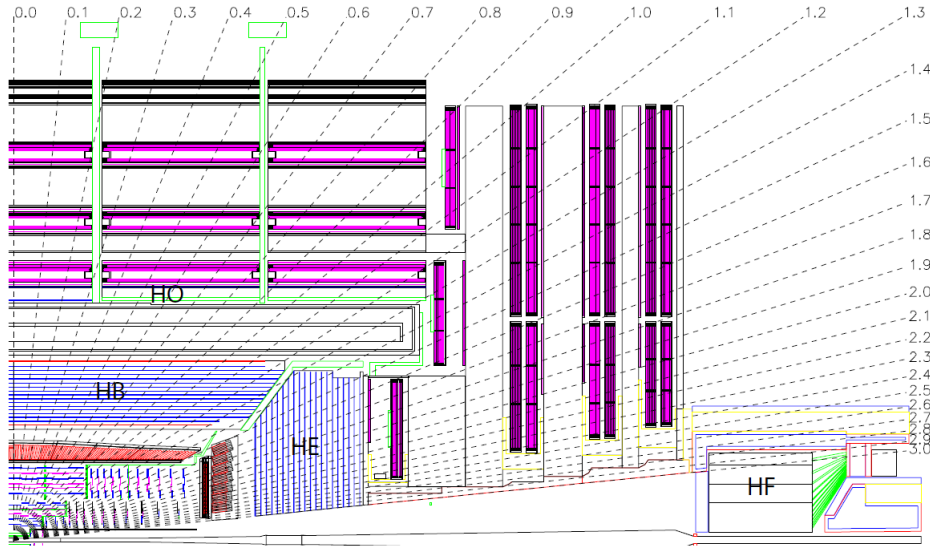


Figure 3.5.: Sketch of one quarter of the CMS detector, showing the position of the hadronic calorimeter components, namely the barrel (HB), endcaps (HE), outer (HO) and forward (HF) parts [37].

up to 3 divisions close to the beam line, where particle rates and energy depositions reach their maximum.

On the outer side of the solenoid cylinder, extending up to $|\eta| < 1.3$ an additional layer of scintillator serves as active medium behind the absorbing material of the magnet. The depth of the absorbing material depends on pseudorapidity and is approximately $1.4 \sin \theta$ interaction lengths. The HO segmentation is identical to the barrel.

For the most forward HCAL component (HF) robust steel absorber plates were chosen, instrumented with quartz fibers and photomultipliers for the detection of Cerenkov light. It is located 11.2 m away from the interaction point and covers the pseudorapidity region of $3.0 < |\eta| < 5.2$, where the radiation dose is extremely high, requiring such robust technology.

The HCAL performance in view of jet energy resolution is summarized in section 3.3.1.

3.2.6 Forward Detectors

The experimental setup is completed with two very forward detectors. Castor (CentauRO And Strange Object Research), located 14.38 m away from the nominal interaction point, covers the region of $5.2 < |\eta| < 6.6$. The Zero Degree Calorimeter (ZDC) measures neutral particles at a distance of 140 m ($|\eta| > 8.3$). Both are tungsten-quartz Cerenkov calorimeters for radiation resistance reasons and have 10 and 7 interaction lengths, respectively.

3.2.7 Muon System

Three different types of gaseous muon detectors are embedded in the flux return yoke of the CMS magnet, where the magnetic field still provides sufficient bending power to determine muon momenta (Fig. 3.6).

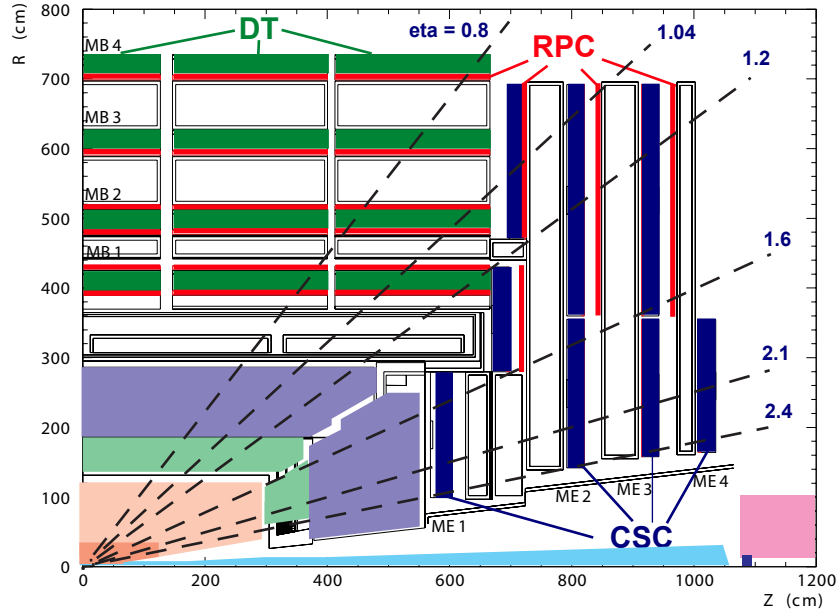


Figure 3.6.: Schematic view of one quarter of the CMS detector, showing the position and type of the muon chambers [36].

Following the geometry of the solenoid, muon chambers are placed parallel to the beam-axis in the four barrel muon stations and perpendicular in the endcap wheels, covering an area of about 25000 m^2 .

Drift tubes (DT) are used in the four barrel stations ($|\eta| < 1.2$), where neutron induced backgrounds are small and low muon rates are expected. Each of the three inner stations is equipped with four chambers measuring the r - ϕ -coordinate and four chambers for determination of the z -coordinate. Hit resolution is about $100 \mu\text{m}$.

In the four endcap stations more radiation resistant cathode strip chambers are installed because muon rates and background levels are higher and the magnetic field is large and non-uniform. They cover the pseudorapidity region of $0.9 < |\eta| < 2.4$ and provide a fast response time and fine segmentation.

The muon systems can be used to trigger on the muon transverse momentum with good resolution (15% (25%) for the barrel (endcap)). However, the uncertainty on background rates and in the determination of the correct bunch-crossing motivates the existence of a complementary set of muon detectors. The resistive plate chambers (RPC) have a lower

hit resolution, but very fast response and good time resolution and are especially suitable for triggering and bunch crossing identification. Six layers of RPCs are placed in the barrel and three layers in the endcap stations, covering $|\eta| < 1.6$.

Reconstruction efficiencies for single muons are typically 95-99%, only dropping in transition regions between different detectors. Multiple scattering before the muons stations limits the p_T resolution of the standalone muon system to about 9% for transverse momenta up to 200 GeV.

This can be improved significantly by combining measurements in the muon system with tracker information, especially beneficial at low p_T (cf. Sec. 3.3.4).

3.2.8 Trigger System and Data Acquisition

The LHC bunch crossing frequency of 40 MHz in combination with multiple interaction per crossing leads to a very large amount of data to be processed by the readout system. Since it is impossible to store the information of all events, a trigger system has to reduce the rate by a factor of 10^6 . The first trigger level (L1) is realized with programmable electronics and has an output rate of 100 kHz. The second level, called high level trigger (HLT), is a software trigger, i.e. it consists of a computing farm running the selection software. This gives the opportunity to use complex algorithms and evolve them in time. Data is finally transferred to the storage systems with rate of about 100 Hz [38].

The L1 trigger does not use the full detector information but only coarsely segmented data from the calorimeters and the muon system. During the L1 processing the readout data is stored in pipelines on the front-end electronics. In contrast, the HLT has access to the full detector information.

The L1 decision is taken in four steps (Fig. 3.7). First trigger primitives are generated from energy deposits in the calorimeter (trigger towers) and track segments or hit patterns from all three muon chambers types.

In a second step regional triggers combine pattern information to form and rank trigger objects like electron, photon or muon candidates. Information on minimum-ionizing particles and isolation properties is analyzed as well. The highest ranked objects are determined from the Global Muon and Global Calorimeter Trigger. The latter also calculates quantities like jets, their scalar p_T sum or the total (missing) transverse energy in the event. Finally, the Global Trigger takes a decision whether to accept or reject an event based on these objects.

The decision also takes into account the readiness of the subdetectors and the data acquisition system (DAQ). The DAQ system has to read out 1 MB per event, resulting in a data flow of 100 GeV/s at nominal LHC luminosity, which is passed to the HLT farm.

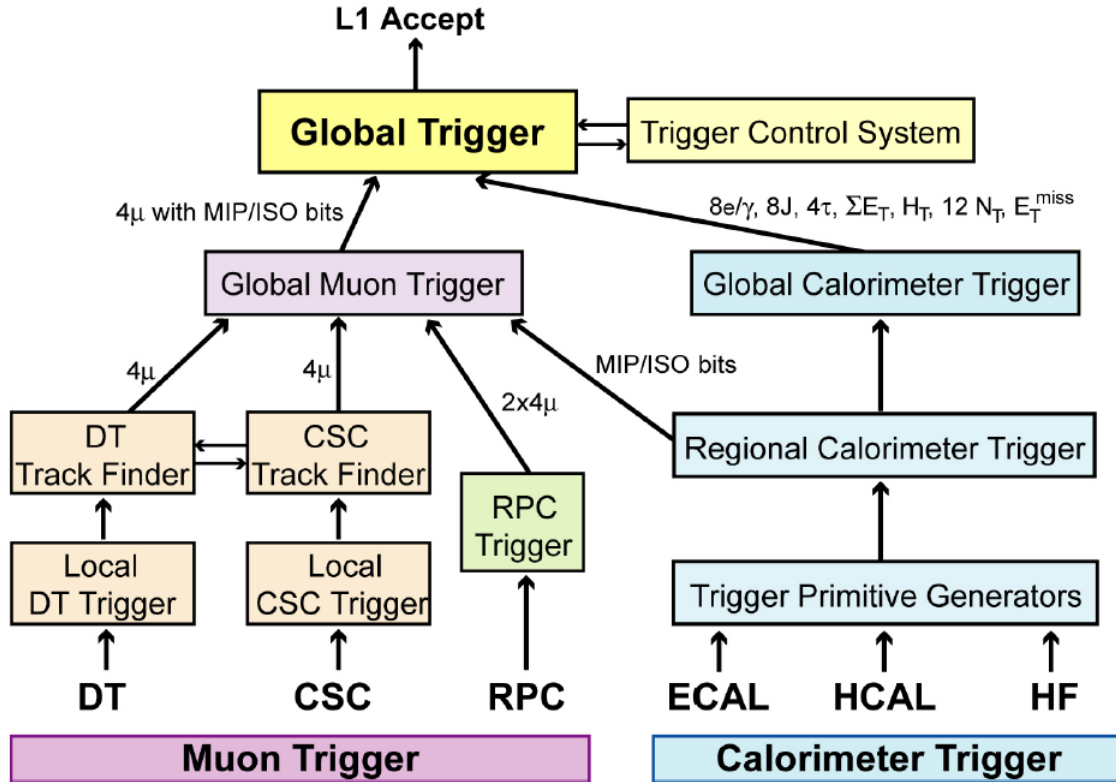


Figure 3.7.: Architecture of the L1 trigger [37].

3.2.9 Data Storage and Processing

The large amount of experimental data acquired with the CMS detector must be stored and made available for analysis. The computing system supports tasks like saving of raw and derived data, processing of pattern recognition and event filtering, data reduction, and the final physics analysis. Furthermore, large samples of simulated events are produced for comparison of data and theoretical descriptions. Data processing also requires the access to non-event data like detector conditions and calibrations.

Since these services cannot be provided at the required scale by single computing center, CMS, like the other LHC experiments, supports distributed computing in the Worldwide LHC Grid (WLCG) [39]. The WLCG is an association of computer centers around the world, connected via high-speed networks, which provide common interfaces (grid middleware) to their storage and CPU resources. The majority of the recorded data of all LHC experiments will be stored and analyzed outside CERN.

These sites are organized in a hierarchical *Tier* structure, and responsibility for the various computing tasks is distributed over three different levels (Fig. 3.8).

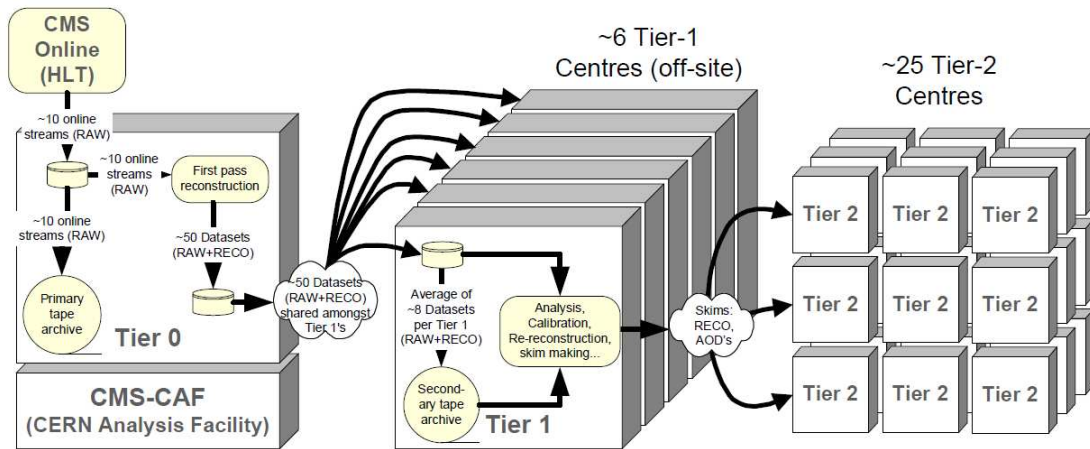


Figure 3.8.: Hierarchical structure and tasks of the CMS computing centers, also showing the data flow [37].

Tier-0 CERN hosts the only Tier-0 center, where the incoming data is stored and prompt reconstruction takes place. Data is then exported to Tier-1 sites.

Tier-1 Seven Tier-1 sites provide large batch CPU facilities and storage space to the collaboration. A tape archive is mandatory since each Tier-1 has custodial responsibility for a share of the recorded data. Tier-1 centers have direct network connections to the Tier-0. Second-pass reconstruction and skimming is carried out, simulated data is stored and data is passed down to Tier-2 sites for analysis.

Tier-2 The final physics analysis takes place at the Tier-2 centers on skimmed data obtained from the Tier-1. In the order of 100 sites, usually local university computing clusters, carry out his task. They are also in charge of production of simulated events, which are cached in the local storage before being transferred to a Tier-1 site. Special activities like calibration and alignment studies are also run at Tier-2 sites.

In reality a fourth category of Tier-3 centers exists. These are local university computing clusters with grid enabled storage and CPU resources, used for physics data analysis but without formal responsibilities in the collaboration.

A flexible and scalable software framework is crucial for efficient data processing. In CMS this is achieved with a modular system with loosely coupled components and well-defined interfaces. The software framework provides a central application in which modules for each particular data manipulation or analysis task can be plugged in. Complexities concerning e.g. reading and writing to files are hidden from the user. The framework imposes a data model where the event is the central entity. Communication between modules can

only happen through products written to the event. Every CMS application consists of a sequence of modules and their configuration. Provenance information for each product in the event is added automatically. All data is stored in ROOT files but with varying content:

- *RAW* contains the full recorded detector information, has a size of 1.5 MB/event and is permanently archived. The *RAW* data is divided into primary datasets by trigger information.
- *RECO* data already passed the reconstruction steps. Pattern recognition like cluster and track finding, vertex reconstruction, corrections and filtering are finished and reconstructed physics objects are stored in the event, which is reduced to 0.5 MB/event. Still it is possible to apply new calibrations or alignment with the available information.
- *AOD* (Analysis Object Data) is a compact (100 kB/event) data format obtained from *RECO* by filtering or skimming. It contains only high level physics objects and all information to refit their kinematics. Due to the small event size large datasets of *AOD* data can be stored at many sites

Non event data from construction (e.g. detector geometry), configuration, and run conditions like calibrations, alignment or detector status are kept in databases which can be accessed by CMS software applications.

In order to facilitate data handling and analyses on remote sites, various CMS specific grid related services are necessary. Data catalogs (*Data Bookkeeping Service*, *Data Location Service*, *Trivial File Catalog*) provide the mapping of dataset names to the hosting site and the actual location of data in the site's local file system.

A data transfer and management tool is used for the placement of data on the sites and for bookkeeping. Further workflow management tools are available for user-specific analysis job creation, submission and monitoring as well as for large scale job submission for reconstruction or simulation purposes.

The functionality of the CMS computing system was demonstrated in various tests before LHC startup.

3.3 Physics Objects Reconstruction

In this section the reconstruction algorithms for physics objects which are relevant in this study are summarized. These are jets, missing transverse energy, electrons and muons. From the signals of the numerous detector readout channels important information must be filtered out. Therefore pattern recognition algorithms are applied in the CMS reconstruction software in order to find detector regions where particles have passed after the

bunch crossing, to identify the type of the particles and to reconstruct their momenta. In most cases several subdetectors are involved in the detection of a particle.

3.3.1 Jets and Missing Energy

Hadronizing quarks and gluons form jets of hadrons in the detector, which are stopped in the calorimeters. The traditional jet reconstruction relies only on calorimeter information, while more sophisticated approaches, which use additional information from the tracking detectors or are based on particle-flow reconstruction [40], are a competitive or even superior alternative.

In the classic approach, cells from the hadronic and electromagnetic calorimeters are combined into so-called towers. Towers are basically η - ϕ -bins, resembling the HCAL granularity, whose energy content is determined by summing up all included cells above a noise threshold.

The basic idea of the particle-flow approach is the reconstruction and identification of all stable particles in the event [41]. Beside electrons, muons and photons this also includes charged and neutral hadrons. Exploiting measurements of all CMS subdetectors a list of individual particles in the event is created, which serves as input to the particle-flow jet clustering and missing transverse energy determination.

Several clustering algorithms to combine the identified particles or calorimeter towers into jets are available and used in the CMS reconstruction software, like cone, kT and anti-kT algorithms. In this work particle-flow jet reconstruction is used, choosing the anti-kt clustering algorithm [42] with a parameter $R = 0.5$.

Jet Energy Corrections

The energy of reconstructed jets needs to be calibrated to the incident particle's energy since the detector response is not perfect. In CMS a factorized approach was chosen, consisting of several levels of jet corrections. Calibration factors are usually derived from Monte Carlo simulation or collisions data using $2 \rightarrow 2$ processes, like dijet, γ +jet and Z +jet events. In such processes the fact that the two objects have to be balanced in the transverse plane can be exploited to calibrate the jet. The levels of jet corrections are sketched in the following. [43]

- An offset correction removes the contribution of electronic noise and pile-up. The average cell-energy measured in zero-bias events is subtracted from the towers. The magnitude of this correction grows with increasing luminosity, when the number of interactions per bunch crossing becomes higher.
- The relative correction in pseudorapidity flattens the energy response which initially is not uniform. This is usually done using dijet balance events.

- An absolute correction of the transverse momentum establishes the correct energy scale. Technically, a comparison of a jet to a balancing object measured in the more precise ECAL, tracker and muon system is made. Muons from Z -bosons decays or photons are commonly used.

More optional corrections exist but were not applied to the jets used in this work.

- EMF correction (Electromagnetic fraction): CMS calorimeters are non-compensating, i.e. their response is different for hadrons and electrons/photons. The measured jet energy depends on the relative content of electrons and photons in the jet, which are stopped in the ECAL and it has to be corrected for this effect.
- Flavor corrections: Different fragmentation in gluon and light-quark jets as well as neutrinos from semileptonic decays of heavy quarks inside jets can be compensated by flavor specific corrections. However, these depend on the assumed process and require an event interpretation.
- Underlying Event: A correction for the energy from underlying event, i.e. soft interactions involving spectator partons.
- Parton: The jet can be corrected to match the incident parton energy level.

Performance of Jet Reconstruction

Jet resolutions are strongly dependent on the jet transverse momentum and the pseudorapidity region in the detector. Typically they are determined in bins of these two variables and their evolution from low to high transverse momenta in a certain η -bin is fitted with a resolution function. For jets including tracking information this formula reads [44]

$$\frac{\sigma(p_T/p_T^{\text{gen}})}{\langle p_T/p_T^{\text{gen}} \rangle} (p_T^{\text{gen}}) = \sqrt{\text{sgn}(N) \cdot \left(\frac{N}{p_T^{\text{gen}}}\right)^2 + S^2 \cdot (p_T^{\text{gen}})^{M-1} + C^2}, \quad (3.4)$$

and contains a noise term (N), a constant term (C) and a stochastic term (S), which is modified by a fourth parameter (M) in order to account for the fact that the response does not follow the same form as in case of a pure calorimetric jet measurement.

The relative jet p_T resolution for particle-flow anti-kt ($R = 0.5$) jets, determined from Monte Carlo simulation as a function of the generated p_T is given in Tab. 3.1

Only in case of high p_T the particle-Flow jet energy resolution is dominated by the energy resolution of the hadronic calorimeter. The inclusion of tracking information limits the degradation of the resolution when going towards lower transverse momenta.

Pseudorapidity	N	S	M
$0.0 < \eta < 0.5$	3.97	0.18	0.63
$0.5 < \eta < 1.0$	3.55	0.24	0.53
$1.0 < \eta < 1.5$	4.55	0.23	0.59
$1.5 < \eta < 2.0$	4.63	0.24	0.49
$2.0 < \eta < 2.5$	2.53	0.34	0.29
$2.5 < \eta < 3.0$	-3.34	0.73	0.08
$3.0 < \eta < 5.0$	2.95	0.12	0.96

Table 3.1.: Jet p_T resolution parameters for anti-kt ($R = 0.5$) particle-flow jets [45]. The constant term C of Eq. 3.4 was fixed at zero.

3.3.2 Missing Transverse Energy

Missing transverse energy² is calculated as the p_T of the negative fourvector sum of all particles found in the particle-flow event reconstruction.

$$p_T = \sqrt{\left(\sum_i p_x^i\right)^2 + \left(\sum_i p_y^i\right)^2} \quad (3.5)$$

So-called *Type I* corrections are applied, which propagate the individual jet energy correction factors to the missing E_T .

3.3.3 Electrons

The reconstruction of electron candidates proceeds in several steps [46]. First a pattern recognition algorithm is applied to search for clusters of active ECAL cells. These clusters are then merged into superclusters which extend along ϕ to include Bremsstrahlung photons, radiated during the flight through the tracker material. In order to find compatible hits in the tracking detectors a trajectory is extrapolated through the magnetic field from the supercluster position toward the interaction point. Compatible hits are finally fitted to form the electron track.

Electron Identification

Additional quality criteria have to be applied to filter the obtained electron candidate collection, since the ECAL energy deposition of jets, photons or single pions, which accidentally matches to a good track, is frequently reconstructed as an electron (*fake electrons*). Several

²Strictly speaking the name missing E_T is wrong. However, the difference between transverse energy and transverse momentum is negligible because particles' masses are small compared to their typical momenta.

selections with distinct properties concerning efficiencies and fake rates are available in the CMS software [47]. They are either cut based using neural network, all using the following variables.

- The ratio of energy deposited in the hadronic and electromagnetic calorimeter H/E , which separates hadrons.
- Matching between the energy of the supercluster and the electron track momentum, measured at the vertex or at the calorimeter E/p . This quantity should be close to unity for electrons since their mass is negligible and all energy is deposited in the ECAL.
- Geometrical matching between the electron track parameters at the vertex extrapolated to the super cluster and the measured supercluster position ($\Delta\phi_{in}$ and $\Delta\eta_{in}$)
- Calorimeter shower shape variables, characterizing the the width of the ECAL cluster ($\sigma_{in\eta}$, \sum_9 / \sum_{25}).

In addition electrons from photon conversion are rejected by a cut on the impact parameter and a limit on the number of layers crossed by the track, which do not show hits.

Another requirement can be the isolation of the electron object in one or several detector components. For isolation further restrictions are applied on the number, energy or transverse momentum of other particles within a (hollow) cone around the candidates fourvector direction. Isolation can be calculated for the tracker, the electromagnetic, and the hadronic calorimeter.

Performance of Electron Reconstruction

Electron reconstruction performance depends strongly on the required quality criteria and is always a trade-off between efficiency and purity. For the electron selection used in this work (Loose Fixed Threshold [48]) an efficiency of 98% for electrons with $p_T > 10$ GeV is reached in $Z \rightarrow ee$ and $W \rightarrow e\nu$ events. The efficiency is approximately uniform in pseudorapidity. The selection purity was found to be 92% for $Z \rightarrow ee$ and 89% in $W \rightarrow e\nu$ events in a scenario including tracker misalignment. The achieved momentum resolution for electrons is of the order 2-5%.

3.3.4 Muons

Muon reconstruction [49] starts in the dedicated muon chambers where hits are combined into track segments, which serve as seed for a first trajectory search. The algorithm looks for hits in all layers of the muon system, including the RPCs and performs a track fit. The track extrapolation towards the interaction point must be compatible with the interaction point within $\Delta x = \Delta y = 15 \mu\text{m}$, $\Delta z = 5.3$ cm, what corresponds to the 1σ bunch width

and length. In so-called global muon objects the reconstructed track from the muon system is combined with hits in the inner tracker. Hits from different silicon layers in the region of interest around the extrapolated trajectory are analyzed and compatible ones enter a global track refit to tracker and muon system hits. Like in the case of electrons isolation quantities in the tracker and calorimeter are defined and can be used for a further selection.

Performance of Muon Reconstruction

Muon reconstruction in CMS is highly efficient, reaching more than 98% for muons with $p_T > 10 \text{ GeV}$ and degrading slightly to 96% for 1 TeV muons. Furthermore global muons have a very high purity. Fake muons from punch-through of high p_T jets and secondary muons from heavy flavor decays inside jets can further be reduced by tight quality cuts [50]. The probability for a correct charge assignment is above 75% for TeV-muons and increases to 99% for lower p_T muons. Exploiting the power of the full tracking system the probability stays above 98%, even for TeV-muons. A momentum resolution of a few percent is reached, which depends on the muon momentum. It becomes worse toward the forward direction and approaches 10% for 1 TeV muons in the pseudorapidity region. $1.2 < |\eta| < 2.4$ (Fig. 3.9).

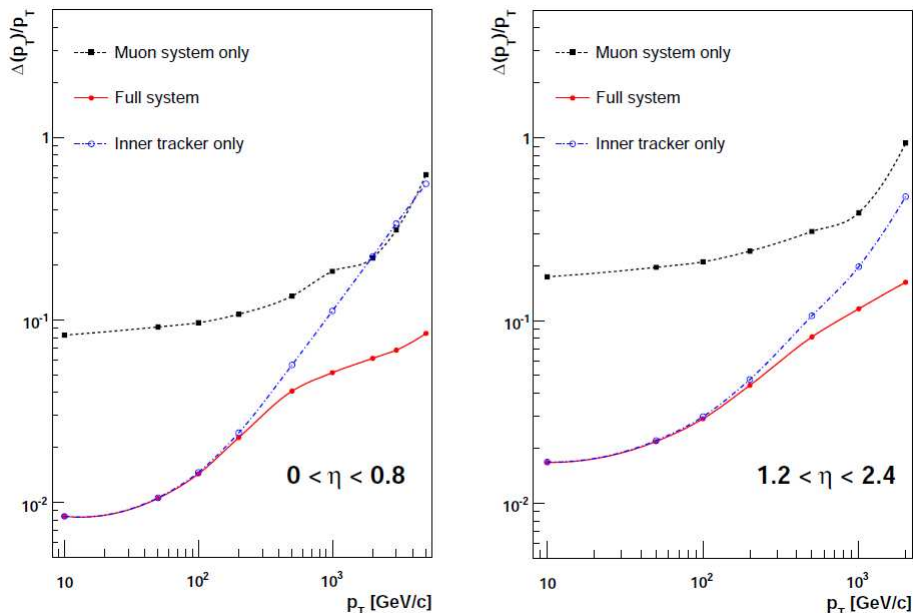


Figure 3.9.: Muon p_T resolution in two pseudorapidity bins as a function of the transverse-momentum using the muon system only, the inner tracking only, and both [37].

3.3.5 Event Simulation

The CMS software framework for event simulation and reconstruction (CMSSW [36]) provides interfaces for all common Monte Carlo event generators, like Pythia [51], Alpgen [52], Sherpa [53] and others, which calculate the hard scattering processes. Also the fragmentation and hadronization of gluons and quarks, as well as the decay of unstable particles is handled by these external codes. Their outcome is fed to the CMS detector simulation module in the HEPMC [54] format.

The CMSSW modules then simulate the interactions of particles with the detector material, the electronics response and readout and, in exactly the same way as for collisions data, the reconstruction of physics objects as described above.

For the simulation part two different codes exist within CMSSW. The GEANT 4 [55] based *full* simulation provides a detailed Monte Carlo simulation of the interactions of particles with the detector material and the electronics response.

The fast simulation package (FastSim) uses a simplified architecture and parametrized responses of detector components for the simulation of event signals. It is constantly tuned to the detailed GEANT based simulation and in future as well to data. The main advantage of the fast simulation is the reduced CPU consumption, which is about 100-1000 times lower than for the full simulation [56]. In both approaches pile-up events can be added to the detector signal. While the simulation of the electronics signal is different, both codes rely on the same high-level algorithms to reconstruct the physics objects.

Chapter 4

The Mass Determination Problem

In this chapter methods for mass determination are summarized and a new method based on kinematic fits is introduced. Furthermore the benchmark point chosen for the mass determination study and its characteristics are discussed.

4.1 Motivation

Knowing about the good prospects for a discovery of supersymmetric particles at the LHC (c.f. Sec. 2.3.2) it is worth considering the next steps following a discovery, i.e. the determination of the underlying theory. It might be difficult to tell, whether the observed new particles really are of supersymmetric nature. Measuring their properties, like spin, charge or mass, will be necessary to reveal the correct theoretical description.

Finding the correct SUSY model is not an easy task since the SUSY parameters are often defined at a high energy scale (e.g. GUT scale), while observations are taking place near the electro-weak (TeV) scale. The evolution of the parameters and particle properties, like masses, from the high to the low scale is described by the renormalization-group equations, but unfortunately there is no unique mapping the other way round, from the observed quantities to the high energy parameters [57].

A promising approach to SUSY parameter determination are global fits of physical observables to SUSY models, i.e. statistical tests of the compatibility of measurements with predictions derived from a certain parameter choice in a SUSY scenario. This method was successfully demonstrated by e.g. the SFitter [58] and Fittino [59] and Mastercode [60,61] groups.

For each choice of parameters the SUSY spectrum at the weak scale is calculated using common RGE implementations. The agreement with standard model observables and future SUSY measurements is quantified, e.g. using a least squares minimization. This way conclusions about the parameters and the underlying model can be made.

Typical SUSY related input variables are mass edges, i.e. endpoints in invariant mass spectra (cf. Sec. 4.2), branching fractions, cross-sections and productions rates for various

LHC final states. Furthermore, Standard Model measurements like precision observables from the LEP experiments, beauty or kaon physics or the anomalous magnetic moment of the muon are used. Important cosmological constraints come from relic density observations.

In these approaches a measurement of absolute SUSY particle masses could as well contribute to a successful application.

4.2 Approaches to Mass Determination

The existence of two invisible particles in R-parity conserving supersymmetry makes mass determination a very challenging task. There is no possibility to reconstruct invariant masses of the decaying particles directly from the measured final state.

Nevertheless, a variety of methods for mass determination was proposed during the last years [62,63]. The proposals vary from an approximate SUSY mass scale determination to sophisticated procedures to reconstruct entire decay cascades with all involved masses and invisible particles.

The first category of methods uses kinematic variables and their correlation to the SUSY mass scale. From the observed distribution in collision data the mass scale can be estimated via a comparison to Monte Carlo simulations. An example for these simple approaches is the effective mass variable, defined as the mass of the fourvector sum of final state particles plus the missing (transverse) energy [64,65]

A more direct mass determination is possible with the *transverse mass* variable M_{T2} [66]. It is inspired by the transverse mass as used in the determination of the W -boson mass. It provides a possibility to determine the mass of the primary sparticles produced in the hard interaction. The complication of two escaping LSPs requires a slightly different definition with respect to the original transverse mass, such that it includes their missing momenta. Usually the variable is minimized over all possible values of total missing transverse momentum. While the endpoint of the distribution yields an estimate of the mass of the decaying particle it unfortunately depends on the LSP mass. Several variations on the definition of the mass variable can be found in the literature.

The dependence on the LSP mass can be overcome by looking at the endpoint of the transverse mass as function of a trial LSP mass. A kink can be observed at the exact value of the two unknown masses [67]. This methods need very high statistics samples and backgrounds have to be small.

A second and well established method is the measurement of mass edges and kinematic endpoints [64,68–70]. The distributions of invariant masses of measured final state particles show a typical structure with edges at the lowest or highest allowed values. The endpoints are related to absolute or relative mass differences of the decaying on-shell particles. By combination of several measurements of this kind, the absolute masses can be determined.

This determination can even be improved by incorporating event-wise information like the momentum balance [71] in a fit. It was shown, that mass edges can be interpreted in a wider context of mass related observables. Instructions of how to construct other such observables, based on general considerations were proposed [72].

The best known example of an edge in an invariant mass distribution is the dilepton edge in the neutralino decay

$$\tilde{\chi}_2^0 \rightarrow \tilde{l}_R(+l_1) \rightarrow \tilde{\chi}_1^0(+l_2)$$

where l can be any lepton flavor and \tilde{l}_R the corresponding slepton.

The invariant mass distribution of the lepton pair (m_{ll}) turns out to have a triangular shape ending at the maximum value, which is related to all three involved masses [70]

$$(m_{ll}^{max})^2 = \frac{(m_{\tilde{\chi}_2^0}^2 - m_{\tilde{l}_R}^2)(m_{\tilde{l}_R}^2 - m_{\tilde{\chi}_1^0}^2)}{m_{\tilde{l}_R}^2}. \quad (4.1)$$

Detailed studies exist for the detection of this mass edge with early LHC data [73], which show that a precise measurement is feasible.

All of these approaches do not require the explicit reconstruction of the LSP momenta. In contrast, the last group of methods is based on the reconstruction of the entire decay chains in an event, hence relying on the clean selection of a certain event topology. As the method presented in this thesis falls into this category, the principles will be discussed in detail here. These methods are sometimes called *polynomial methods*.

4.2.1 Decay Chain Reconstruction and Mass Determination

The key issue in event reconstruction is the determination of the LSP momenta. If they are known, the masses of the decaying particles are given by the invariant masses of the decay products, which always include an LSP.

A possibility for a momentum determination lies in the utilization of an event hypothesis. An event hypothesis means an assumption about the decay topology and implies a number of kinematic constraints, which follow from four-vector conservation at the vertices in the decay chain.

Let us consider the specific event topology shown in Fig. 4.1. Two particles (A/A') are produced in the collision, which then decay via the states (B/B') and (C/C') into the LSPs (D/D'). While the LSP cannot be detected the Standard Model decay products occurring in the sequence (f_i) are measured in the detector if they are charged leptons or jets. Neutrinos may also occur as decay products but this case will not be considered here, since this means a further complication due to three more unmeasured momentum components per neutrino.

The conservation of the four-momentum at the decay vertices (0-5) leads to six so called invariant mass constraints, by taking the square of the four-vectors. For the first decay

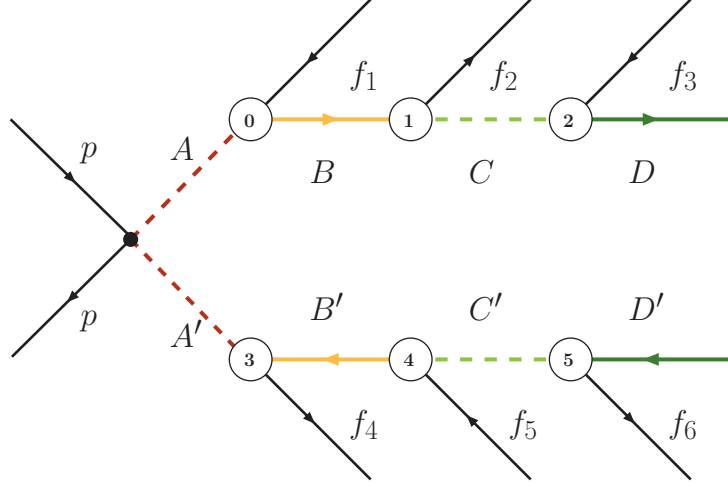


Figure 4.1.: Example for a decay chain involving several intermediate heavy particles. The f_i denote measured final states, while capital letters stand for SUSY particles. The particle D (D') stands for the invisible LSP.

branch this yields the following equations, where p stands for the four-vector of the corresponding particle.

$$\begin{aligned}
 (p_D + p_{f_3})^2 &= p_C^2 = M_C^2 & (4.2) \\
 (p_D + p_{f_3} + p_{f_2})^2 &= p_B^2 = M_B^2 \\
 (p_D + p_{f_3} + p_{f_2} + p_{f_1})^2 &= p_A^2 = M_A^2
 \end{aligned}$$

In addition the LSP must be on-shell.

$$p_D^2 = M_D^2 \quad (4.3)$$

The second decay branch is described by

$$\begin{aligned}
 (p_{D'} + p_{f_6})^2 &= p_{C'}^2 = M_{C'}^2 & (4.4) \\
 (p_{D'} + p_{f_6} + p_{f_5})^2 &= p_{B'}^2 = M_{B'}^2 \\
 (p_{D'} + p_{f_6} + p_{f_5} + p_{f_4})^2 &= p_{A'}^2 = M_{A'}^2 \\
 p_{D'}^2 &= M_{D'}^2.
 \end{aligned}$$

Two further constraints are obtained from the assumption, that the entire event should

have zero transverse momentum.³ The equations read

$$\begin{aligned} p_{f_1}^x + p_{f_2}^x + p_{f_3}^x + p_D^x + p_{f_4}^x + p_{f_5}^x + p_{f_6}^x + p_{D'}^x &= 0 \\ p_{f_1}^y + p_{f_2}^y + p_{f_3}^y + p_D^y + p_{f_4}^y + p_{f_5}^y + p_{f_6}^y + p_{D'}^y &= 0 \end{aligned} \quad (4.5)$$

Note, that the four-momenta of the invisible particles D and D' appear in the formulae. Therefore one can consider this as a system of 10 equations with a number of unknowns. Considering the case of two identical decay chains the unknowns are

1. 2×4 LSP four-momentum components, which are event specific.
2. 4 masses of the particles A, B, C, D , which are the same for each event having the same topology.

In the following the first category of parameters will be called *local* unknowns while the masses will be referred to as *global* unknowns. Counting 10 equations and a total of 12 unknowns for this cascade it is not possible to solve this system of equations but there are two ways to overcome this problem.

The first one was chosen by Cheng et al. [74]. Exploiting the fact that global unknowns are common to all events, they combine pairs of two events to obtain a problem with $2 \times 8 + 4 = 20$ unknowns and $2 \times 10 = 20$ constraint equations. As the equations are nonlinear several complex solutions exist, which must be found numerically. Taking only solutions with real values the histogram of the obtained mass values for many pairs of events shows peaks at the positions of the true particle masses.

Another approach makes use of mass hypotheses to find a solution of the unmeasured LSP momenta. This ansatz is used by Webber [75] and as well in this work. By making assumptions about the involved SUSY masses the number of unknowns is reduced to 8 per event, thus being smaller than the number of constraints. Hence, the LSP momenta can be determined by solving the system of equations. Not all equations have to be used as their number is larger than the number of unknowns in the specific topology of Fig. 4.1.

A smart way to solve for the LSP momenta was presented in [75] and is discussed here in some detail since we will make use of this solution in our work. The constraint equations (4.2 – 4.5) are rewritten as linear functions of the unmeasured four-momenta $p_D/p_{D'}$ by expanding the left side of the equation and substituting any squared terms by the mass values, which of course are hypothetical in case of the SUSY particles. So, using $p_D^2 = M_D^2$

³This is true only approximately because initial and final state radiation may cause a significant deviation at a high energy hadron collider like the LHC. This problem is discussed further detail in Ch. 7

one obtains

$$\begin{aligned}
 -2 \cdot p_{f_1} \cdot p_D &= M_B^2 - M_A^2 + 2 \cdot p_{f_1} \cdot p_{f_2} + 2 \cdot p_{f_1} \cdot p_{f_3} + m_{f_1}^2 \equiv S_1 \\
 -2 \cdot p_{f_2} \cdot p_D &= M_C^2 - M_B^2 + 2 \cdot p_{f_2} \cdot p_{f_3} + m_{f_2}^2 \equiv S_2 \\
 -2 \cdot p_{f_3} \cdot p_D &= M_D^2 - M_C^2 + m_{f_3}^2 \equiv S_3
 \end{aligned} \tag{4.6}$$

Equivalent expressions S_5, S_6 and S_7 , depending on the momentum of D' , can be obtained for the second decay branch.

Furthermore the transverse momentum balance can also be read as a function of the unmeasured momenta.

$$\begin{aligned}
 p_D^x + p_{D'}^x &= p_{miss}^x \equiv S_4 \\
 p_D^y + p_{D'}^y &= p_{miss}^y \equiv S_8
 \end{aligned} \tag{4.7}$$

Together these eight expressions form a linear system of equations for the 8 components of the D and D' four-momenta and can thus be solved analytically, e.g. by matrix inversion. Details of the solution are given in [75].

The solution yields values for the unmeasured momenta which fulfill the above equations but note that they do not fulfill the original mass constraints (4.2) and (4.4), unless $p_D^2 = M_D^2$ holds which is not required in the solution. In contrast, the deviation $p_D^2 - M_D^2$ can be used as statistic to test how well the mass hypothesis fits to the events under investigation. By searching the mass space (M_A, M_B, M_C, M_D) for the minimal deviation, summed over all events, the masses can be determined.

4.2.2 The Kinematic-Fits-Method

The ansatz followed in this work is slightly different. Again a mass hypothesis is used to solve for the local unknowns in the events, but in contrast to the method of Webber presented above, all available constraints are used at the same time.

A well established technique to exploit such over-constrained topologies are kinematic fits. In a kinematic fit the measured parameters are varied such, that the constraint equations are fulfilled and at the same time the sum of the relative quadratic deviations from the originally measured values (residuals) is minimized, taking into account the size of the uncertainty for each measurement.

An example is the usage of the W -boson mass constraint in a fit of top-quark events, where an improvement of the top-mass resolution can be achieved. Even more similar to the SUSY problem is the situation of semi-leptonic top-pair events, where the unmeasured momentum components of the neutrino are extracted from the fit. However, this situation still is less complex than a SUSY event, since there is only one unmeasured particle and its x - and y -momentum can already be deduced from the transverse momentum balance.

In this work the kinematic fit approach is extended to the SUSY topology described above. This method was already studied for a hadronic final state and a different fit implementation in [76]. For each event a kinematic fit can be performed if a mass hypothesis is specified. The goodness of fit is given by the quadratic sum of the residuals which should follow a χ^2 -distribution with 2 degrees of freedom (dof) in our case. The number of dof is obtained by subtracting the number of unknowns (8) from the number of constraints (10). Now, the event hypothesis can be varied and the χ^2 -value can be taken as a measure for the degree of compatibility with the true masses.

However, a single event does not have the discriminating power to decide which are the true masses. It merely defines a hyperplane in the mass space which fits to this specific event. Only by combining several events a distinction between good and bad mass hypotheses becomes possible. The expectation is that for an ensemble of events the average χ^2 -value is smallest when testing the correct masses in the fit (Fig. 4.2). The details how

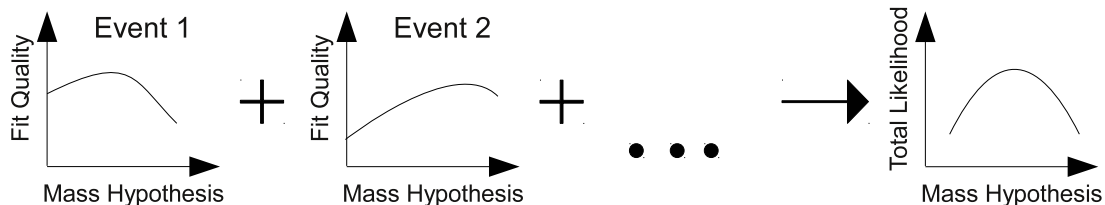


Figure 4.2.: Schematic view of the combination of event-wise mass scan for mass determination.

this combination is realized is described in Ch. 7.

Note that experimental uncertainties are included in the fit by using the full covariance matrix of the measured parameters. This contrasts with other available mass determination methods based on event reconstruction, where these experimental uncertainties are not taken into account.

If the constraints are non-linear, like the mass constraints given above, the fit must use an iterative procedure (c.f. Sec. 6.1). This contrasts with the analytical approach chosen by Webber.

Details on implementation and performance of this new method are given in the next chapters. First the setup in terms of SUSY scenario and decay chain is discussed in the following sections.

Chapter 5

Physics Scenario

5.1 SUSY Benchmark Scenario

The mSUGRA benchmark point SPS1a is chosen for this study. It belongs to a set of benchmark points, covering a wide range of possible signatures and event properties, which were defined to facilitate the comparison of phenomenological studies in the HEP community [77]. As other studies concerning the determination of SUSY masses in leptonic channels [74,75] made use of the SPS1a benchmark point, it seems an appropriate choice for the demonstration of the kinematic fit method and allows a direct comparison with the results of other groups. The SUSY parameters of SPS1a are given in Table 5.1.

The chosen benchmark is a "typical" mSUGRA point with rather low masses and by now is excluded from collider experiments (cf. Sec. 2.3.2). Nevertheless, using this benchmark point permits a direct comparison to previous mass determination studies. With its intermediate $\tan\beta$ it lies in the bulk of the cosmologically preferred region [78,79]. The Prospino [80] next-to-leading order cross-section is about 42 pb.

Figure 5.1 shows the mass spectrum of the SPS1a as obtained from Pythia [51], given the mSUGRA parameters. The actual masses obtained for the benchmark point depend slightly on the specific code used for the calculation [81,82].

The masses in the spectrum reach up to 600 GeV and the gluino is the heaviest sparticle. All squarks have slightly lower masses, around 550 GeV, despite the light stop quark, which has a mass of only 400 GeV. It is the only squark reaching down into the mass region of the two heaviest neutralinos and the almost mass degenerate heavy chargino. All sleptons reside below the squarks in the mass hierarchy.

The spread of the various neutralino and chargino masses, interleaved with the left- and

m_0	$m_{1/2}$	A_0	$\tan\beta$	sign μ
100 GeV	250 GeV	-100 GeV	10	+

Table 5.1.: mSUGRA parameters of the benchmark point SPS1a.

right-handed slepton masses opens up a large variety of decay chains with leptons in the final state. The lightest neutralino is the LSP, which is a common mSUGRA feature.

While in most cases right-handed squarks decay directly into the LSP, the left-handed types initiate decay chains involving charginos and/or neutralinos. Suitable decay chains for mass determination are discussed in the following section.

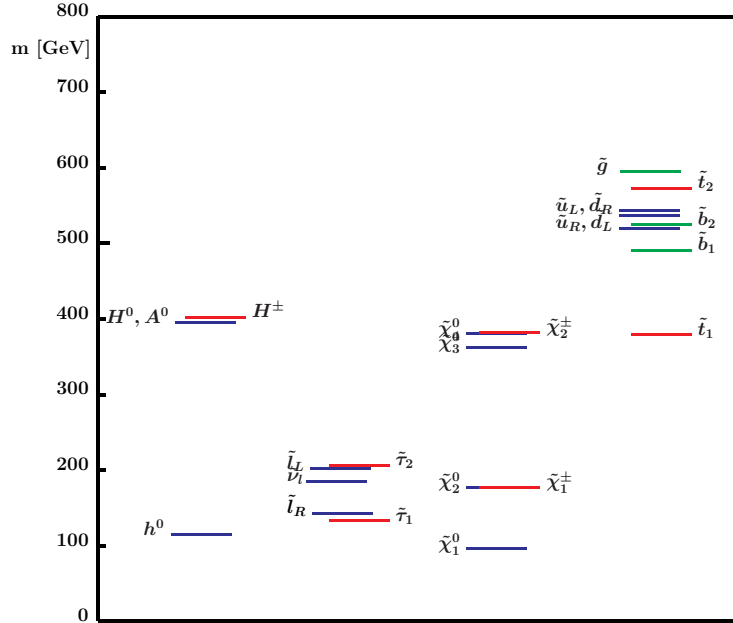


Figure 5.1.: Spectrum of sparticle masses at the SPS1a benchmark point [77].

5.1.1 Suitable (Leptonic) Decay Chains

The new mass determination method is based on an event topology which is over-constrained, i.e. in which more constraints than unmeasured momentum components are available. This defines which kind of events can be used: Having $2 \times 4 = 8$ LSP momentum components at least 9 constraints must be available. Assuming transverse momentum balance, giving 2 constraints, at least 7 mass constraints and hence 5 intermediate mass states are required.

Beside the minimum length of the decay chain other considerations play an important role in the choice of a suitable decay cascade. The signature, i.e. the Standard Model final states of the decay, can either be chosen as fully hadronic and consist only of jets or be partially leptonic if slepton and gaugino decays involving electrons and muons are preferred. Decays into tau-leptons fall into a special category, as taus decay further and the signature depends on the actual decay mode.

The decision for a fully hadronic or leptonic decay mode should take into account a number of advantages and disadvantages:

- Branching ratio: the branching ratio is generally larger for hadronic decays.
- Object resolution: electrons and muons can be reconstructed in the detector with higher precision than jets, for which a larger uncertainty on the energy scale and a worse resolution of the transverse energy have to be taken into account. This may reflect in the final precision of the mass determination.
- Combinatorics: in the event reconstruction all final state particles must be assigned to a position on the decay branches. Having only one type of particles (jets) yields a large number of possible permutations which grows factorially with the number of particles. Including leptons in the signature the combinatorial factor is much smaller.
- Backgrounds from other SUSY processes: signatures are not unique to a certain topology, because many different SUSY decay channels are possible. The more leptons in the final state the less channels are contributing.
- Backgrounds from Standard Model processes: Cross sections for standard model processes can be orders of magnitude larger. Especially for QCD-like, fully hadronic signatures the background can be overwhelming. For more exclusive channels with several leptons backgrounds are smaller and might even become negligible.

These considerations lead to a cascade, that ideally contains as many leptons as possible. Analyzing the branching ratios at the SPS1a point one finds the following situation:

- About 40% of the gluinos decay into a \tilde{q}_R ($\tilde{q} = \tilde{u}, \tilde{c}, \tilde{d}, \tilde{s}$), which almost exclusively decay into the LSP (>98%). First or second generation \tilde{q}_L and the lighter \tilde{b}_1 are each found in 20% of the gluino decays. The remaining fraction of 20% goes in almost equal shares into \tilde{b}_2 or \tilde{t}_1 but not into \tilde{t}_2 .
- The decay of \tilde{q}_L proceeds dominantly in two channels: roughly 60% go into $\tilde{\chi}_1^\pm$ and 30% into $\tilde{\chi}_2^0$. In case of \tilde{b}_1 the chargino fraction is reduced and the decay into \tilde{t}_1 contributes significantly (14%).
- 96% of $\tilde{\chi}_1^\pm$ decay into a stau and a tau-neutrino, the others yield an LSP and a W -boson.
- All of $\tilde{\chi}_2^0$ decay into a lepton and \tilde{l}_R , with a $\tilde{\tau}$ -fraction of about 85%.
- Right-handed sleptons have the exclusive decay into LSP and the corresponding lepton.

Hence, when looking for a cascade with sufficient length it is clear that the starting point must be a left-handed squark (first or second generation) or a \tilde{b}_1 , optionally coming from a gluino decay. As 20% of all events have a gluino and left-handed squark as primary

sparticles and only 8% such a squark pair, this option is worth a consideration and will give an additional jet in the final state.

For squark decays the chargino channel has the largest branching ratio. However, the chargino decays either via $\tilde{\tau} + \nu_\tau$, yielding an additional unmeasured particle, or via a W-boson, which has a dominantly hadronic decay and increases the number of jets in the final state. A leptonic W-boson decay yields a neutrino, which again means an additional unmeasured particle and makes it almost impossible to achieve an over-determined event topology.

Having the second lightest neutralino as next particle limits the number of jets to 1 per branch (plus the gluino jet). The disadvantage is the large abundance of stau-leptons in the $\tilde{\chi}_2^0$ -decay, which decay to tau leptons, whose reconstruction and identification is especially difficult. Limiting the signature to electrons and muons, which are simpler to reconstruct in the detector, the complete decay chain will look as shown in Fig. 5.2. The total branching ratio for the cascade starting with a \tilde{q}_L is 1.7×10^{-3} at the SPS1a. The same cascade was

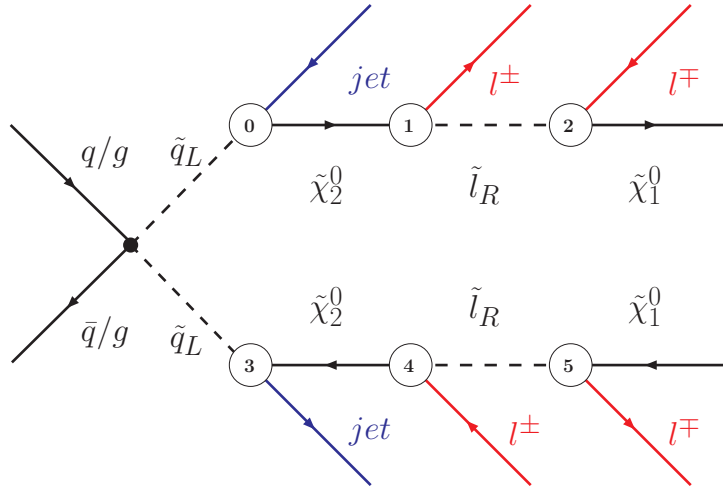


Figure 5.2.: Feynman graph for event topology with 4 leptons at the SPS1a parameter point.

also used in other mass determination studies [74,75].

While the largest fraction of events with such a topology contains a \tilde{q}_L as starting point, any of the other, lighter squarks (except \tilde{t}) can initiate the same cascade. Therefore we include all possible squark types in our signal definition and consider them individually in the analysis, if necessary. Masses of the particles appearing in the signal cascade are listed in Tab. 5.2.

All branching ratios depend on the particular SUSY parameters and therefore other points in the parameter space may yield more or less favorable leptonic decay chains.

Particle	\tilde{g}	\tilde{d}_L/\tilde{s}_L	\tilde{u}_L/\tilde{c}_L	\tilde{q}_R	\tilde{b}_2	\tilde{b}_1	$\tilde{\chi}_2^0$	\tilde{l}_R	$\tilde{\chi}_1^0$
Mass [GeV]	606	568	562	546	546	517	180	143	97

Table 5.2.: Pole masses of signal cascade particles in the SPS1a simulated events sample (cf. Sec. 5.2).

Backgrounds

The majority of background events have the same topology but contain a stau slepton instead of smuon or selectron. The stau channel has a four times higher branching ratio and $\sim 35\%$ of the taus decay leptonically [16]. Other sources of four lepton events are decays of Z - and W -bosons in the chain, but their fraction is small.

Concerning the Standard Model backgrounds, there are few processes with a signature of four isolated leptons which form to pairs of opposite sign and same flavor. A further requirement of hard jets and on missing transverse energy in the event will make their contribution negligible [83,84].

Combinatorics

The number of possible permutations of jets and leptons in this topology is rather small. We first consider the case of squark pair production, i.e. two jets and two lepton pairs in the final state. Not taking into account the exchange of the two LSPs, which are not measured anyway, the following permutations remain:

- Exchange of jets between branches \rightarrow factor of 2
- Exchanging lepton positions on the same branch \rightarrow 2 possibilities for each branch
- If the lepton pairs have identical flavor \rightarrow 2 possibilities to combine them.

Note that if the LSPs are ignored the exchange of lepton pairs between branches is the same as exchanging the jets. This yields a total of $2 \times 2 \times 2 = 8$ permutations for different flavor lepton pairs or $8 \times 2 = 16$ otherwise.

The number of permutations grows if the event selection allows more jets in the final state. Only two of the jets have to be placed in the cascade and hence for N jets the factor of 2 for the permutation is replaced with a factor $N \cdot (N - 1)$.

5.2 Simulated Events Sample

For the generation of a SPS1a Monte Carlo event sample the SUSY-HIT program package was used [85], which includes codes for the calculation of the SUSY mass spectrum (SUSPECT) and the decays of the supersymmetric and higgs particles (SDECAY, HDECAY).

From the mSUGRA and Standard Model parameters (cf. Tab. 5.1 and Tab. 5.3) all weak-scale quantities are calculated.

$\alpha_{em}^{-1}(M_Z)$	G_F [GeV ⁻²]	$\alpha_S(M_Z)$	M_Z [GeV]	m_b [GeV]	m_t [GeV]	m_τ [GeV]
127.934	1.16639×10^{-5}	0.1172	91.187	4.25	172.5	1.7771

Table 5.3.: Values of Standard Model input parameters for Monte Carlo event generation.

In the CMS simulation framework the outcome was passed to Pythia for the actual event generation and the simulation of sparticle decays and the fragmentation and hadronization processes.

The obtained leading-order cross-section for a center-of-mass energy of 14 TeV is 36 pb. An event sample of 5 million events was produced and processed with the CMS fast detector simulation (cf. Sec. 3.3.5), corresponding to an integrated luminosity of $L_{\text{int}} = 140 \text{ fb}^{-1}$.

5.2.1 Detector Simulation Objects

Since the CMS reconstruction software provides many options in the definition of jet, electron and muon objects, the relevant technical information is summarized in Tab. 5.4.

Jets: Anti-kt ($R = 0.5$) particle-flow jets are chosen and L2 and L3 energy scale corrections (cf. Sec. 3.3.1) are applied.

Missing Transverse Energy: The particle-flow missing E_T calculated from all reconstructed particles is used and is corrected for the jet energy scale (L2, L3 correction).

Electrons: Starting from the standard electron collection rather loose identification criteria (cf. Tab. 5.4, Sec. 3.3.3, [47]) must be fulfilled. An isolation value is calculated from energy deposits in the ECAL, HCAL and Tracker in a cone around the electron. The isolation value I is then given by the total energy deposits for the three detector components, divided by the electron p_T . The requested isolation is

$$I = \frac{\text{iso}^{\text{ECAL}} + \text{iso}^{\text{HCAL}} + \text{iso}^{\text{TRK}}}{p_T^{\text{electron}}} < 0.1 \quad (5.1)$$

The lepton isolation performance is discussed below.

Muons: The general muon collection is used and no further quality requirements are applied. The isolation is calculated from the energy deposits E_T in ECAL and HCAL and the tracker p_T in a cone of $R = 0.3$ around the muons. The three components are combined to an isolation value relative to the muon p_T in the same way as for electrons and an isolation $I < 0.2$ is required.

Jet Collection	ak5PFJetsL2L3
Missing E_T	metJESCorAK5PFJet
Electron Collection	gsfElectrons
Electron ID	eidRobustLoose
Isolation Value Maps	eleIsoFromDepsEcalFromHitsByCrystal eleIsoFromDepsTk eleIsoFromDepsHcalFromTowers
Muon Collection	muons
Muon Isolation Function	isolationR03()

Table 5.4.: Technical names of physics objects collections, identification and isolation procedures as used in the analysis. The CMS software release is CMSSW_3_8_7.

Particle Matching

In several occasions an association of reconstructed to generated particles is useful. Whether generated or reconstructed particles serve as starting collection for the comparison depends on the use case. In the determination of measurement resolutions a matching of generated objects to reconstructed ones is performed, whereas it is done the other way round when trying to identify the generator particles corresponding to a reconstructed signal cascade.

The procedure is equivalent in either case: for any particle the corresponding reconstructed or generated object closest in ΔR is matched, if $\Delta R < \Delta R_{max}$ as well as $0.5 < p_T^{rec}/p_T^{gen} < 2$. is fulfilled. The maximum distance is chosen as $\Delta R_{max} = 0.1$ (0.3) for leptons (jets). A particle is only matched to a single particle from the other collection. In case of ambiguities the object closest in ΔR is chosen.

Lepton Isolation

The distribution of the isolation variable defined in Eq. 5.1 for electrons and muons in the SPS1a sample is shown in Fig. 5.3. Reconstructed electrons and muons with a matching generator particle peak at zero in a steeply falling distribution, while unmatched leptons tend to higher values of the isolation variable. For a matching the generated lepton must lie within $\Delta R = 0.1$ of the reconstructed particle.

The *fake rate*, defined as the fraction of unmatched leptons

$$\frac{\#notmatched}{\#matched + \#not\ matched} \quad (5.2)$$

and the *efficiency*

$$\frac{\#matched}{\#generated} \quad (5.3)$$

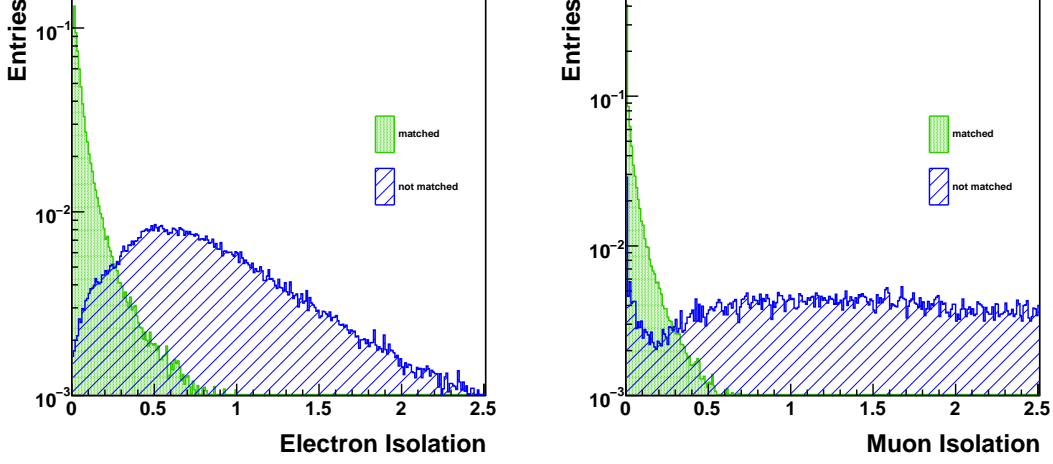


Figure 5.3.: Distribution of isolation variable Eq. 5.1 for electrons (left) and muons(right). Shown are the distributions for reconstructed leptons with a matching generator particle (green) and those without (blue) for SPS1a.

characterize the isolation cut. The efficiency includes the matching efficiency and only generated electrons and muons with $p_T > 10 \text{ GeV}$ and $|\eta| < 2.5$ are counted to respect the limited detector acceptance in lepton reconstruction.

Choosing the working point is a trade-off between high efficiency and low fake rate. In our case the suppression of background cascades seems to be most important, thus requiring a low fake rate. Hence, $I < 0.1$ is chosen for electrons, translating into an efficiency of 56% and a 5% fake rate (cf.Fig. 5.4) and for muons $I < 0.2$ is required, yielding 77% efficiency and a fake rate of 3%.

Resolutions

Resolutions for the transverse momentum and angular reconstruction of the different kinds of particles need to be known for the kinematic fit, where the entire covariance matrix for all measured parameters, i.e. four-momentum components, is needed (cf. Sec. 6.1).

Jet resolutions strongly depend on the transverse momentum and further vary with pseudorapidity. Therefore the jet response is typically determined in bins of these two variables. The jet transverse momentum resolution parametrization is

$$\frac{\sigma(p_T/p_T^{\text{gen}})}{\langle p_T/p_T^{\text{gen}} \rangle} (p_T^{\text{gen}}) = \sqrt{\text{sgn}(N) \cdot \left(\frac{N}{p_T^{\text{gen}}} \right)^2 + S^2 \cdot (p_T^{\text{gen}})^{M-1} + C^2}, \quad (5.4)$$

as already introduced in Eq. 3.4 (Sec. 3.3.1). The parameters determined for the transverse

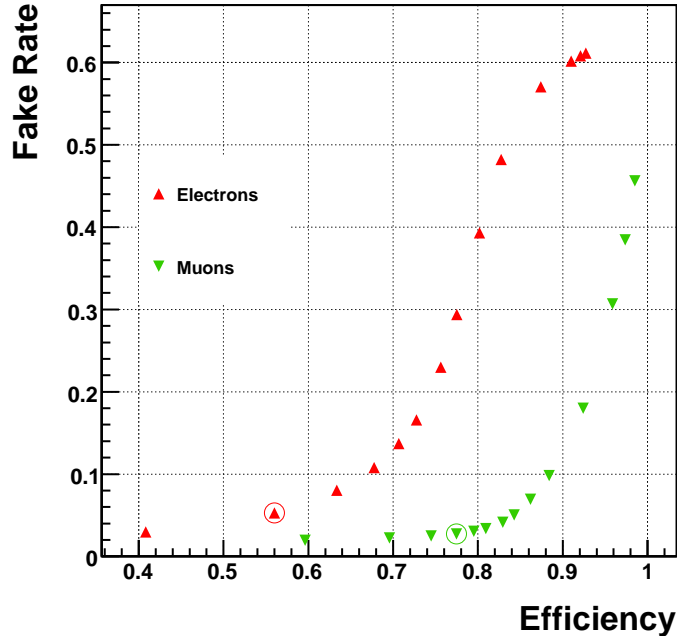


Figure 5.4.: Selection efficiency (Eq. 5.3) versus fake rate (Eq. 5.2) for different cuts on the isolation variable for electrons (red) and muons (green) for SPS1a. The working points are marked with circles.

momentum of the chosen particle-flow anti-kt ($R = 0.5$) jets are given in Tab. 3.1 [40].

However, we also need resolutions for the pseudorapidity and azimuthal angle measurement. They are determined on the SPS1a sample again using a binning in p_T and η , by matching reconstructed jets to *generator jets*, which are clustered from generated particles after the particle shower simulation.

The position resolution is characterized by the distribution of the differences $\eta^{rec} - \eta^{gen}$ and $\phi^{rec} - \phi^{gen}$ of reconstructed jets compared to a matched generator jet. For each p_T - η -bin a Gaussian is fitted to the observed distribution. The width of the Gaussian in a pseudorapidity region changes with p_T and is fitted with the resolution function Eq. 5.4. Fig. 5.5 shows the fitted resolution functions for three different pseudorapidity bins, up to $|\eta| = 3.0$ which marks the end of the HCAL endcap and the begin of the forward calorimeters (cf. Sec. 3.2.5). Parameters determined in the fits are summarized in Tab. 5.5 and used to calculate the uncertainties for the covariance matrix in the kinematic fit.

Electron and muon resolutions are also determined in bins of p_T and η . Using the SPS1a sample all generator electrons and muons from a χ_2^0 or $\tilde{e}_R/\tilde{\mu}_R$ decay are compared to a matching reconstructed electron or muon. The cores of the observed distributions of

Variable	η			ϕ		
	N	S	M	N	S	M
$ \eta $ -Range						
0.0 – 1.0	1.2×10^{-11}	-0.39	-0.46	6.0×10^{-17}	-0.40	-0.44
1.0 – 2.0	1.6×10^{-7}	-0.43	-0.44	1.8×10^{-8}	-0.41	-0.39
2.0 – 3.0	3.0×10^{-8}	-0.49	-0.45	3.0×10^{-10}	-0.39	-0.36

Table 5.5.: Fitted jet angular resolution parameters (cf. Fig. 5.5)

p_T^{rec}/p_T^{gen} , $\eta^{rec} - \eta^{gen}$ and $\phi^{rec} - \phi^{gen}$ are again fitted with a Gaussian and the gaussian width is plotted versus the transverse momentum. (Figs. 5.6-5.8).

The fitted functional form for the electron p_T is the one expected for a calorimeter based measurement

$$\sigma(p_T^{rec}/p_T^{gen}) = \sqrt{\left(\frac{a}{p_T}\right)^2 + \left(\frac{b}{\sqrt{p_T}}\right)^2 + c^2}, \quad (5.5)$$

and similar to the jet case consists of a noise term (a), a stochastic term (b) and a constant term (c). Also the electron and muon η and ϕ resolution show the same behavior.

For the muon p_T the deviation from the true momentum increases with p_T , which is an effect of the detector hit resolution in the inner tracker. The published muon resolution plot Fig. 3.9 shows that at high momenta the combination of tracker and muon system information attenuates the increase, but not sufficient high p_T muons are available in the SPS1a sample to observe this effect. Therefore, data is only fitted with a second order polynomial $p_0 + p_1 \cdot p_T + p_2 \cdot p_T^2$ and the observed resolution is consistent with the published plot in this p_T -region.

The resulting parameters for the electron (muon) resolution are given in Tab. 5.6 (5.7) and in most cases the uncertainties on the fitted parameters are large, due to their large correlations. Overall, we find that the angular resolution for both, electrons and muons, is of the order of 10^{-4} and the transverse momentum is measured to a few percent precision, which is much better than for jets. Hence, any uncertainties on the fitted parameters are of little importance, since the fit will mainly adapt the jet momenta.

Parameter	$ \eta $ -Range	$0.0 < \eta < 0.8$	$0.8 < \eta < 1.5$	$1.5 < \eta < 2.5$
p_T	a	0.0565	0.0909	2.5×10^{-8}
	b	0.0765	0.1256	0.104
	c	0.0045	5.4×10^{-13}	0.0105
η	a	4.6×10^{-10}	1.2×10^{-10}	2×10^{-11}
	b	0.00132	0.00123	0.00158
	c	0.000323	0.000255	0.000135
ϕ	a	9×10^{-14}	8.2×10^{-10}	1.7×10^{-11}
	b	0.0019	0.00257	0.00475
	c	0.000104	0.000206	1.2×10^{-13}

Table 5.6.: Fitted electron resolution parameters (cf. Fig. 5.6).

Parameter	$ \eta $ -Range	$0.0 < \eta < 0.8$	$0.8 < \eta < 1.5$	$1.5 < \eta < 2.5$
p_T	p_0	0.00872	0.01425	0.01718
	p_1	3.5×10^{-5}	$5. \times 10^{-5}$	$2. \times 10^{-5}$
	p_2	1.1×10^{-7}	7.4×10^{-8}	6.5×10^{-7}
η	a	$2. \times 10^{-10}$	0.00391	0.00307
	b	0.00103	$1. \times 10^{-14}$	0.00092
	c	0.000283	0.000222	0.00013
ϕ	a	0.00271	0.0039	0.00564
	b	0.000454	0.000512	0.000439
	c	5.4×10^{-5}	6.9×10^{-5}	9.6×10^{-5}

Table 5.7.: Fitted muon resolution parameters (cf. Fig. 5.7).

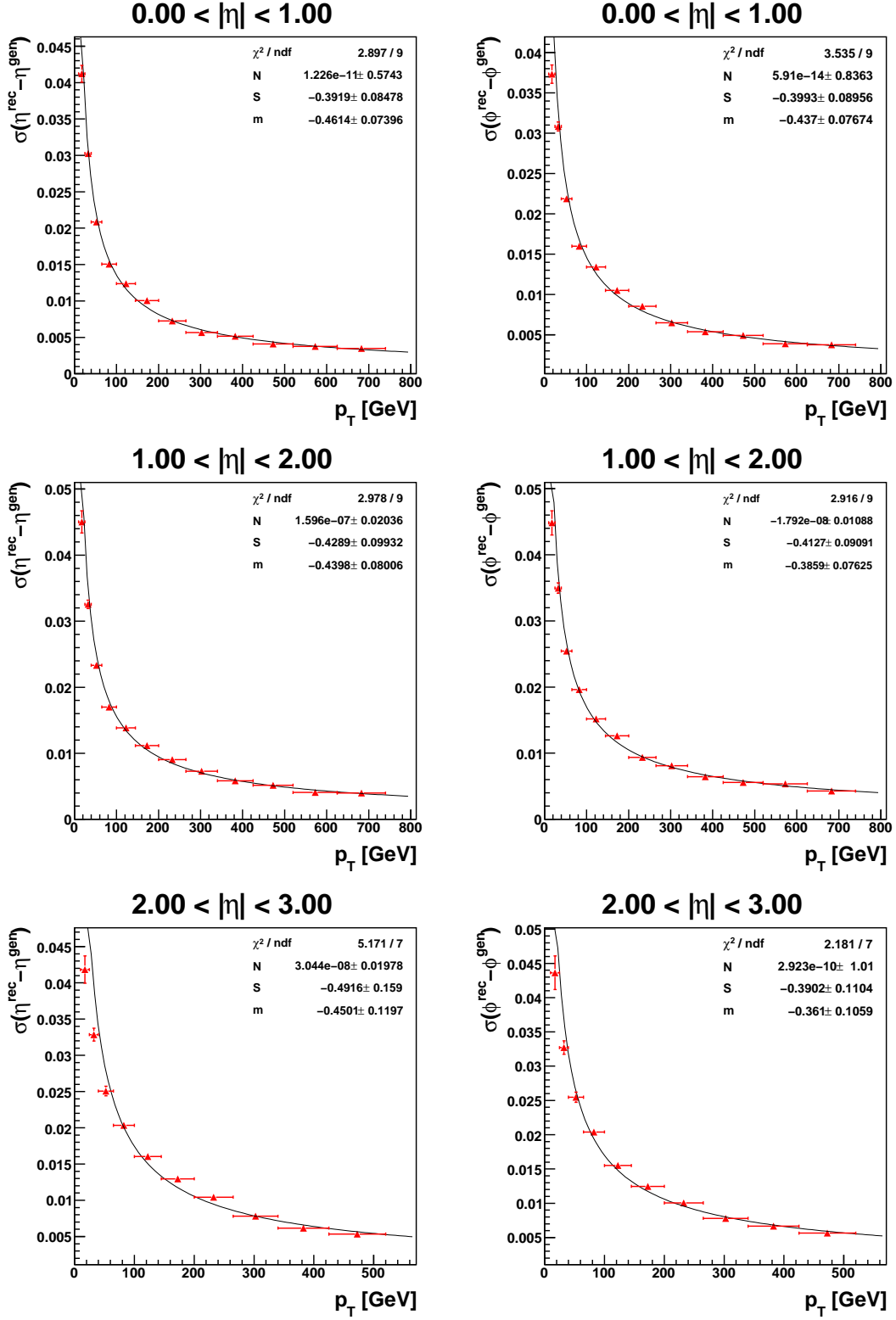


Figure 5.5.: Standard deviation of angular reconstruction residuals for jets in different pseudorapidity bins. Left column: η -resolution versus the generated jet p_T . Right column: ϕ -resolution. The resolution function Eq. 5.4 with parameters N , S and M is fitted to data, while C is fixed at zero.

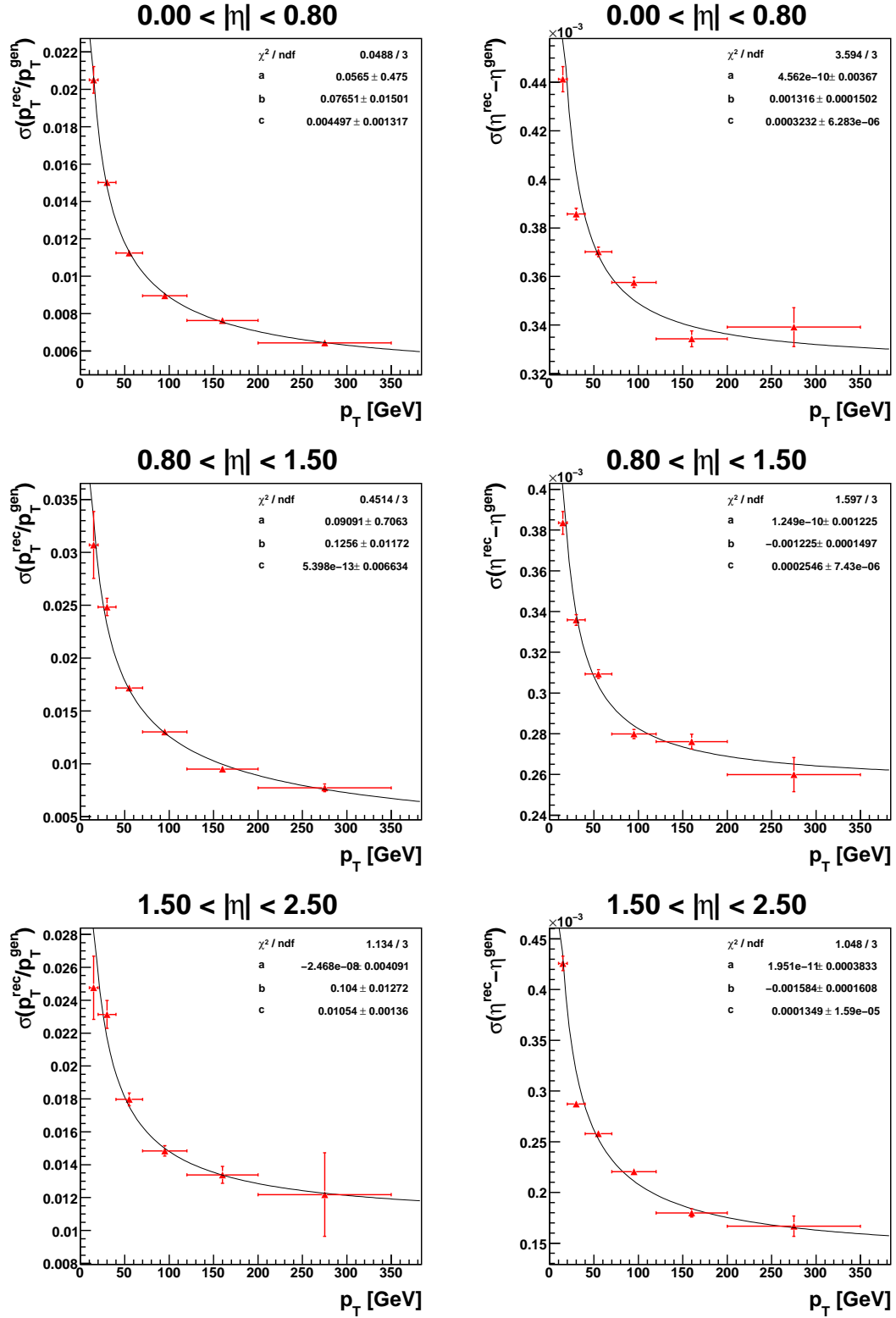


Figure 5.6.: Electron transverse momentum resolution (left column) and pseudorapidity resolution (right column) versus p_T for different pseudorapidity regions.

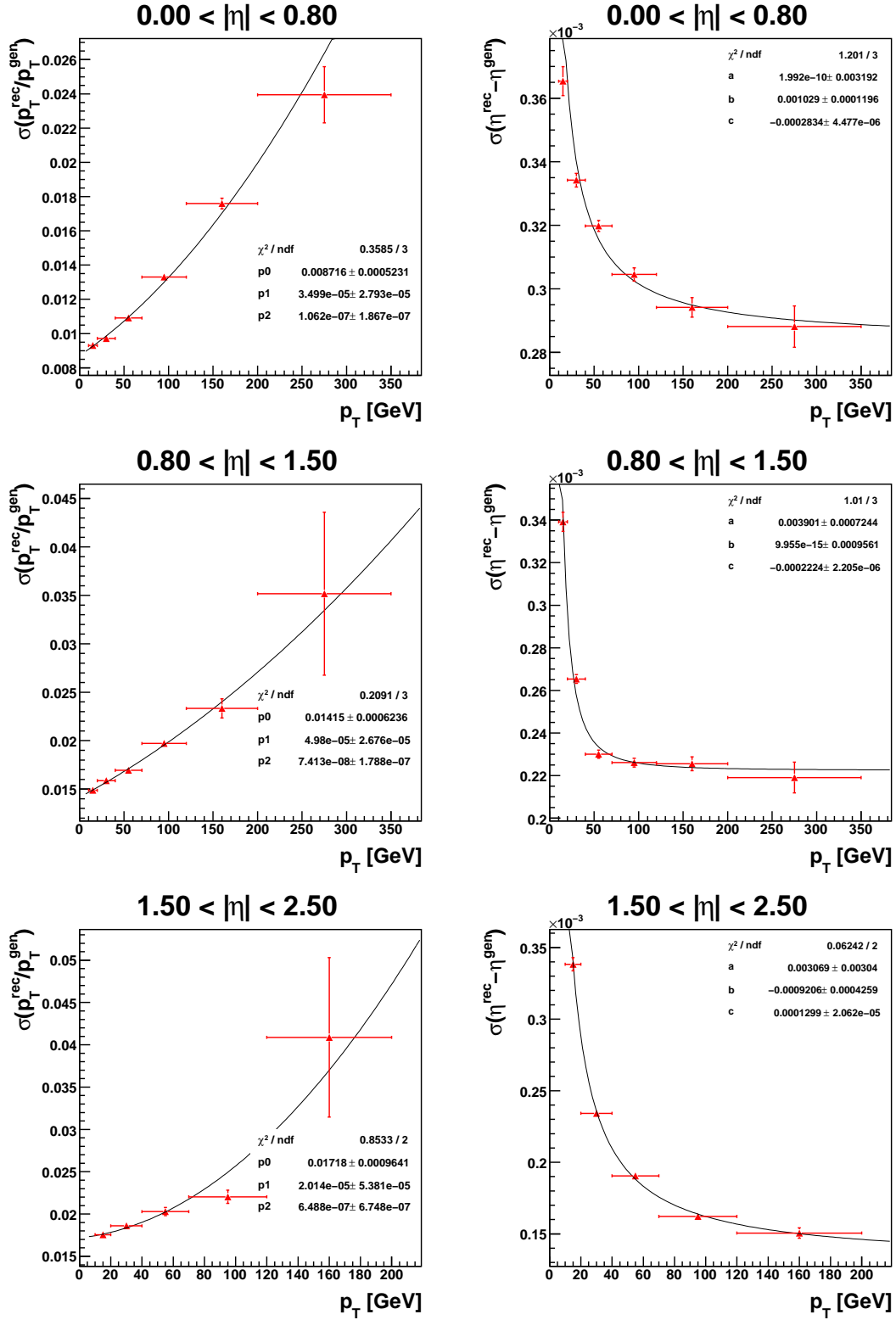


Figure 5.7.: Muon transverse momentum resolution (left column) and pseudorapidity resolution (right column) versus p_T for different pseudorapidity regions.

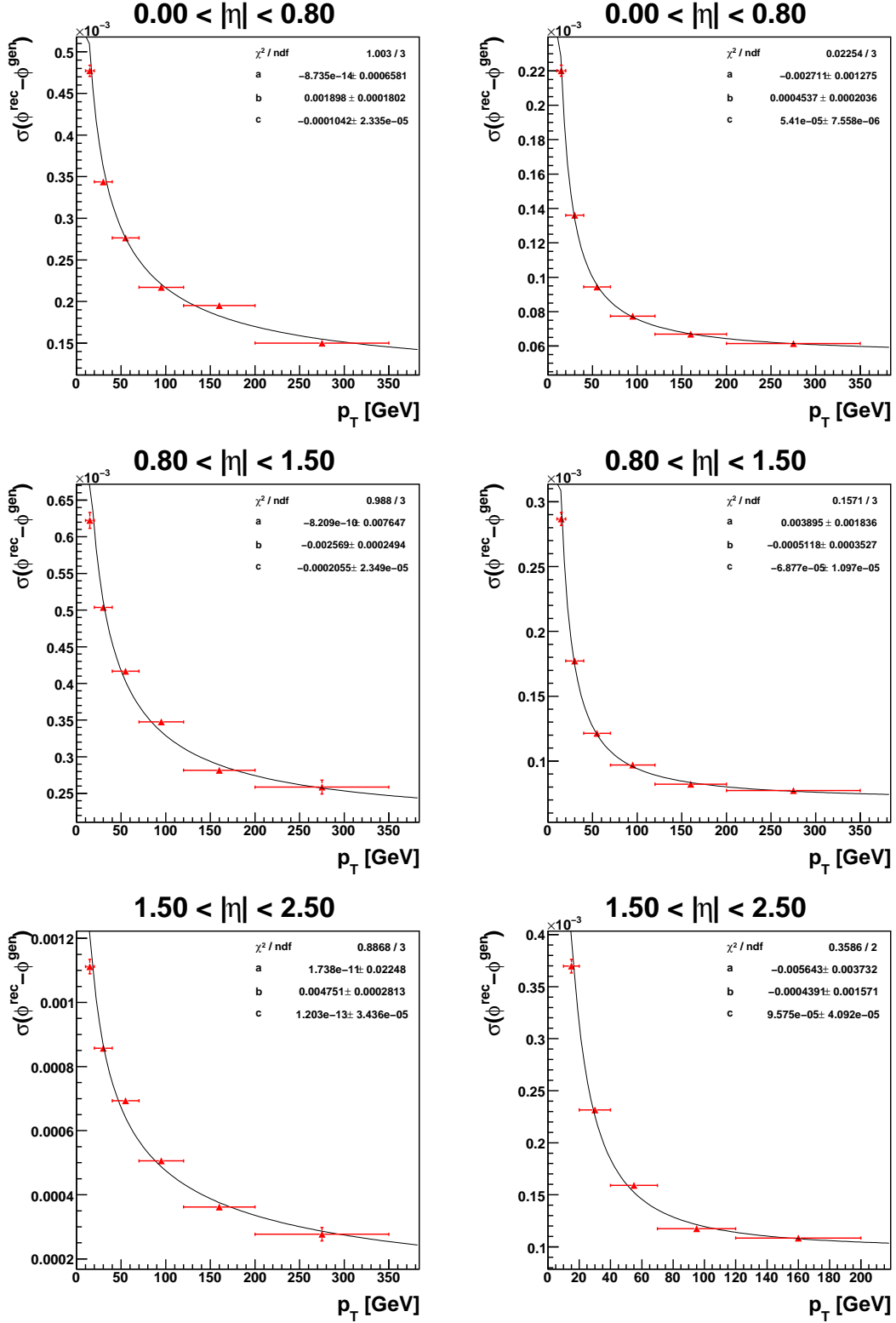


Figure 5.8.: Electron (left column) and muon (right column) azimuthal angle resolution versus p_T for different pseudorapidity regions.

5.2.2 Event Selection

Preselection

A preselection was applied in order to reduce the storage space of the simulated events sample. It is motivated by the final event selection for the leptonic cascade and applies the following cuts on reconstructed objects (cf. Sec. 5.2.1).

- Jets: $N \geq 2$ with $p_T > 20 \text{ GeV}$ and $|\eta| < 5$.
- Leptons (electrons+muons): $N \geq 3$ with $p_T > 5 \text{ GeV}$, $|\eta| < 2.5$, counting only electrons which fall either in the identification class *eidRobustLoose* (cf. Sec. 3.3.3) or fulfill some basic isolation requirements.

Without the requirement on electron identification more than 75% of the events have at least two leptons and pass the preselection. The number of remaining events including the identification cuts is 2,470,405, i.e. 49% of the initial sample.

Spectra of the transverse momenta for the four leptons and two jets with highest p_T (*leading* objects) in an event, as well as the missing E_T distribution after preselection are shown in Figs. 5.9 and 5.10 for signal and background events.

Final Selection

Starting from the preselected sample, several cuts are applied (Tab. 5.8) to select the signal cascade (Fig. 5.2).

The most distinctive feature of this cascade are the two lepton pairs, each consisting of opposite charge and same flavor leptons (OSSF). Events containing exactly four such isolated leptons are chosen, considering only electrons and muons. Not allowing additional leptons in the event reduces the background and keeps combinatorics small. A minimal transverse momentum of 10 GeV is required to ensure a sufficient reconstruction quality. In the CMS detector leptons are only identified in the pseudorapidity region $|\eta| < 2.5$, i.e. the region covered by the silicon tracker and muon chambers (cf. Figs. 3.3, 3.6).

The second feature are two jets, which are expected to have high energy due to the large mass difference between squark and neutralino. Additional jets may also come from a gluino decay or hadronic activity like initial and final state radiation. Two jets with a transverse momentum of at least 30 GeV are found in all of the selected leptonic events.

The p_T spectra of the jets with highest and second highest p_T (Fig. 5.11) show, that on average signal events have higher transverse jet momenta than other SUSY processes with e.g. squark decays into heavier charginos or neutralinos. In order to suppress background, a requirement of $p_T > 150 \text{ GeV}$ is chosen. In addition we restrict the jet to lie within $|\eta| < 3.0$, where the angular resolution could be determined well (cf. Sec. 5.2.1).

Since more jets may emerge from initial and final state radiation, only the minimal number of jets is specified, with the drawback of increased combinatorics. Some missing

	Preselected Sample	Event Selection Cuts		
		2 OSSF lepton pairs (e/μ) $p_T > 10 \text{ GeV}$ $ \eta < 2.5$	≥ 2 Jets $p_T > 150 \text{ GeV}$ $ \eta < 3.0$	missing E_T $> 50 \text{ GeV}$
$\tilde{q}_L \tilde{q}_L$	579	162	120	117
$\tilde{g} \rightarrow \tilde{q}_L$	455	97	71	65
\tilde{b}_1	720	183	136	126
\tilde{b}_2, \tilde{q}_R	214	44	31	26
Total Signal	1968	486	358	334
Eff. Signal	1	0.25	0.18	0.17
Background	2470405	923	391	367
S/B	0.0008	0.53	0.92	0.91

Table 5.8.: Cumulative effect of event selection cuts on detector simulation sample corresponding to an integrated luminosity of $L_{int} = 140 \text{ fb}^{-1}$. The signal efficiency includes all three signal categories (see below). Backgrounds include all other SUSY processes.

transverse energy is expected from the escaping LSPs and helps to reduce Standard Model backgrounds, but does not contribute to the suppression of SUSY background.

Figures 5.12 and 5.13 show kinematic distributions of all objects after the final selection.

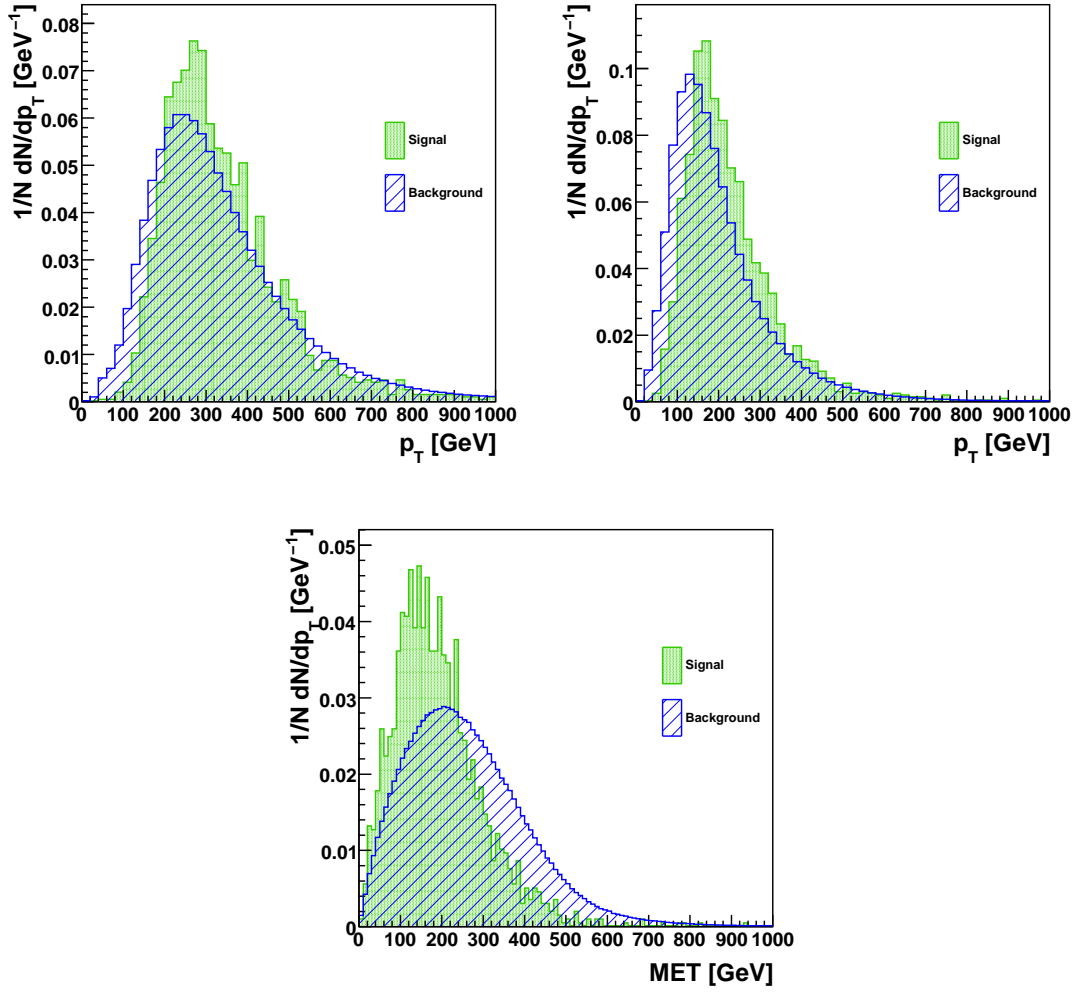


Figure 5.9.: Transverse momentum spectra of the two leading jet (left), next-to-leading jet (right), and missing E_T in signal and background events at SPS1a after preselection.

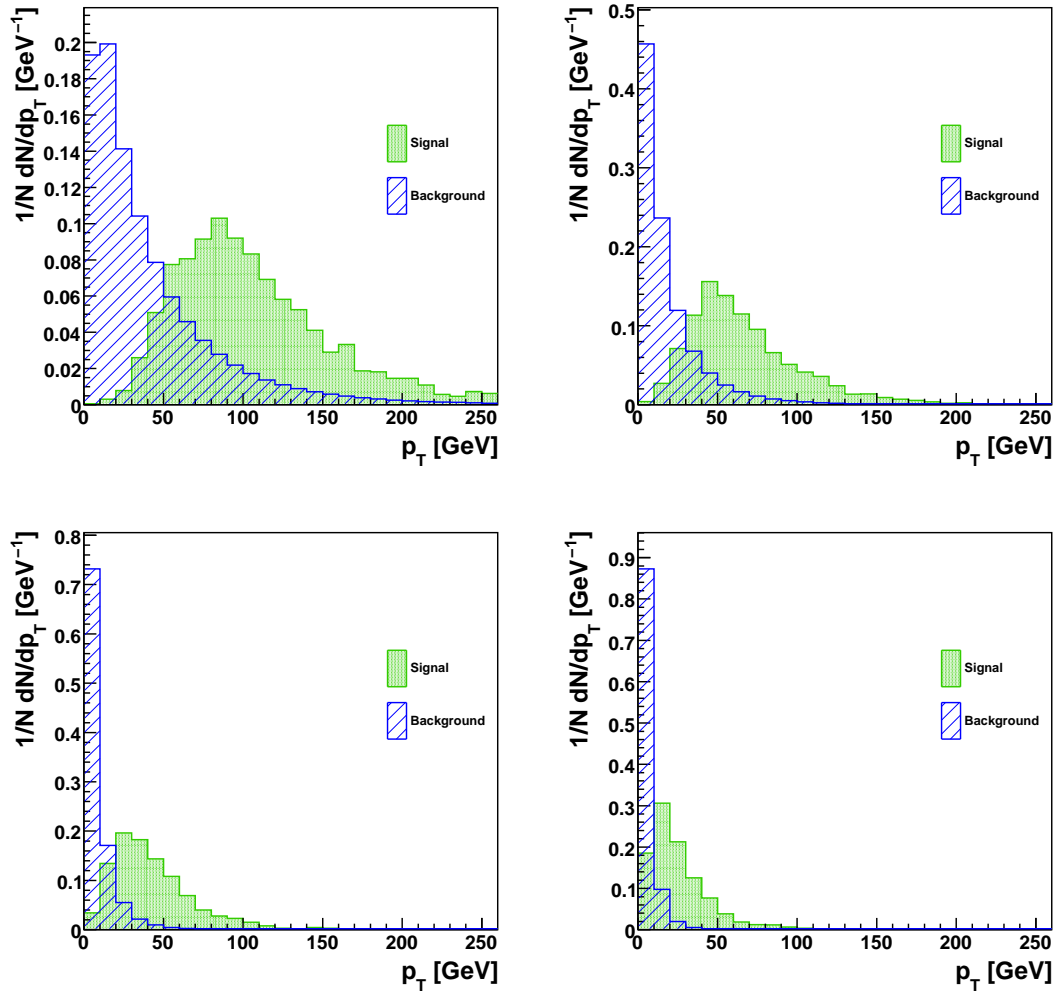


Figure 5.10.: Transverse momentum spectra of the four leading leptons in signal and background events at SPS1a after preselection.

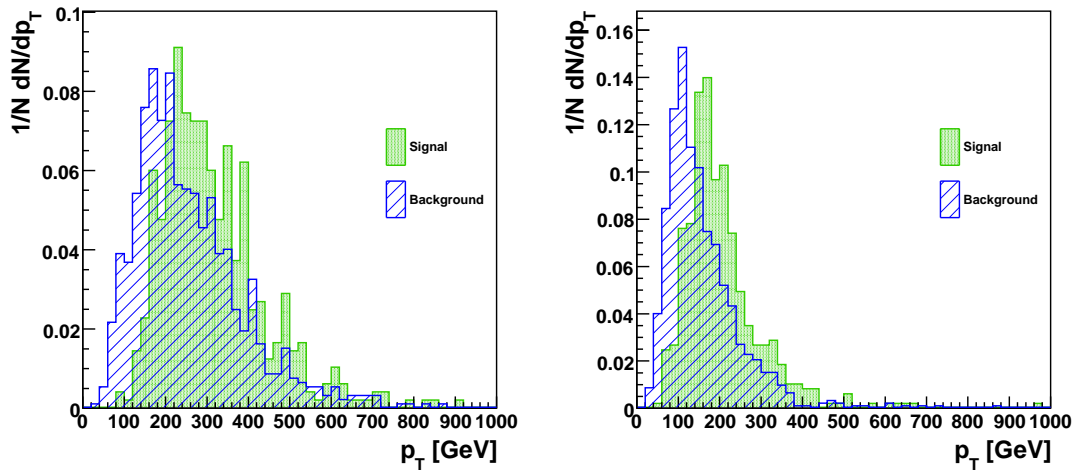


Figure 5.11.: Transverse momenta of leading and second leading jet in signal (green) and background events (blue) in events with 4 isolated OSSF lepton pairs.

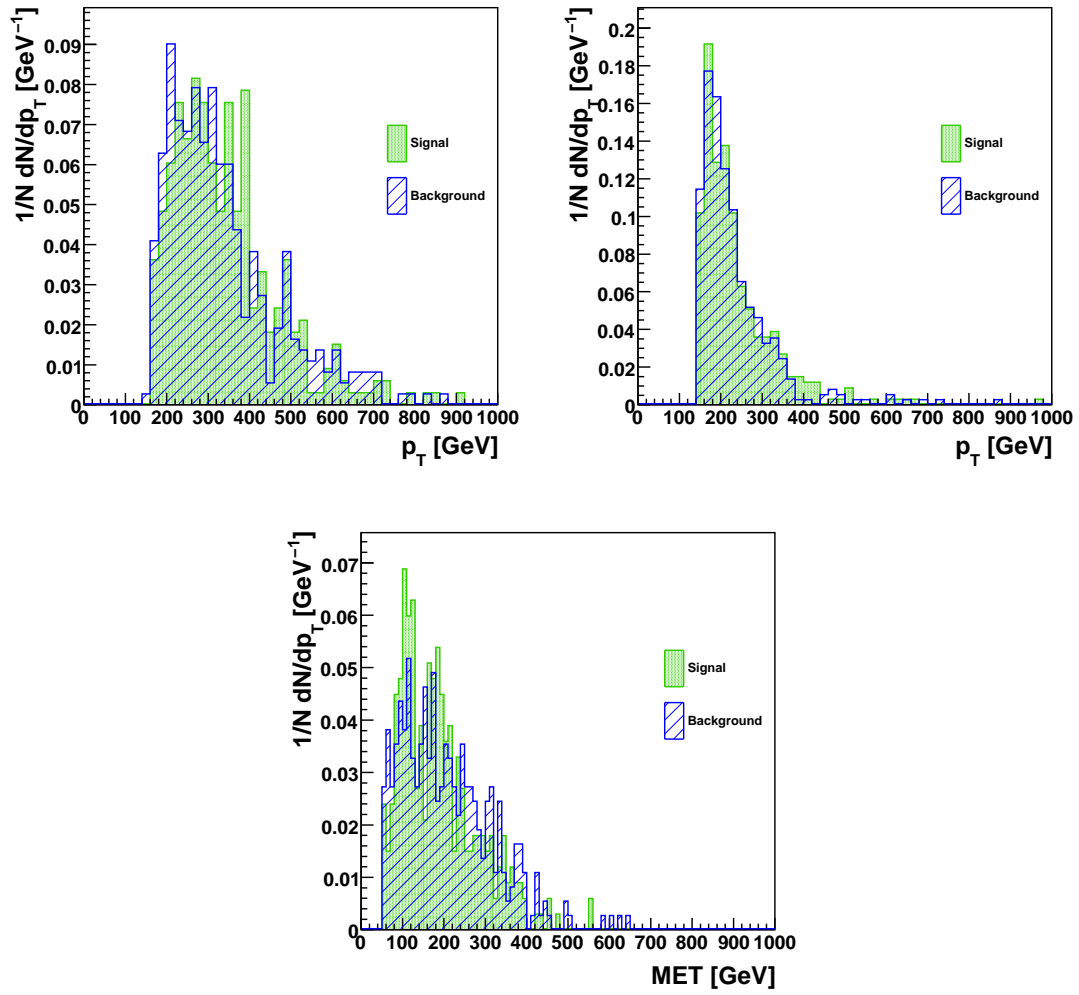


Figure 5.12.: Transverse momentum spectra of the two leading jets and missing E_T in signal and background events at SPS1a after full selection.

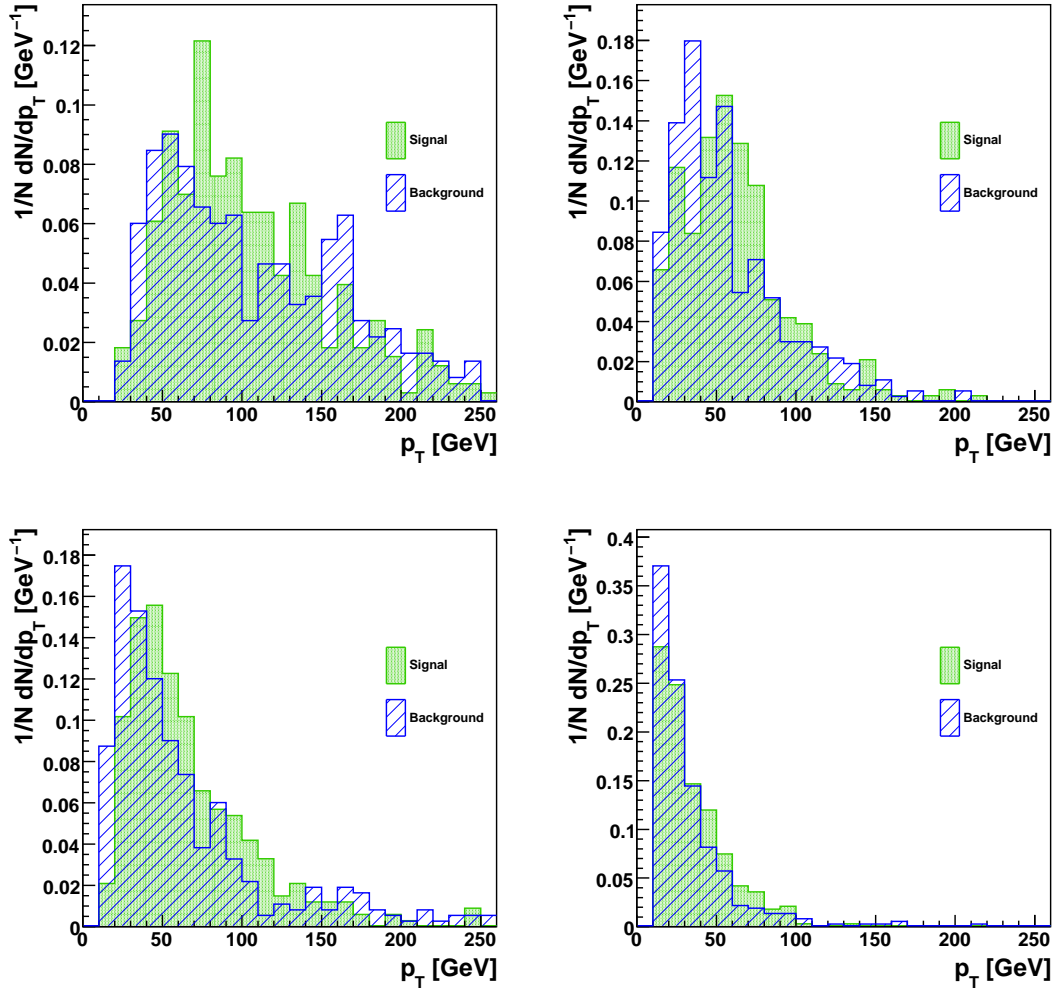


Figure 5.13.: Transverse momentum spectra of the four leading leptons in signal and background events at SPS1a after full selection.

The event selection cuts are similar to those applied in the mass determination study by McElrath et al. [74] but not identical. These authors require a lower jet $p_T > 100$ GeV and an additional cut on jet pseudorapidity, motivated by the fact that jets from heavy particle decays are found dominantly in the central detector region. However, we find that a restriction to $|\eta| < 2.5$ does not significantly change the selection result. Furthermore a b -jet veto is included in their study. In principle the obtained event samples should be comparable in terms of selected phase space.

Starting from the preselected sample, 334 signal events are selected (Tab. 5.8), which can be divided into four groups, using Monte Carlo truth information.

1. $\tilde{q}_L \tilde{q}_L$: Squark pair production (1st and 2nd generation) and the decay via the desired SUSY particles.
2. $\tilde{g} \rightarrow \tilde{q}_L$: Gluino or gluino-pair production and their decay into left-handed squarks of the first and second generation plus the subsequent signal decay.
3. \tilde{b}_1 : Events containing at least one \tilde{b}_1 , either directly produced or coming from a gluino decay.
4. \tilde{b}_2, \tilde{q}_R : Appearance of at least one of the almost mass degenerate \tilde{b}_2 or right-handed squarks in the signal cascade.

Masses of the b -squarks and right-handed squarks differ from those of the first two generations of left-handed squarks (cf. Sec. 5.1) but nevertheless are included in the signal, since the final state is identical. More precisely, the jet flavor is different in case of \tilde{b} and in principle b -tagging could be exploited to distinguish the \tilde{b} -decay from other squarks.

Considering all three signal categories a selection efficiency of 17% is found. The SUSY background is strongly suppressed by a factor of 3×10^{-4} but still contributes 367 events, yielding a signal to background ratio of $S/B = 0.91$ for the selected sample. All possible SUSY decays were included in the initial event sample.

Including backgrounds a total of 701 out of the 2470405 events is selected, where the size of the event sample was already reduced in a preselection with 49% efficiency, giving a total fraction of selected events of $701/5,000,000 = 1.4 \times 10^{-4}$.

Background events are categorized in Tab. 5.9 according to their particle content. Each event is listed in the first category in which one of its branches matches, going from the first to the last row of the table. The (electroweak) production of neutralinos, charginos and sleptons contributes with 14%. In these events additional jets must be picked from initial state radiation. The pair production of \tilde{t}_2 hardly contributes ($\sim 4\%$) but the much lighter \tilde{t}_1 appears in one quarter of the events. It is light enough to be either produced directly or come from a gluino or sbottom decay. In the subsequent decay chain leptons then arise from a top-quark or chargino decay.

Category	Selected	Fraction
direct $\tilde{\chi}$ or \tilde{l} production	53	0.14
direct \tilde{t}_2 -pair production	16	0.04
\tilde{t}_1 from production or \tilde{g} or \tilde{b} decay	90	0.25
\tilde{g}/\tilde{q} decay via $\tilde{\chi}_{3/4}^0/\tilde{\chi}_{1/2}^\pm$	111	0.30
direct $\tilde{q} \rightarrow \tilde{\chi}_1^0$ decay	3	0.01
signal topology but decay via $\tilde{\tau}$	94	0.26
Total	367	1.0

Table 5.9.: Mutual exclusive categories of background events. Events are classified in the order listed here, if one of the two decay branches falls into this category.

A large fraction of the background (30%) contains leptonic decays of other neutralinos or charginos than the desired $\tilde{\chi}_2^0$. The last important background category is very *signal-like* and differs only in the slepton flavor, where a $\tilde{\tau}$ is found. These events makes up about one quarter of the background.

In a way most background events are *signal-like* because 65% percent contain one branch with the correct $\tilde{q} \rightarrow \tilde{\chi}_2^0 \rightarrow \tilde{l}_R \rightarrow \tilde{\chi}_1^0$ decay ($\tilde{l} = \tilde{e}, \tilde{\mu}$) and even 87% at least one branch with the correct lower part $\tilde{\chi}_2^0 \rightarrow \tilde{l}_R \rightarrow \tilde{\chi}_1^0$.

5.3 Toy Detector Simulation

A second event sample is used in the analysis, in order to test and demonstrate the performance of the mass determination method in a simplified scenario with reduced experimental uncertainties and imperfections. It is based on the same generated events but does not make use of the CMS detector simulation. Instead a pseudo detector simulation is applied to all partons and leptons from the Pythia final-state of the hard interaction, including initial- and final-state radiation but not the parton shower or hadronization.

In this *Toy Monte Carlo* (Toy MC) all quarks, gluons and leptons are smeared in p_T , η , and ϕ around their true value according to a gaussian distribution, where the width of the gaussian is given by the resolutions which were determined for the detector simulation in the previous section (cf. Tabs. 3.1, 5.5-5.7).

Tau leptons are treated according to their decay mode. For hadronic decays the tau fourvector is treated like a quark while in leptonic decays the resulting electron or muon is smeared.

This approach is of course a strong simplification of the real situation, where one has to deal with effects of hadronization, overlap in jet clustering, reconstruction inefficiencies, fake leptons and jets, additional jets from multiple interactions and underlying event. These difficulties are included in the study using the CMS detector simulation but ignored in this

	Signal	Background
Det. Sim. Selected Sample	334	367
≥ 2 Jets, $p_T > 150$ GeV, $ \eta < 3.5$ 2 OSSF e/μ Pairs, $p_T > 10$, $ \eta < 2.5$	252	171
≥ 2 Jets, $p_T > 100$ GeV, $ \eta < 3.5$ 2 OSSF e/μ Pairs, $p_T > 10$, $ \eta < 2.5$	312	238

Table 5.10.: Event selection in Toy MC. The initial sample consists only of events selected in the detector simulation sample.

Toy Monte Carlo.

Using the Toy Monte Carlo facilitates e.g. the validation and testing of the kinematic fit implementation and setup in a well-defined scenario where all measurement uncertainties are perfectly known. Furthermore, studying the combinatorial problem is simplified without the complication of matching measured final states to the generated ones. It will help to disentangle detector and measurement effects from those inherent in the mass determination method.

Toy Monte Carlo Event Selection

A Toy MC event selection with identical cuts as in the detector simulation case does not yield the same sample. Much more events fulfill the selection criteria (1050 instead of 749 in case of no missing E_T cut), mainly due to the perfect reconstruction efficiency for leptons and the idealized jet treatment.

However, for a later comparison of results the two samples should be comparable in the sense, that the event content is similar and the same kinematic phase space is covered. This is approximated by performing the Toy MC selection only on those events, which were selected in the detector simulation sample.

Requiring two OSSF lepton pairs and two jets with $p_T > 150$ GeV on Toy MC level, only 75% of signal and 47% of background events are selected. The main reason why events fail the selection is the cut on the jet transverse momentum.

The distribution of the second leading jet p_T in discarded signal events (Fig. 5.14) shows that many of these events have a second jet with transverse momentum close to the cut value. By lowering it to 100 GeV, 93% of signal events fulfill the requirements (cf. Tab. 5.10).

For background the discrepancy remains much larger since many events are also failing the lepton requirement and do not contain the correct number of leptons. Therefore the selected Toy MC sample has a better S/B -ratio of 1.31 and is of limited use in studies including background.

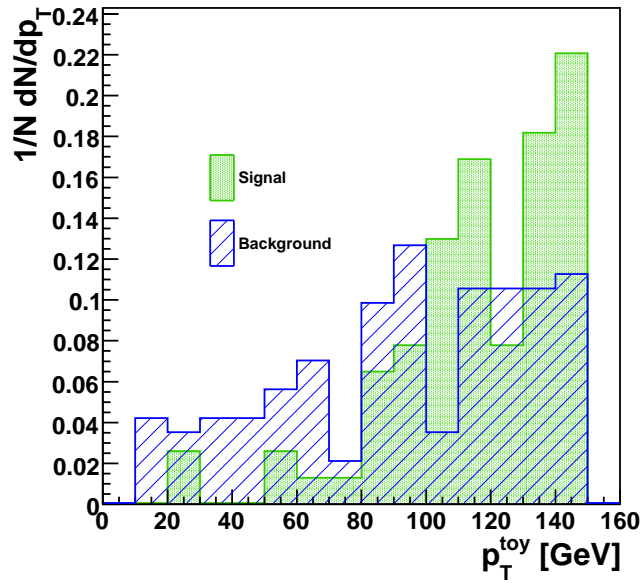


Figure 5.14.: Toy Monte Carlo transverse momenta of second leading jet in signal (green) and background events (blue) which were not selected with a $p_T > 150$ GeV cut.

Chapter 6

Kinematic Fit Implementation and Setup

6.1 Kinematic Fitting

The new approach for mass determination consists of an event-by-event kinematic fit in which hypotheses for the involved masses are tested. Kinematic fit means a least-square minimization of the residuals of all measured parameters in an event (p_T , η and ϕ of jets and leptons), which are subject to several kinematic constraints. In our case the constraints are invariant masses of combinations of final-state particles as well as an overall transverse momentum balance in the event. A solution to such a problem can be found using the method of Lagrangian multipliers.

6.1.1 Method of Lagrangian Multipliers

The squared sum of residuals for the n measured parameters (\vec{y}) with covariance matrix V

$$S(\vec{y}) = \Delta\vec{y}^T V^{-1} \Delta\vec{y} \quad (6.1)$$

has to be minimized, while fulfilling the kinematic constraints. Each of the l constraints is a function of the measured as well as the m unmeasured parameters (\vec{a}) and can be formulated as an equation

$$f_k = f_k(\vec{y}, \vec{a}) \stackrel{!}{=} 0, \quad k = 1, \dots, l$$

which holds for the true values of the involved parameters.

Finding the minimum of a function (S) while at the same time fulfilling constraint equations can in general be achieved by the method of Lagrangian multipliers. Each constraint is multiplied by an additional parameter λ (Lagrange Multiplier) and added to the sum of squares

$$L(\vec{y}, \vec{a}, \vec{\lambda}) = S(\vec{y}) + 2 \cdot \sum_{k=1}^l \lambda_k f_k(\vec{y}, \vec{a}).$$

The extremum of this new function L gives the desired solution for \vec{y} and \vec{a} . The factor of two is a convention.

The extremum can be found by differentiation of L with respect to all parameters, including the Lagrangian multipliers. This yields a system of equations which has to be solved. If the constraints are linear functions of the parameters an exact solution can be found e.g. by matrix inversion. However, as the mass constraint we want to apply are non-linear a linearization must be used and the problem be solved iteratively. This procedure is described in the literature [86] and summarized in Appendix A.

If the problem is over-constrained, values for the previously unknown parameters \vec{a} can be found by solving these equations. Over-constrained means that more constraints than unknowns are available. This is obvious, considering that each constraint depending on an unknown parameter leads to an equation involving this parameter, by differentiation with respect to the Lagrangian multiplier.

An over-constrained system has a number of degrees of freedom which is given by the difference between the number of constraints and unmeasured parameters

$$\text{ndf} = l - m.$$

In the case of a SUSY cascade, as described in the previous section, the number of parameters is high. From the 6 jets and leptons we count 18 measured momentum components while the two LSPs contribute 8 unmeasured parameters. It was discussed that a total of ten constraints can be applied, eight of them constraining invariant masses and two of them the transverse momentum balance. Thus the system has $10 - 8 = 2$ degrees of freedom. The obtained values for S at the extremum of L should therefore follow a χ^2 -distribution with two degrees of freedom.

Unfortunately, the constraints are highly non-linear and include, depending on the parametrization, squares, sine, cosine, and/or their hyperbolic versions (cf. Sec. 6.1.2 below). Therefore it is of great importance for the convergence of the algorithm to have initial values for the unmeasured parameter which are close to the true extremum. Otherwise the error caused by the linearization might become too large and prevent convergence or lead to a secondary extremum. The issue of a choice of initial values in our specific case is discussed in Sec. 6.2.

Convergence Criteria

Criteria need to be defined, when the iterative search for the extremum of the function L can be stopped. Ideally this should happen when all constraints are fulfilled and the minimal sum of the residual is reached, i.e. the algorithm has converged in the (global) minimum. In reality such a criterion is not easy to define. Two quantities are used to judge on the level of convergence. The absolute sum of all constraints has to fall below an upper

bound

$$\sum_{k=1}^l |f_k| < \varepsilon_F \quad (6.2)$$

and the change of S with respect to the previous iteration should be small

$$\Delta S < \varepsilon_S \quad (6.3)$$

Default threshold values were chosen as $\varepsilon_S = 10^{-4}$ and $\varepsilon_F = 0.1 \text{ GeV} \times l$, the latter depending on the number of constraints.

Requiring $\sum_{k=1}^l |f_k|$ to decrease in each iteration is a suitable handle to enforce convergence. If in an iteration the sum of constraints increases, then the step size is reduced by a factor of two until the requirement is fulfilled again or a maximum number of ten step size reductions is reached. In most events the convergence criteria are reached within a few (<10) iterations, where the requirement on ΔS is the limiting factor.

A program package for kinematic fits established in the CMS collaboration [87] was adapted and used to perform the fit. The code follows the procedure outlined above. A few details on the implementation are summarized in the following.

6.1.2 Momentum Parametrization

A common parametrization of particle four-momenta at collider experiments uses the transverse energy E_T (or transverse momentum p_T if masses are negligible w.r.t typical energies), the pseudorapidity η and the azimuthal angle ϕ , since these are closely related to the detector geometry. For a massless particle the fourvector becomes

$$p = \begin{pmatrix} E \\ \vec{p} \end{pmatrix} = \begin{pmatrix} E_T \cdot \cosh \eta \\ E_T \cdot \cos \phi \\ E_T \cdot \sin \phi \\ E_T \cdot \sinh \eta \end{pmatrix}. \quad (6.4)$$

For all measured particles, jets and leptons, in the fit this parametrization is chosen. The unmeasured LSPs are parametrized using the momentum components and a mass, which may be hypothetical.

$$q = \begin{pmatrix} \sqrt{m^2 + |\vec{q}|^2} \\ q_x \\ q_y \\ q_z \end{pmatrix}. \quad (6.5)$$

6.1.3 Implementation of constraints

An invariant mass constraints for measured particles with four-momenta p^i and unmeasured particles with four-momenta q^j , restricted to a mass M with width Γ_M reads

$$f = \sqrt{\left(\sum_i p^i + \sum_j q^j\right)^2} - \alpha \cdot M = 0. \quad (6.6)$$

Here a Gaussian mass width is accounted for with the additional fit parameter α . It has an initial value of $\alpha^{ini} = 1$ and its variance is set to $\sigma_\alpha^2 = \Gamma_M^2/M^2$, such that a variation of α in the fit by 1σ corresponds to a variation of the mass constraint of $(1 \pm \sigma) \cdot M = M \pm \Gamma_M$.

Also the momentum balance is not exactly fulfilled in a typical event. The actual p_T sum, including the soft and forward particles outside the cascade, fluctuates around zero. In the constraint calculation this fluctuation is accounted for with an additional term β . This new parameter has an initial value of $\beta^{ini} = 0$ and a variance corresponding to the width of the fluctuation distribution $\sigma_\beta^2 = \Delta p_{x/y}^2$. The implementation for a momentum balance constraints, including out of cascade momentum c from initial and final state radiation, reads

$$f_{x/y} = \sum_i p_{x/y}^i + \sum_j q_{x/y}^j - c_{x/y} - \beta = 0. \quad (6.7)$$

The choices for the particle and p_T -balance widths are discussed later (Sec. 6.3.2).

With the above particle parametrizations the (squared) invariant mass of $i = 1, \dots, n$ measured particles p^i and one unmeasured object q can be written as

$$M^2 = \left(\sum_{i=1}^n E_T^i \cosh \eta^i + \sqrt{q_x^2 + q_y^2 + q_z^2 + m^2}\right)^2 - \left(\sum_{i=1}^n E_T^i \cos \phi^i + q_x\right)^2 - \left(\sum_{i=1}^n E_T^i \sin \phi^i + q_y\right)^2 - \left(\sum_{i=1}^n E_T^i \sinh \eta^i + q_z\right)^2. \quad (6.8)$$

The components of the total transverse momentum in the fit are less complex and for two unmeasured particles q^j read

$$p_x = \sum_{i=1}^n p_T^i \cos \phi^i + \sum_{j=1}^2 q_x^j - c_x \quad (6.9)$$

$$p_y = \sum_{i=1}^n p_T^i \sin \phi^i + \sum_{j=1}^2 q_y^j - c_y. \quad (6.10)$$

Clearly these equations are non-linear in the parameters E_T, η, ϕ , hence their deviations do not yield a linear system of equations and make a linearization and iterative solution necessary (see App. A for details).

Alternative Fit Approach

An alternative approach for a kinematic fit is the formulation of the constraints as additional χ^2 -terms. The minimization of the extended χ^2 can then be realized with an arbitrary minimization algorithm such as simulated annealing or genetic algorithm.

The option of a genetic algorithm was studied in the context of mass determination in a hadronic decay chain [76]. A major strength lies in the simultaneous treatment of huge combinatorics in the minimization. Since combinatorics is not as a huge concern in the leptonic decay, we stick to the well established method of Lagrangian multipliers.

6.2 Choice of Initial Values for Unmeasured Parameters

The choice of initial values for the unmeasured parameters is a key issue for the performance of the kinematic fit in a high-dimensional and non-linear problem like the SUSY events at hand. If the initial LSP momenta are set to values far away from their truth, the error introduced by the linearization might become too large and the fit algorithm possibly does not find the global extremum or gets stuck in a local one. It is very likely that several local minima exist, regarding the fact that the χ^2 -contour lies in a 18-dimensional parameter space.

6.2.1 Options for Choice of Initial Values

Beside a completely random choice of initial values, different well-motivated possibilities exist and are discussed in the following. Two of them are analytic solutions for an approximated problem and the third one exploits the knowledge about two-body decays to generate random values in a clever way.

Analytic Solutions

Reconsidering the constraint equations Eq. 4.2-4.5 for the decay cascade and assuming that the SUSY mass values are known, possibilities exist to analytically calculate the momentum components of the LSPs from a subset of these constraints.

The ansatz of Webber [75] using a subset of six mass and two momentum balance constraints was already described in Sec. 4.2.1. The analytic solution for the LSP momentum components is an approximation for the true LSP momenta. Their exact values would only be obtained in the case of correct mass hypotheses, a perfect transverse momentum balance and vanishing measurement errors.

In order to construct the linear system of equation (Eq. 4.6 – 4.7) the relation $p_D^2 = M_D^2$ was used to substitute the quadratic terms. Note that this constraint is not respected in the solution and therefore all invariant masses ($M_A^2, M_B^2, M_C^2, M_D^2$) constructed from the calculated LSP momenta do not agree with the input masses, unless $p_D^2 = M_D^2$ really holds.

Starting from such a set of LSP momentum components, the kinematic fit will still have to adjust the parameters to perfectly fulfill the mass constraints.

A second possibility was proposed by Schleper [88]. The basic idea is again the construction of a set of equations which are linear in the unknown four-momentum. In contrast to Webber's calculation all four mass constraints are enforced and the constraint on transverse momentum balance is not included.

From the set of mass constraint equations 4.2 for one decay branch, the linear system is obtained in the known way, by substituting the invariant masses $p_i^2 = M_i^2$. This time the chain is taken in the opposite direction and the squark (p_A) is the fourvector to be solved for.

$$p_A \cdot p_{f_1} = \frac{1}{2}(M_A^2 - M_B^2 + M_{f_1}^2) \equiv R \quad (6.11)$$

$$p_A \cdot p_{f_2} = p_{f_1} \cdot p_{f_2} + \frac{1}{2}(M_B^2 - M_C^2 + M_{f_2}^2) \equiv S \quad (6.12)$$

$$p_A \cdot p_{f_3} = (p_{f_1} + p_{f_2}) \cdot p_{f_3} + \frac{1}{2}(M_C^2 - M_D^2 + M_{f_3}^2) \equiv T \quad (6.13)$$

The expressions R , S , T depend only on measured particles and the SUSY masses, but not on any of the SUSY particle momenta. Adding a fourth trivial equation for the energy component of the squark $p_A^0 = p_A^0$ one can write in matrix notation

$$\begin{pmatrix} 1 & 0 & 0 & 0 \\ p_{f_1}^0 & p_{f_1}^1 & p_{f_1}^2 & p_{f_1}^3 \\ p_{f_2}^0 & p_{f_2}^1 & p_{f_2}^2 & p_{f_2}^3 \\ p_{f_3}^0 & p_{f_3}^1 & p_{f_3}^2 & p_{f_3}^3 \end{pmatrix} \times \begin{pmatrix} p_A^0 \\ p_A^1 \\ p_A^2 \\ p_A^3 \end{pmatrix} = \begin{pmatrix} p_A^0 \\ R \\ S \\ T \end{pmatrix}, \quad (6.14)$$

where the upper index denotes the fourvector component. The matrix can be interpreted as a partitioned matrix

$$M = \begin{pmatrix} A & B \\ C & D \end{pmatrix} \quad (6.15)$$

with the blocks $A = 1$, $B = (0, 0, 0)$, $C = (p_{f_1}^0, p_{f_2}^0, p_{f_3}^0)^T$ and $D = -(\vec{p}_{f_1}^T, \vec{p}_{f_2}^T, \vec{p}_{f_3}^T)^T$. From the inversion formula for a partitioned matrix one obtains an expression for the three-momentum components of the squark

$$\vec{p}_A = p_A^0 \vec{m} + \vec{n} \quad (6.16)$$

with the vectors $\vec{m} = -D^{-1}C$ and $\vec{n} = D^{-1}(R, S, T)^T$.

Still the fourth equation $p_A^2 = M_A^2 = (p_A^0)^2 - \vec{p}_A^2$ has to be fulfilled, yielding two possible

solutions for the energy component.

$$p_A^0 = \frac{\vec{m}\vec{n}}{1 - \vec{m}^2} \pm \sqrt{\frac{M_A^2 - \vec{n}^2}{1 - \vec{m}^2} + \frac{(\vec{m}\vec{n})^2}{(1 - \vec{m}^2)^2}}. \quad (6.17)$$

From the solution for the squark four-momentum (Eq. 6.16, 6.17) a corresponding LSP momentum can then be calculated. Two solutions per decay branch lead to a total of four combinations of initial parameters per event.

However, in practice it turned out that in many cases no real solution exists, due to a negative expression under the square root. In the SPS1a toy Monte Carlo signal sample only 57% of the events could be completely solved, while in 38% only one branch gave a solution and no solution was found in the rest of the events. The physical reason for this fragility was not studied and needs further investigation. Nevertheless, all events with a full solution were included in the comparison with the other methods.

Random Choice in Slepton Rest-Frame

A third possible choice of the starting values focuses on the two-body-decay of the next to last SUSY particle in the decay chain. In the rest-frame of the decaying particle C (C') the decay products, i.e. the LSP D (D') and the particle f_3 (f_6) which is assumed to be massless, have opposite momentum with a fixed magnitude, given by the masses of the involved particles

$$|\vec{p}_{D/f_3}^*| = \frac{M_C^2 - M_D^2}{2 \cdot M_C}.$$

Two more coordinates are necessary for a full description of their momenta:

- The azimuthal angle ϕ^* , defined in the plane perpendicular to the flight direction of particle C in the laboratory frame.
- The angle θ^* between \vec{p}_D^* and the flight direction of particle C in the laboratory frame.

If the decaying particle has spin 0 or is unpolarized uniform distributions for $\cos \theta^*$ and ϕ^* are expected. A set of initial values following these distributions can be randomly chosen and then be transformed to the laboratory frame. The necessary Lorentz-transformation cannot be determined unambiguously but exploiting the knowledge about the measured decay product f_3 (f_6) an educated guess is possible, e.g. by choosing the one with the smallest boost. Knowing the transformation from the rest-frame of particle C to the laboratory-frame the momentum of D in this reference frame can be calculated. Details on how to obtain the transformation and how to calculate the LSP momentum are given in App. B. A set of 3 $\cos \theta^*$ and 8 ϕ^* values is randomly chosen for each event. This choice is labelled as *rest-frame* method.

Random Momenta

Another random choice is included in the test, which does not make use of any kinematic event information. Momentum components p_x , p_y and p_z are randomly generated in the interval $0 < p < 300$ GeV. For each LSP fifty different momenta are tried. These values may serve as an object of comparison to rate the performance of the more sophisticated methods.

6.2.2 Comparison

The quality of the obtained initial values is compared for all four approaches. The methods are labeled *analytic I* for the solution by Webber, *analytic II* for the calculation using the four mass constraints, *random* stands for random LSP momentum components, and *rest-frame* denotes the method using random values for the decay angles in the slepton rest-frame.

First the agreement of the initial LSP momenta with the true values is compared for the Toy MC in signal events, including all three categories. For each event an initial momentum is generated for both LSPs and the deviation to the corresponding generated particle is determined (Fig. 6.1).

The upper-left figure shows the relative difference $(p_T^{ini} - p_T^{true})/p_T^{true}$, where distributions have been normalized to one for comparison. Both analytic methods show a narrow peak at zero, meaning that the transverse momentum is already very well matching the true value. For the *rest-frame* method the peak is broader and tends towards smaller values, and in case of *random* values the peak is even lower and has a large tail towards high Δp_T .

Looking at the distance in ΔR (upper-right) again the analytic methods perform best and the majority of initial LSPs is actually placed inside a region of $\Delta R = 0.5$, i.e. a typical jet radius. The peak is exactly at zero for *analytic II* and close to it for the *analytic I* method. The *rest-frame* methods reconstructs the position not as precisely but still shows the correct tendency to small distances. In contrast, the distribution of purely random values even rises with increasing ΔR .

The distance can be split into the differences in the η and ϕ coordinates (lower row). As expected from the ΔR distribution, the peaks in the analytic approaches are sharper than for the *rest-frame* variant. This random approach still is a fair approximation, whereas the *random* method hardly delivers a correct η value and completely fails to give the correct ϕ position. This is not surprising since this is a purely random choice and no knowledge about the decay topology is exploited.

The initial momenta quality can be controlled further by studying the agreement of the initial setup with the applied mass and momentum balance constraints. The *random* choice is no longer considered, since obviously the other options perform significantly better. Using the correct assignment of particles in the cascade the invariant masses and p_T -balance can

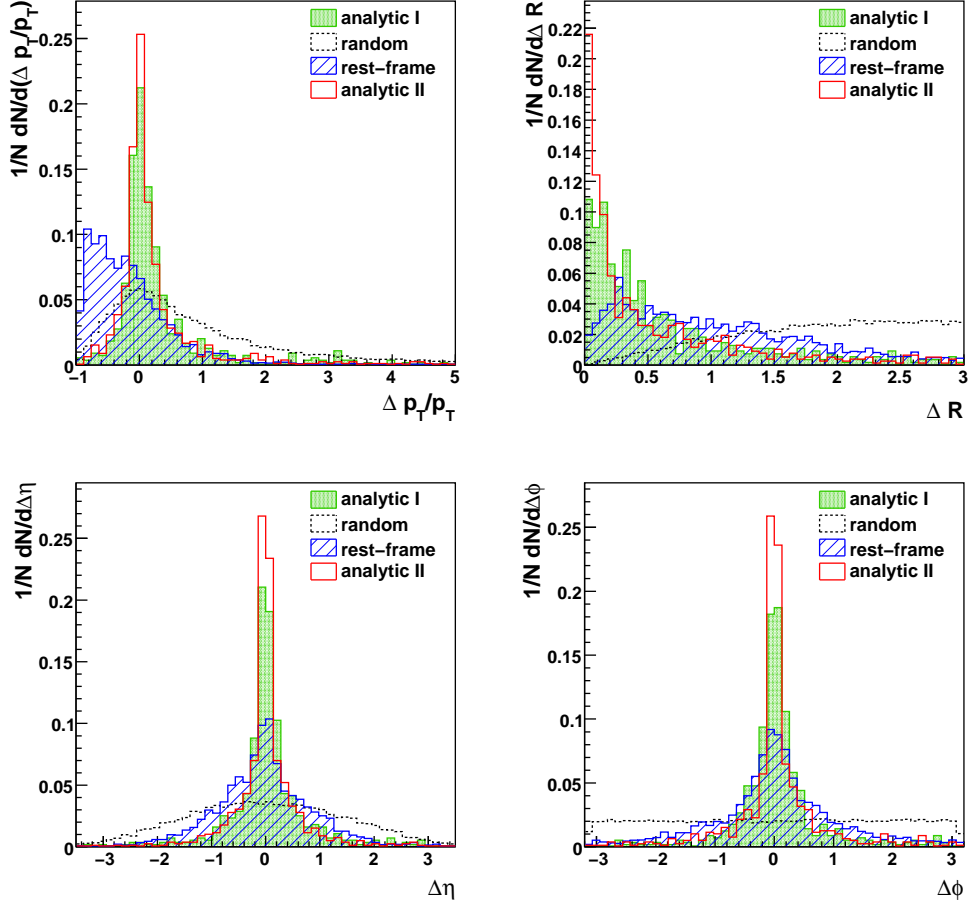


Figure 6.1.: Difference between calculated and true LSP momenta in $(p_T^{ini} - p_T^{true})/p_T^{true}$, ΔR , η and ϕ for the four different methods.

be calculated from the measured final state and the initial LSP vectors (Fig. 6.2).

The *analytic II* method requires that all mass constraints are fulfilled, hence only the momentum constraint (lower-right plot) shows a deviation from zero. For the *analytic I* version the momentum constraint is always fulfilled, whereas the mass constraints are not exactly met. In the calculation the substitution $p_D^2 = M_D^2$ is made which is not respected for the solution fourvector p_D^{ini} . As a consequence the expressions for the SUSY masses derived from Eq. 4.6, e.g.

$$M_C^2 = M_D^2 + 2 \cdot p_{f_3} \cdot p_D + m_{f_3}^2 \neq (p_D^{ini} + p_{f_3})^2 \quad (6.18)$$

do not agree with the invariant mass of the fourvector sum of final states. Here, the

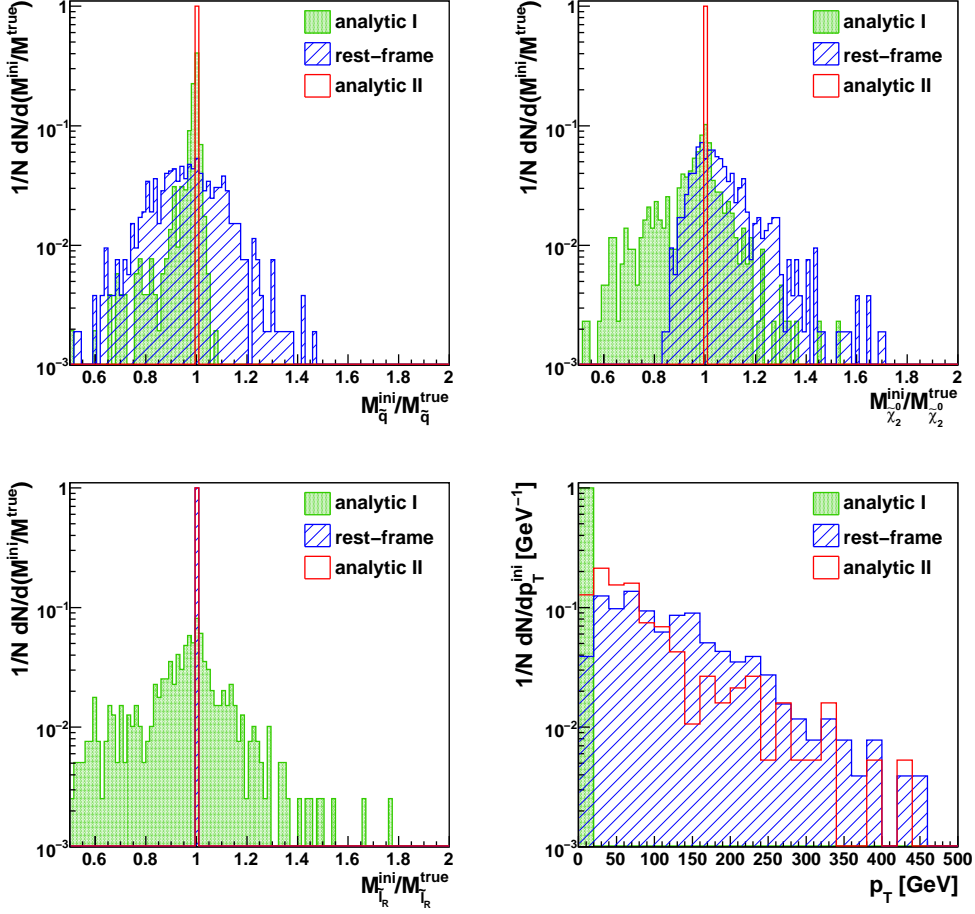


Figure 6.2.: Difference between calculated and true invariant masses and p_T -balance for three different choices of initial LSP momenta.

calculated fourvector p_D^{ini} and its invariant mass M_D^{ini} is used in the calculation of the constraints.

In case of the *rest-frame* method, the LSP and slepton mass constraint are fulfilled by construction. Overall all these initial values seem a fair starting point for the kinematic fit.

Performance with Detector Simulation

It was shown that the determination of suitable initial values with the *analytic I* method works well in case of the Toy MC. This still needs to be confirmed for the detector simulation sample, where the measurement uncertainties may be larger in some cases and the transverse momentum balance is determined with a larger uncertainty. We observe that these effects hardly degrade the agreement of initial and true LSP momenta in Δp_T as well

as in ΔR (Fig. 6.3). The tails of the distributions are a little larger but still the obtained solution is a good approximation.

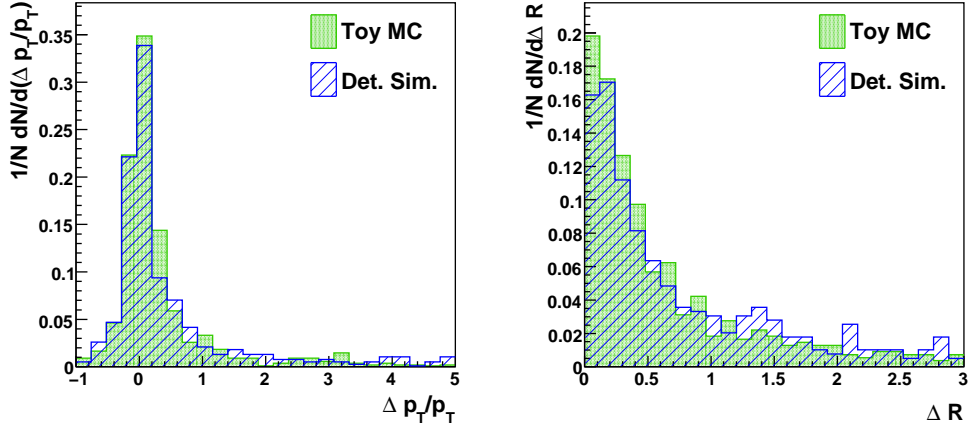


Figure 6.3.: Difference between calculated and true LSP momenta in p_T and ΔR for the *analytic I* method in Toy Monte Carlo and detector simulation sample.

6.2.3 Conclusions

Four methods to generate initial values for the unknown LSP momenta were tested. The analytic methods achieve the best agreement of calculated and true momenta. The *analytic II* method seems to perform best but this approach has the drawback that a solution was found for only 57% of the events. It needs further study and understanding to overcome this limitation.

From two methods with a random component the *rest-frame* method is clearly superior, since it exploits some kinematic information of the event. The purely random choice is the worst possibility.

The outcome of the *rest-frame* method fulfills the LSP and slepton mass constraint, while in case of the *analytic I* values only the p_T -balance is perfectly met and the masses have to be adjusted in the fit. Overall, the significantly better agreement of the LSP momenta and the fact, that it is an analytic solution, leads to the decision to use the *analytic I* method in the further analysis. After all, a surprisingly good agreement is already achieved before the kinematic fit, always having in mind that the true particle masses entered the calculation here.

6.3 Error Treatment

6.3.1 Particle Momentum Resolutions

The full covariance matrix V for the momentum components of measured jets and leptons enters the sum of least squares (Eq. 6.1). Since the reconstruction uncertainties of any two objects in the event are basically uncorrelated the covariance matrix is diagonal.

For the Toy Monte Carlo sample the uncertainties are exactly known and really follow a Gaussian. The values used in the momentum smearing also enter the covariance matrix directly. In case of the detector simulation sample the resolutions determined in Sec. 5.2.1 are assumed (cf. Tabs. 3.1, 5.5, 5.6, 5.7).

6.3.2 Mass Widths

Constraining a SUSY particle mass to exactly the same value in all events and decay branches is not a realistic assumption, since e.g. the squark decay width can be as large as a few GeV. For the weakly decaying neutralinos and sleptons the widths are typically smaller by an order of magnitude.

The way of incorporating this into the fit via an additional parameter (cf. Eq. 6.6) requires the specification of the decay width. Hence three assumptions on the squark, neutralino and slepton mass width have to be made. In case of the squark mass the situation gets complicated by the mass gap between the first two and the third generation squarks. If they are indistinguishable (because no b-tagging is applied) the effective observed mass distribution is much wider. However we have no prior knowledge about the mass gap between the generations and hence assume a small width, compatible with a single generation. In particular the widths are taken directly from the mass spectrum calculator (Tab.6.1).

Also the assumption of a perfect momentum balance in the transverse plane is quite optimistic. In reality an initial imbalance will exist in the parton-parton interaction and the final state can partially escape undetected or suffer from mismeasurements. This results in missing transverse energy in addition to the momentum carried away by the LSPs. This additional component, accounted for with the parameter β in the constraint (Eq. 6.7), is determined differently in Toy Monte Carlo and detector simulation sample.

In the first case the terms of Eq. 6.7 are calculated using the generated momenta of all involved particles. Especially the calculation of the true contribution from out-of-cascade activity is possible in this scenario. The resulting distribution for p_x and p_y is centered around zero and can be fitted with a gaussian, whose width is taken as uncertainty of β .

In the detector simulation sample a treatment of the out-of-cascade activity is more complicated. The best estimate of the momentum balance comes from the measurement of the missing transverse energy in the particle flow event reconstruction. In the fit the component of soft activity $c_{x/y}$ is therefore calculated by subtracting the selected leptons and

jets from the (negative) MET-fourvector. In addition, each jet with a minimum transverse momentum of 30 GeV is considered as additional particle in the p_T -balance constraint and its momentum is also allowed to vary in the fit.

Constraint	Width [GeV]
$m_{\tilde{q}_L}$	5.5
$m_{\tilde{\chi}_2^0}$	0.02
$m_{\tilde{l}}$	0.27
$p_{x/y}$	4.0

Table 6.1.: Widths of constraints as used in the kinematic fit.

Chapter 7

Results

In this chapter the mass determination method is applied on the described SPS1a mSUGRA scenario. First the fit setup is validated using the knowledge about the generator level particle masses and momenta. Then the masses are determined from a scan over possible values.

7.1 Validation of the Fit Algorithm

The kinematic fit is tested on all categories of signal events, choosing the correct assignment of jets and leptons to their positions in the cascade. First the invariant masses are fitted to the true fourvector mass values of the SUSY particles. When background events are included the mean mass values are used instead and the decay width is accounted for by using gaussian mass constraints (cf. Sec. 6.1). This way the performance of the kinematic fit algorithm is first studied independently from background effects and combinatorics.

In the Toy Monte Carlo the measurement uncertainties of the particles used for the gaussian smearing are exactly known. Consequently a covariance matrix with the true variances can be used in the fit. Therefore this scenario provides a first valuable test of the fit implementation and setup.

If the sum of residuals for the measured jet and lepton parameters follows the expected χ^2 -distribution, the corresponding fit probability distribution is uniformly distributed between zero and one. This is almost the case in our setup (Fig. 7.1), although a peak at small values is observed. Imperfections causing this peak enter e.g. in the reconstruction of the p_T -balance of a Toy MC event, when some soft particles fail the acceptance cuts. The fit algorithm converges for 88% of the events.

A further consistency check is made by looking at the size of the parameter corrections determined in the fit (pull distributions). The pull can be defined in two ways: By the comparison to the true Monte Carlo values

$$p_i = \frac{x_i^{fit} - x_i^{truth}}{\sigma_{x_i}} = \frac{\Delta x_i}{\sigma_{x_i}}$$

or by comparison of measured and fitted values, which can also be done on experimental data

$$p_i = \frac{x_i^{fit} - x_i^{meas}}{\sigma_{\Delta x_i}} = \frac{\Delta x_i}{\sigma_{\Delta x_i}}.$$

In this case the correct uncertainty must be used, obtained from the variances of measured and fitted parameters [86]

$$\sigma_{\Delta x_i} = \sqrt{\sigma_{x_i}^2 - \sigma_{x_i^{fit}}^2}.$$

Using the latter definition we observe the distributions Fig. 7.1 (top-right & lower row) for the jet and lepton transverse momenta. As expected, they follow a gaussian with mean zero and $\sigma \approx 1$. The standard deviation is slightly smaller than 1 because only events with $\text{Prob}(\chi^2) > 0.05$ are considered, in order to exclude the peak at zero fit probability. Out of all converged events, 14% fall below this threshold. Pulls for the angular parameters η and ϕ also show this behaviour and are provided in App. C.

Another benchmark is the reconstruction of the unmeasured LSP momenta. Their initial values already approximate their true momenta well (cf. Sec. 6.2) and are further optimized in the fit. A comparison shows that the deviation from the true values is indeed further reduced after the fit (Fig. 7.2). The significant improvement illustrates the power of the applied kinematic constraints.

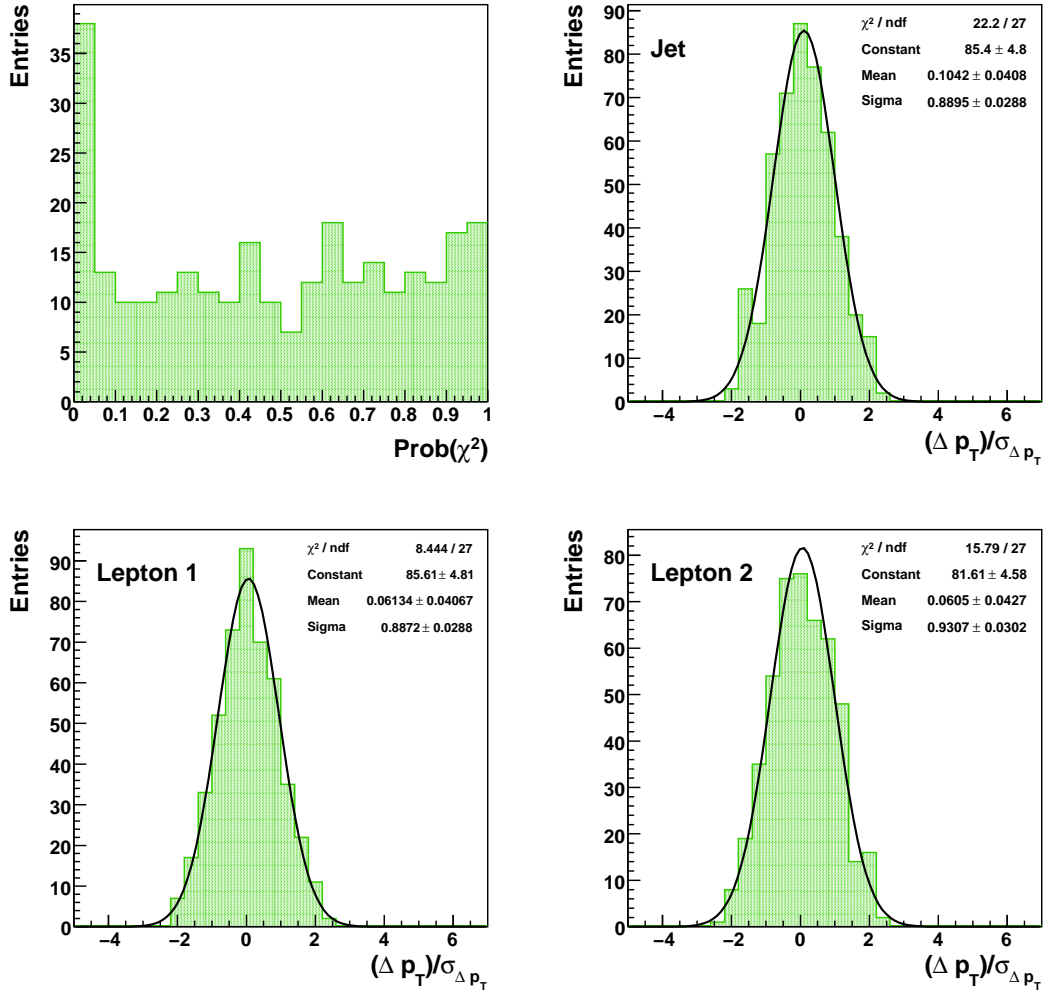


Figure 7.1.: Fit probability distribution for signal events using the true masses in Toy Monte Carlo and pull distributions ($\Delta p_T = p_T^{\text{meas}} - p_T^{\text{fit}}$) with fitted gaussian for jet and lepton p_T in events with $\text{Prob}(\chi^2) > 0.05$. The correct lepton and jet positions in the cascade are used.

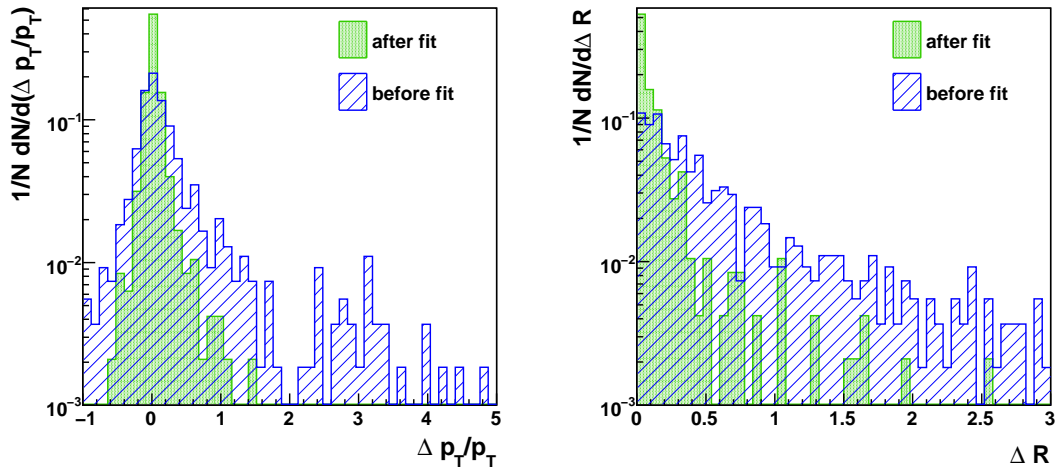


Figure 7.2.: Relative difference in p_T and distance in ΔR of LSP four-momenta to the true values before and after the kinematic fit. The correct position of jets and leptons in the cascade and the true masses are used. Only events with $\text{Prob}(\chi^2) > 0.05$ are shown.

The Combinatorial Problem

Positions in the cascade have to be assigned to six out of all selected particles, which yields at least 8 possible permutations in case of four leptons and only two jets (cf. Sec. 5.1.1). Each of these combinations has to be tested in the fit and each time the initial LSP momenta have to be calculated beforehand. A plausible criterion to select the best combination is the χ^2 value, also denoted as S before (cf. Eq. 6.1). The fit with the smallest value (and therefore the largest fit probability) is chosen and the assignment of the final state particles is controlled and summarized in four categories (Tab. 7.1).

Category	Percentage of events
Wrong jet	7%
Wrong lepton pairing	1%
Lepton pair assigned to wrong squark	2%
Leptons exchanged on same branch	38%
Correct assignment	52%

Table 7.1.: Particle assignment after kinematic fit with true masses in Toy Monte Carlo. The combination with smallest χ^2 is chosen.

An additional jet from initial or final state radiation or a gluino decay is sometimes preferred over the correct ones (7% of events). In very few cases a wrong lepton pairing is found (1%) or a lepton pair is assigned to the wrong jet (2%). The small numbers show that the two decay branches are kinematically different and the fit is capable of distinguishing between them with high efficiency.

However, the determination of the lepton position on a branch is more difficult. Only 52% of the events show the correct assignment but 38% have positions switched in one or both lepton pairs. Looking closer at this category of events with the correct lepton pair-jet association, we find that the fraction of correct assignments is 0.57, while the other three possibilities, i.e. the lepton positions switched on the first branch, on the second branch or on both branches, are found in only 16%, 17% and 9% of the events, respectively. Hence, the fit has quite some power to distinguish between the correct and wrong lepton positions, although a better performance could have been expected from a precise lepton momentum measurement.

The cause of this difficulty lies in the lepton kinematics. The leptons come from two decays with a similar mass difference of $\Delta M(\tilde{\chi}_2^0, \tilde{l}_R) = 37 \text{ GeV}$ and $\Delta M(\tilde{l}_R, \tilde{\chi}_1^0) = 46 \text{ GeV}$ and the entire system is boosted due to the decay of the heavy squark. Therefore the observed p_T spectra for the two leptons are almost identical and also their directions are similar in many events, due to the Lorentz boost. Since the LSP momenta are not measured, a wrong lepton combination may yield the correct masses, despite the good lepton momentum resolution.

As an effect of choosing the combination with smallest χ^2 -value the distribution of the fit probability gets shifted towards larger values, because a wrong combination is only accepted if its probability is larger than the one of the correct assignment. This can be seen from Fig. 7.3 (green histogram) when comparing to Fig. 7.1 (upper-left plot).

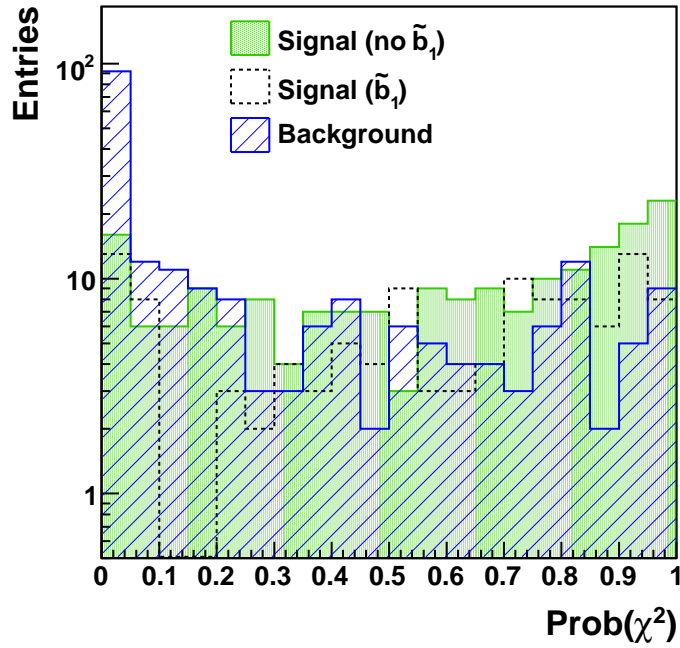


Figure 7.3.: Fit probability distribution in Toy MC for signal, divided into events containing a \tilde{b}_1 and all others, and the SUSY background. The particle permutation with smallest χ^2 is chosen in each event.

In a fit including SUSY background events (Fig. 7.3) a mass hypothesis has to be used, for which the central values of the true mass distributions are chosen here. The majority of background events is found at very low probabilities, while the remaining ones show a flat distribution. The existence of some well fitting background events is not unexpected, since many of them contain decay chains which are very signal-like (cf. Sec. 5.2.2).

Events containing a light sbottom (\tilde{b}_1) are plotted separately because its mass lies about 45 GeV below the value assumed in the fit. We observe that a large fraction of \tilde{b}_1 -events are located at very low fit probability but surprisingly the distribution of the remaining ones is almost flat and even shows a small shift towards larger values. It seems that the LSP and measured momenta can be adjusted to be compatible with the higher squark mass, despite the other kinematic constraints.

Detector Simulation Sample

For the detector simulation sample the same distributions are considered to check the fit performance. Only signal events with a complete and unambiguous matching (cf. Sec. 5.2.1) of reconstructed particles to the cascade partons and leptons are included.

In the probability distribution (Fig. 7.4) the peak at zero is increased w.r.t to the Toy MC. Otherwise the distribution is still reasonably flat.

Reasons for this effect are that particle resolutions entering the covariance matrix are only approximated in case of the detector simulation sample and particles may also fall into non-gaussian tails of momentum resolutions. Furthermore the momentum balance is affected by the finite resolution of the missing E_T measurement. Modifying the Toy MC such, that the measured missing E_T is emulated by smearing the LSP p_T with the appropriate resolution, results in an increased peak at small values in the Toy MC fit probability distribution.

The transverse momenta pull distributions are again in good agreement with the expectation, showing that overall the uncertainty assumptions are adequate.

Still the LSP momenta are well adjusted in the fit (Fig. 7.5) and no difference to the Toy Monte Carlo fit performance is visible.

Including combinatorics in the fit, again a shift towards larger probabilities is observed (Fig. 7.6). However, the signal peak at lowest probabilities remains large for both signal categories. Similarly, the majority of background events accumulates at low probabilities and a cut at an intermediate value (e.g. $\text{Prob}(\chi^2) > 0.3$) would yield an almost background free sample.

Investigating the association of final state particles to the position in the cascade (Tab. 7.2), we find a slight degradation of the performance w.r.t to the Toy MC, which is attributed to the mentioned resolution effects.

Category	Percentage of events
Wrong jet	7%
Wrong lepton pairing	2%
Lepton pair assigned to wrong squark	5%
Leptons exchanged on same branch	40%
Correct assignment	46%

Table 7.2.: Particle assignment after kinematic fit with true masses in detector simulation sample. The combination with smallest χ^2 is chosen.

The fraction of wrong jet selections remains the same but finding the correct lepton pairs and associating them to the correct branch fails more frequently. Also an exchange of leptons on the same branch happens more often, although the correct lepton combination is still found more than twice as often (53%) as any other lepton permutation (max. 19%), which is much better than in a random assignment.

In summary, the kinematic fit works very well in the chosen setup for both event samples and powerfully reconstructs the event kinematics when provided the correct SUSY masses.

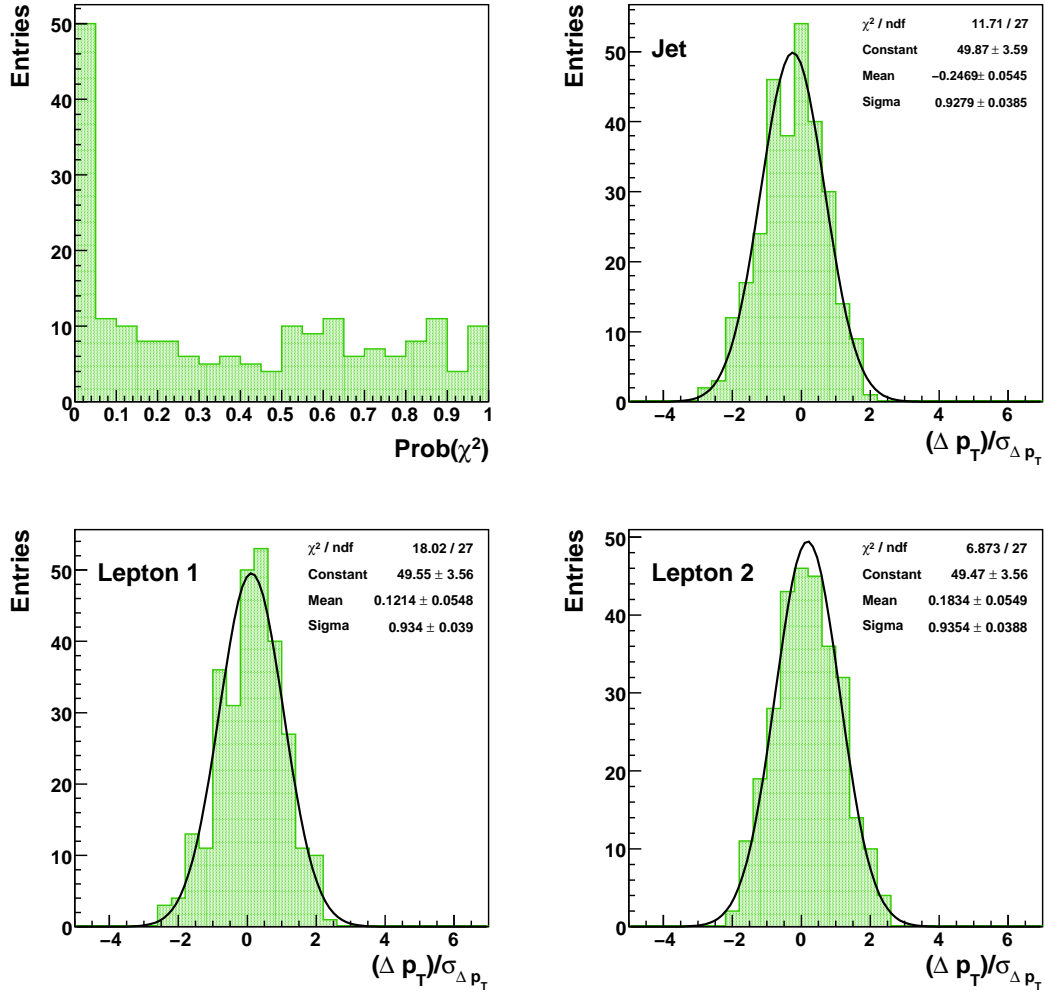


Figure 7.4.: Fit probability distribution for signal events using the true masses in detector simulation sample and pull distributions $(\Delta p_T = p_T^{\text{meas}} - p_T^{\text{fit}})$ with fitted gaussian for jet and lepton p_T in events with $\text{Prob}(\chi^2) > 0.05$. The correct lepton and jet positions in the cascade are used.

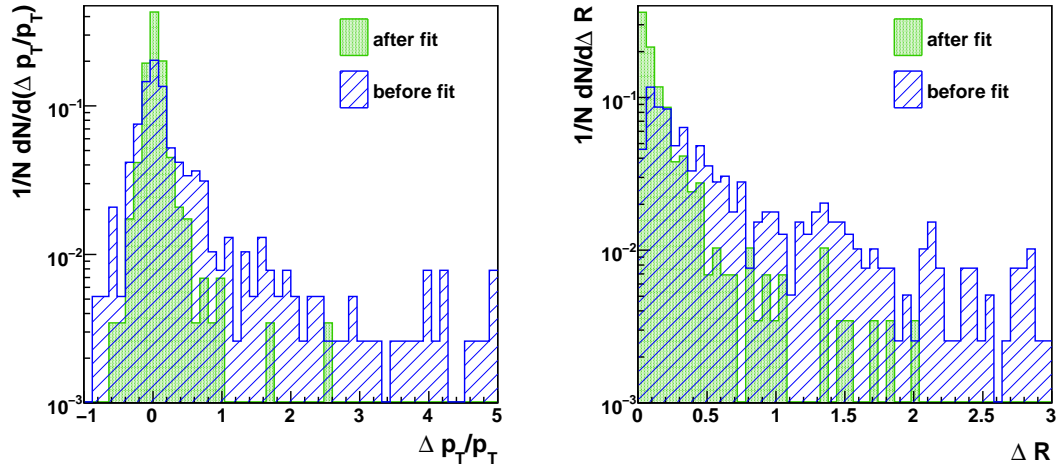


Figure 7.5.: Relative difference in p_T and distance in ΔR of LSP four-momenta to the true values before and after the kinematic fit in detector simulation sample. The correct position of jets and leptons in the cascade and the true masses are used. Only events with $\text{Prob}(\chi^2) > 0.05$ are shown.

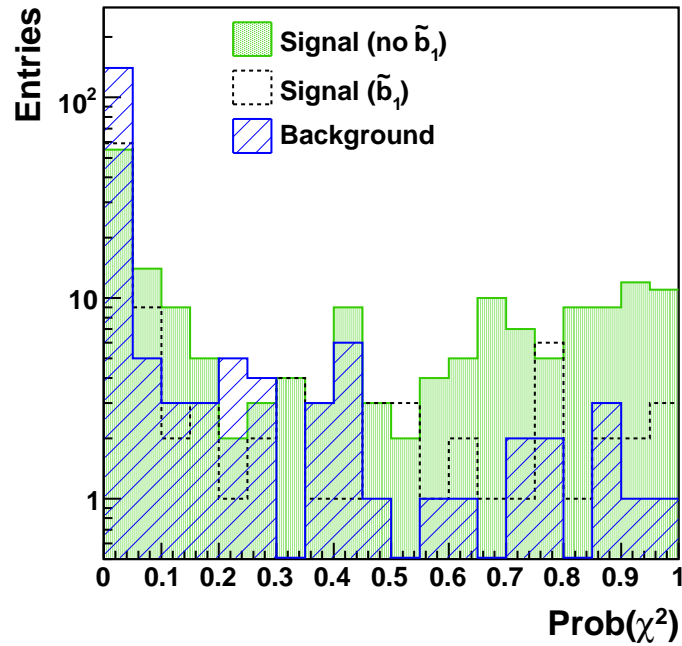


Figure 7.6.: Fit probability distribution in detector simulation sample for signal, divided into events containing a \tilde{b}_1 and all others, and the SUSY background. The particle permutation with smallest χ^2 is chosen in each event.

7.2 Combining Events

An important aspect of the mass determination method is the combination of kinematic information from many events. Each event is fitted individually to a set of mass hypotheses and at first sight two options for a combination exist.

The fits could be combined *event-wise*, meaning that the best fitting mass hypothesis for each single event is determined and the distribution of their best hypotheses is used to draw conclusions on the true masses. However, this approach will not be successful because a single event has not sufficient constraints to determine the unmeasured LSP momenta and all of the four masses. Hence, for each event a mass scan will only reveal hyperplanes of perfectly fitting masses instead of a single best mass point.

The second option is an *hypothesis-wise* combination in which the fit results of all events for a single mass hypothesis are combined and the distribution of such a combined result for all different mass hypotheses is analyzed. In order to best exploit the available information, each event should be considered at each tested mass hypothesis, no matter if its compatibility is high or low, since in principle we assume that each event contains the same decay chain. The question is how to construct a meaningful quantity, which effectively combines the information, and ideally has well-defined statistical properties.

The key figure, characterizing each fit result, i.e. the compatibility with the assumed mass hypothesis, is the squared sum of residuals (χ^2 or S as defined in Eq. 6.1), which in case of the true masses should follow the χ^2 probability density function (p.d.f.). The χ^2 probability is obtained by integration.

An option to construct a likelihood from the fit results is to use the underlying p.d.f. of S , i.e. the χ^2 -function. For k degrees of freedom it is given as

$$f_{\chi}(x, k) = \frac{1}{2^{k/2}\Gamma(k/2)} \cdot x^{k/2-1} e^{-x/2}.$$

The total likelihood for N events with fit results S_i can then be written using this p.d.f.

$$L = \prod_{i=1}^N f_{\chi}(S_i, k).$$

It is common to take the negative logarithm of the likelihood

$$-\ln L = -\sum_{i=1}^N \ln(f_{\chi}(S_i, k)),$$

which in our case of 2 degrees of freedom becomes

$$-\ln L = -\sum_{i=1}^N \ln\left(\frac{1}{2}e^{-S_i/2}\right) = \frac{1}{2} \cdot \sum_{i=1}^N S_i + \text{const.} \quad (7.1)$$

Since for an interpretation of the likelihood we are interested only in differences $\Delta(-2\ln L)$ and not in absolute values the constant term can be neglected. Actually the difference then becomes

$$\Delta(-2\ln L) = \Delta\left(\sum_{i=1}^N S_i\right) \quad (7.2)$$

and is identical to the difference of the sum of S values. Hence, maximizing the likelihood Eq. 7.1 is equivalent to a minimization of the sum of S values.

Note that this correspondence only exists for the special case of $k = 2$ with a purely exponential dependence of f_X , otherwise additional non-constant terms $\ln x^{k/2-1}$ enter.

This definition of the likelihood needs to be slightly modified to account for two effects. It is not unlikely that for some events no solution is found in the kinematic fit and the algorithm does not converge. However, the number of events entering the likelihood must be constant for all hypotheses to preserve the statistical meaning. Therefore a regularization value S_{reg} is used for all events without a proper fit solution.

The second issue is the numerical stability in case of poor agreement with the hypothesis. If S is large, its exact value has little meaning, since the topology just does not fit to the hypothesis and depends more on the numerical minimization process. In order to avoid large fluctuations the regularization value S_{reg} is used as an upper bound for accepted fit probabilities. Neglecting the constant term in Eq. 7.1 the likelihood is finally calculated as

$$2\ln L = -\sum_{i=1}^N \min(S_{\text{reg}}, S_i) \quad (7.3)$$

In the following a value of $S_{\text{reg}} = 2.41$ corresponding to $\text{Prob}(S_{\text{reg}}) = 0.3$ is chosen, which in addition excludes most of the background events, when fitting the true masses (cf. Fig. 7.6).

Interpreting the obtained distribution of $\Delta(-2\ln L)$ as a likelihood for the simultaneous determination of the four mass parameters the confidence intervals for $m = 4$ in Tab. 7.3 apply. In reality such an interpretation is difficult because the shape of the likelihood contour is influenced by several factors. While the effect of the regularization cut-off may be small in the vicinity of the extremum, the shift towards larger fit probabilities when including combinatorics is not negligible and leads to an enhancement of the extremum (cf. Sec. 7.4.3). Also the step size of the mass scan (cf. Sec. 7.4.1) can lead to deformations. Therefore the observed $\Delta(-2\ln L)$ intervals may not correspond to the real uncertainties, which would have to be evaluated e.g. by repetition of the experiment on different event samples.

Coverage probability (%)	$m = 1$	$m = 2$	$m = 3$	$m = 4$
68.27 (1σ)	1.0	2.3	3.53	4.72
95.45 (2σ)	4.0	6.18	8.02	9.72
99.73 (3σ)	9.0	11.83	14.16	16.25

Table 7.3.: $2\Delta \ln L$ corresponding to the given coverage probability for joint estimation of m parameters.

7.3 Visualization

Having introduced and validated the kinematic fit and outlined how to exploit the joint information of many events, a scan over possible mass values is the last missing piece. In this scan hypothetical values for the masses of the squarks, neutralinos and sleptons are defined on a four-dimensional mass grid and each hypothesis is tested in the fit.

Clearly a visualization of the likelihood in four dimensions is not possible and it needs to be projected into fewer dimensions, i.e. two or even one mass variable, for visual analysis. Such a projection has to be made in a way that the confidence region determined for the remaining variable also is compatible with the same coverage probability for the other, undisplayed masses.

One possible approach is the following: for each point in the reduced $(n - 1)$ -dimensional grid, the value of the projected dimension which maximizes the likelihood is selected. This can be repeated until the desired dimensionality is reached.

The effect of this approach can be illustrated in two dimensions. Starting from two random variables Θ_i and Θ_k , each following a Gaussian distribution with mean zero and $\sigma = 1$, a histogram of the correlated variables Θ_i and $\Theta_j = \Theta_k - 0.5 \cdot \Theta_i$ is created. The log-likelihood is determined from the histogram bin-contents N as $2 \cdot \ln(N)$. This is analog to a scan of the likelihood contour with the kinematic fit. The difference to the maximum likelihood value is shown in the 2D-histogram Fig. 7.7, left. The contour of the 1σ confidence region for the joint estimation of two parameters is indicated with the dash-dotted line, corresponding to $2\Delta \ln L = 2.3$.

In the projection on the Θ_j -axis the largest likelihood for all Θ_i coordinates is taken for each bin and the bin center set as coordinate for the graph x -axis. The selected bins are indicated with the black markerline. The projection is basically a cut through the two dimensional plane.

The resulting one-dimensional curve (Fig. 7.7, right) has a parabolic shape and is fitted to determine the position of the maximum and its width. The points where the function has dropped to $f_{max} - 2.3$ are marked. Obviously the 1σ interval is the same as determined from the 2-dimensional distribution. Choosing the parameter region with $f_{max} - 1$ a width of $\Delta\Theta_j = \pm 1.15$ is found, which agrees well with the standard deviation of the original gaussian distribution ($\sigma = 1.13$).

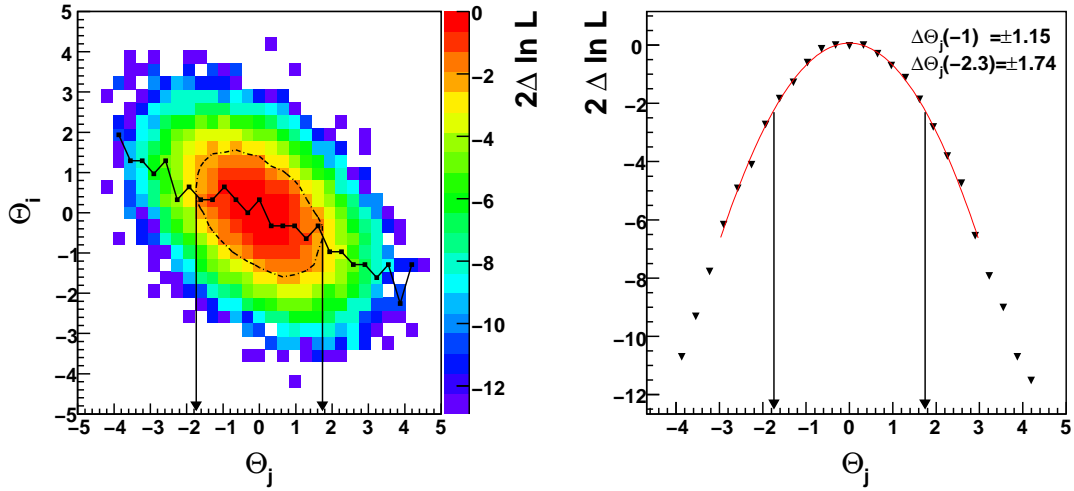


Figure 7.7.: Left: Log-likelihood distribution for correlated variables with Gaussian distribution. The dash-dotted line shows the 1σ -contour. The markerline indicates the bins with largest likelihood for a fixed Θ_j . Right: Likelihood values along the marked line. A parabola fit yields the given Θ_j intervals values for $2\Delta \ln L$ -differences of 1 and 2.3.

Due to fluctuations in the bin-contents the x-section is not a straight line. However, it approximates a line through the points where the error ellipse becomes tangent to a vertical. Fig. 7.8 [16] illustrates this for an ideal error ellipse. The values of Θ_i which maximize the likelihood for a given value of Θ_j are indicated with the dotted line and the intersection of this line with the error contour yields the correct uncertainty σ_j . An advantages of this

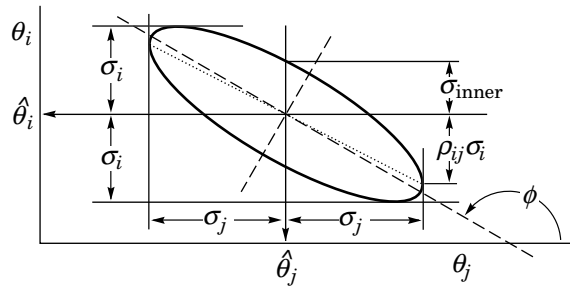


Figure 7.8.: Left: Ideal 2D error ellipse [16]. The dotted line show the values of Θ_i which maximize the likelihood for a given value of Θ_j .

procedure are that the $2\Delta L$ -values for the confidence intervals are preserved and respect the correlations.

7.4 Mass Determination

7.4.1 Mass Scan on Signal Events

Finally, mass hypotheses are tested in order to determine the masses of the involved particles. First, only signal events containing the cascade Fig. 5.2, with two \tilde{q}_L ($\tilde{q} = \tilde{u}, \tilde{d}, \tilde{c}, \tilde{s}$) as initial particles are considered, scanning on a four-dimensional mass grid as defined in Tab. 7.4 and taking into account all combinatorial possibilities. Identical particles on both branches are assumed to have the same mass. The mass widths assumed in the gaussian constraints are not varied.

Particle	$M_{\min.}$ [GeV]	$M_{\max.}$ [GeV]	ΔM [GeV]
\tilde{q}_L	470	650	10
$\tilde{\chi}_2^0$	100	400	10
\tilde{l}_R	60	210	10
$\tilde{\chi}_1^0$	0	120	10

Table 7.4.: Grid of mass hypotheses for scan.

The resulting likelihood distribution, after application of the described projection technique, shows a good correspondence of its extremum with the true central value of the cascade particle masses (Fig. 7.9). The average χ^2/ndf per event of about 0.75 at the extremum is reasonable and decreases to 0.6 if only counting events with a complete matching of jets and leptons to generated particles. In such events the blurring effects of e.g. hadronization and jet reconstruction are rather small and a better average χ^2 is not surprising. A regularization cut-off corresponding to $\text{Prob}(\chi^2) = 0.3$ is chosen, which excludes most background events when fitting the true masses (cf. Fig. 7.6). Correlations among the masses are observed, which are quite strong for the lower part of the decay chain ($\tilde{\chi}_2^0$, \tilde{l}_R , $\tilde{\chi}_1^0$).

In the squark mass diagrams (first three plots of Fig. 7.9) a decrease is visible towards the upper-left corner, along a line of constant mass difference to the second mass variable. It has its origin in the correlations among the three lower particle masses, as will become clear later. The extremum for the squark mass is rather insensitive to correlation effects in the rest of the decay chain, due to the fact that all three measured particles on the branch enter the squark-mass constraint.

A particularly strong correlation is found between the $\tilde{\chi}_2^0$ and \tilde{l}_R masses, where the best hypotheses lie on a diagonal line which corresponds to the true mass difference of about 37 GeV within the binning resolution. A stretched but clear absolute extremum is observed, covering the true mass values with its upper end. Due to the strong correlation the two plots of $\tilde{\chi}_2^0 / \tilde{l}_R$ versus the squark mass (upper row Fig. 7.9) have a similar likelihood contour.

A good reconstruction of the mass difference is not surprising, since the invariant masses of neutralino and slepton differ only by the contribution of the second lepton, which is measured very precisely. Even with a slightly wrong LSP fourvector, i.e. in the vicinity of the true $\tilde{\chi}_2^0 / \tilde{l}_R$ masses, the difference of the invariant masses will not change much. Deviations from the true difference are more likely to be accepted by the fit if they tend towards larger values (good hypotheses lie below the line of the true mass difference), which can be understood looking at the interplay with the LSP mass variable.

All three distributions involving the LSP mass show the same feature. Beside a well positioned total extremum a band of good hypotheses is visible, reaching from the true LSP mass down towards zero. This band becomes more prominent when including the other categories of signal events (cf. Sec 7.4.3). Its ridge in the slepton-LSP mass plane (lower right plot Fig. 7.9) is slightly bent, i.e. it is not found along the line of a constant mass difference. While starting at the true $M_{\tilde{l}} - M_{\tilde{\chi}_1^0} = 46 \text{ GeV}$ for the correct LSP mass, it tends towards larger values when approaching $m_{\tilde{\chi}_1^0} = 0$.

The reason why $m_{\tilde{\chi}_1^0}$ so far below the true value can provide a good χ^2 -sum is that it is only indirectly constrained in the fit, i.e. only through its contribution to the invariant masses further up the chain. The $\tilde{\chi}_1^0$ mass appears in combination with its three momentum in the energy component of the fourvector sum and hence any LSP mass may be compatible if only the momentum components can be adapted accordingly. If the LSP momentum has a large absolute value, the influence of the mass term is small. This means that the restrictions on p_x and p_y in the momentum balance constraints are of great importance, which in turn is related to the precision of all momentum measurements. This aspect is further discussed below.

Having in mind the rather weak restrictions on the $\tilde{\chi}_1^0$ mass, the shape of the band of good likelihood values can be further understood recalling a well known phenomenon, the dilepton mass edge of the decay $\tilde{\chi}_2^0 \rightarrow \tilde{l}_R + l^\pm \rightarrow \tilde{\chi}_1^0 + l^\pm + l^\mp$, which builds the lower part of our signal decay chain. The maximum lepton pair invariant mass is given by Eq. 4.1 (cf. Sec. 4.2) and can be rewritten as a product of linear mass differences and sums

$$\begin{aligned} (m_{ll}^{max})^2 &= \frac{(m_{\tilde{\chi}_2^0}^2 - m_{\tilde{l}_R}^2)(m_{\tilde{l}_R}^2 - m_{\tilde{\chi}_1^0}^2)}{m_{\tilde{l}_R}^2} \\ &= \frac{(m_{\tilde{\chi}_2^0} + m_{\tilde{l}_R})(m_{\tilde{\chi}_2^0} - m_{\tilde{l}_R})(m_{\tilde{l}_R} + m_{\tilde{\chi}_1^0})(m_{\tilde{l}_R} - m_{\tilde{\chi}_1^0})}{m_{\tilde{l}_R}^2}. \end{aligned} \quad (7.4)$$

The triangular shape of the m_{ll} distribution means that a large fraction of events actually have a dilepton invariant mass close to the maximum value (cf. Fig. 7.10). Therefore it is difficult or even impossible for the fit to adjust the lepton momenta such, that these events become compatible with a lower m_{ll}^{max} . This leads to the strong drop at the upper edge of the likelihood distributions, since for a fixed slepton mass a decrease of $m_{\tilde{\chi}_2^0}$ would lead

to a lower m_{ll}^{max} , which for the events close to the dilepton edge results in a large fit χ^2 . The same argument holds for the $\tilde{\chi}_1^0$ whose mass cannot be increased without violating this kinematic requirement.

Taking into account that the $m_{\tilde{\chi}_2^0} - m_{\tilde{l}_R}$ mass difference is precisely found with its true value in the scan, the shape of the $m_{\tilde{l}_R}$ vs. $m_{\tilde{\chi}_1^0}$ likelihood contour can be further understood from Eq. 7.4. If $m_{\tilde{l}_R}$ is tested at a lower value and the best hypotheses therefore also lie at an equally lower $m_{\tilde{\chi}_2^0}$, the only way to preserve the m_{ll}^{max} value is to increase the mass difference between slepton and LSP, which means to favor hypotheses below the diagonal line of the true mass difference. The smallest value the slepton mass can reach under these assumptions is obtained by inserting $m_{\tilde{\chi}_1^0} = 0$, the true m_{ll}^{max} value, and the true mass difference $m_{\tilde{\chi}_2^0} - m_{\tilde{l}_R} = 37 \text{ GeV}$ in Eq. 7.4, yielding a value of $m_{\tilde{l}_R}^{min} \approx 68 \text{ GeV}$.

However, the observed ridge does not reach this smallest possible mass difference but broadens towards larger slepton masses (i.e. larger differences) which is related to the measurement uncertainties in the event.

Considering the described relations between the scan result and the dilepton mass edge it seems a natural extension to the kinematic fit method to incorporate a mass edge measurement. This could help to improve the mass resolution and especially to fix the overall mass scale by compensating the weak LSP mass constraints. This ansatz is further pursued in Sec. 7.5.

Combinatorics

In the validation of the fit implementation it was shown, that combinatorics shift the χ^2 -probability distribution towards larger values. Therefore a better likelihood value is expected on average in case combinatorics are included. Actually, the best total χ^2 -value for $\tilde{q}_L \tilde{q}_L$ signal events increases from 0.75 to 1.0 if only the correct assignment is considered (cf. Fig. 7.9 and Fig. 7.11). While the extremum keeps its position and the correlations remain, the likelihood contour is flattened and small $\tilde{\chi}_1^0$ -masses become even more compatible. The picture does not change when using only events in which all cascade jets and leptons can be matched to generated particles.

Integrated Luminosity

The shape of the likelihood distribution depends on the amount of analyzed data. Fitting only 50% of available signal events ($\tilde{q}_L \tilde{q}_L$) the ridge in $m_{\tilde{l}_R} - m_{\tilde{\chi}_1^0}$ is less pronounced and compatibility of small LSP masses cannot be excluded (left plot Fig. 7.12).

A cumulative effect is expected when fitting more events. Only by addition of many events the common mass regions with good fits become visible, since a single event has not sufficient constraints to determine the missing LSP momenta and the masses of the SUSY particles at the same time. Also an event may contribute strongly to the observed

maximum with a very good fit probability close to the true masses and by the inclusion of more such strong events the extremum becomes clearer.

For a duplication of integrated luminosity it is observed that the band at small $\tilde{\chi}_1^0$ masses further narrows (right plot Fig. 7.12) but does not vanish. The intrinsic weakness concerning the LSP mass is not cured by an increased integrated luminosity.

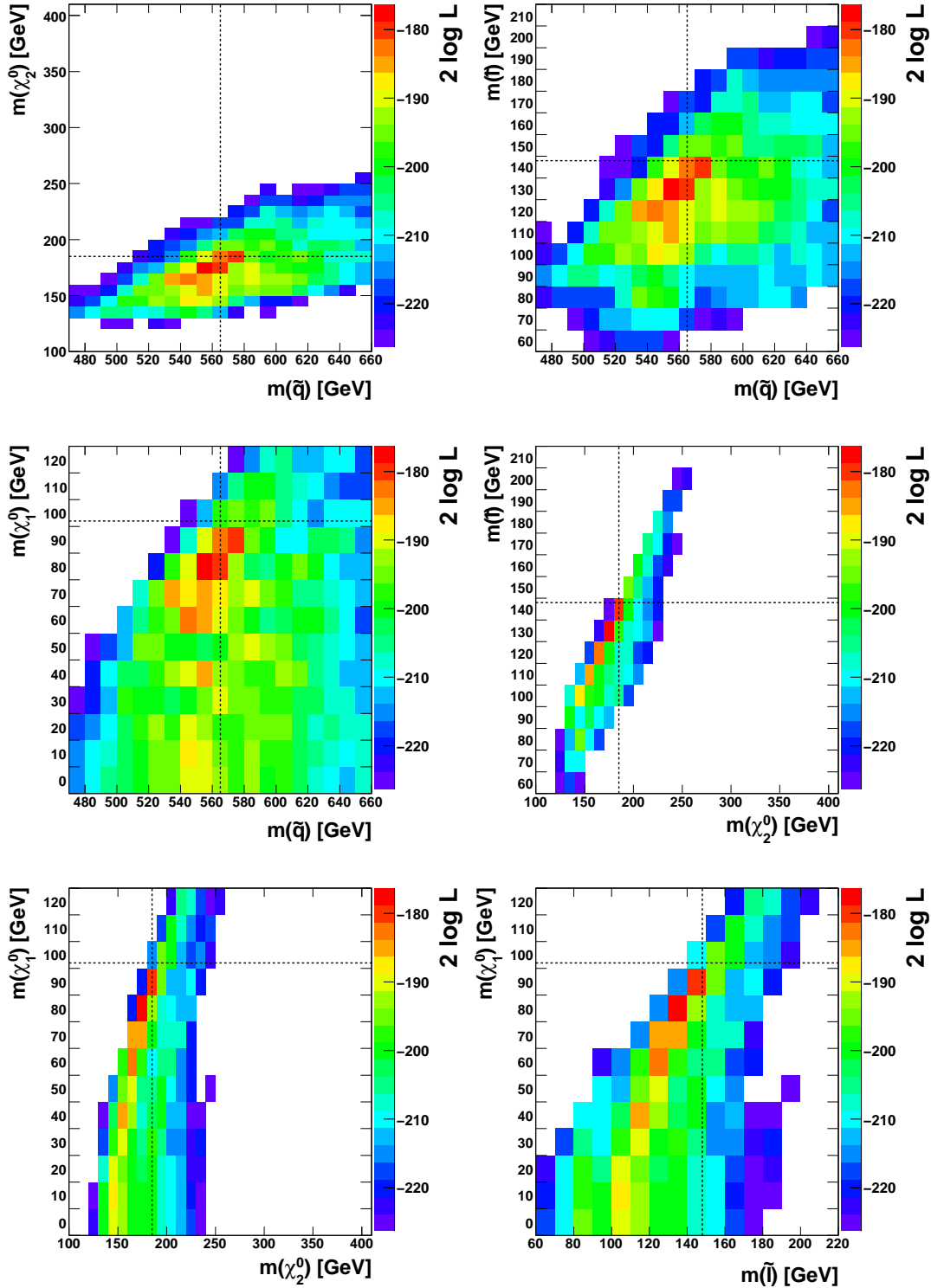


Figure 7.9.: All possible 2-dimensional projections of the mass scan for $\tilde{q}_L \tilde{q}_L$ signal events in the detector simulation sample with full combinatorics. Each bin corresponds to a tested mass hypothesis and the bin content is calculated according to Eq. 7.3 with a cut-off at $\text{Prob}(\chi^2) = 0.3$. White areas lie below the minimal displayed z-axis value or were not scanned due to the mass hierarchy. True values of SUSY masses are indicated by black dashed lines.

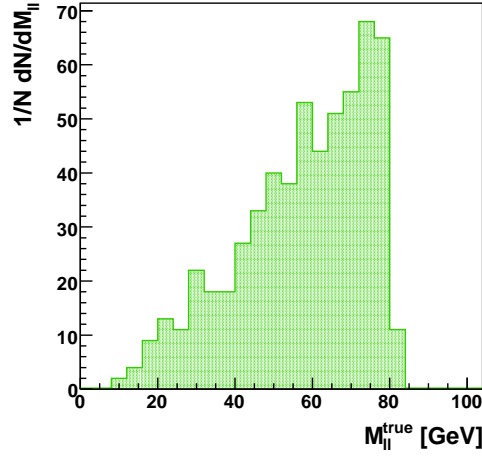


Figure 7.10.: Generated lepton pair invariant mass distribution in signal events with typical triangular shape.

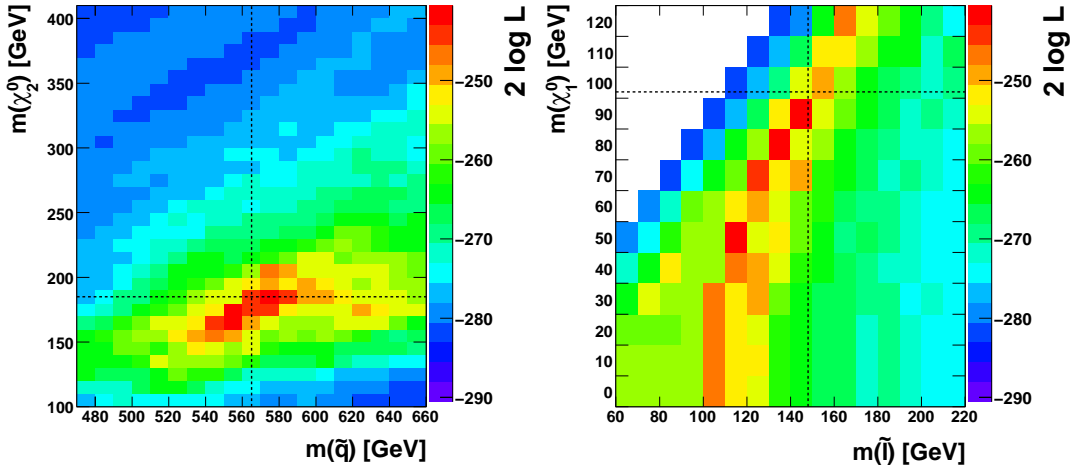


Figure 7.11.: Projections of the mass scan for $\tilde{q}_L \tilde{q}_L$ signal events in detector simulation sample without combinatorics. True values of SUSY masses are indicated by black dashed lines.

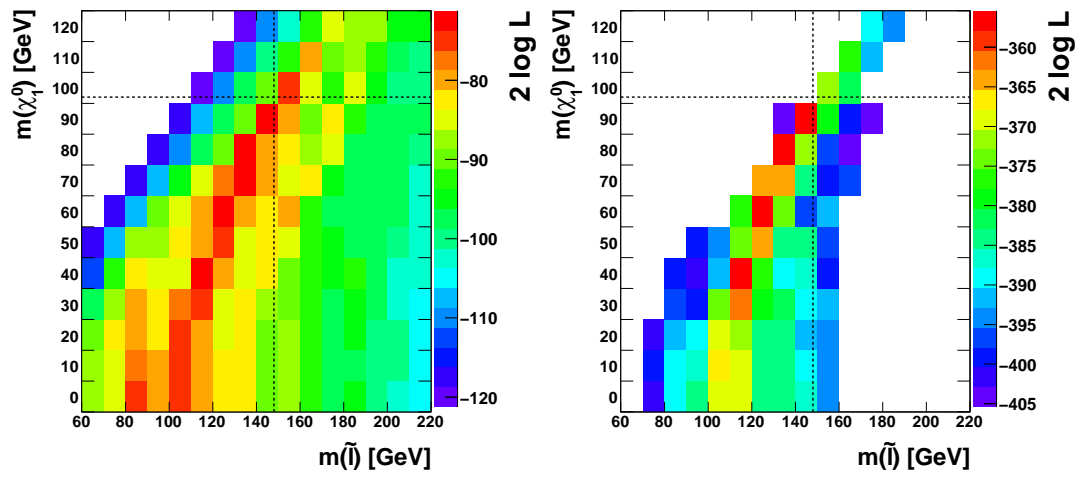


Figure 7.12.: Projections of the mass scan for $\tilde{q}_L \tilde{q}_L$ signal events in detector simulation sample with full combinatorics for different luminosities. Left: 70 fb^{-1} . Right: 280 fb^{-1} . True values of SUSY masses are indicated by gray dashed lines.

7.4.2 Toy MC Study of Measurement Resolutions

The impact of the measurement resolutions of leptons, jets and missing E_T is evaluated by means of varying resolution assumptions. For technical reasons this is done using the Toy MC, keeping in mind the known differences to the detailed simulation (cf. Sec. 5.3).

Electrons and muons are measured very precisely whereas jets are the physics objects subject to the largest reconstruction uncertainties, especially if carrying little transverse momentum (cf. Sec. 5.2.1). Given also the high jet multiplicity at a hadron collider their resolutions are the crucial factor for any precision measurement involving different types of particles. Therefore a variation of the jet p_T resolutions will have the strongest impact on the scan result.

Two options exist to calculate a missing E_T in the Toy MC. Either by summing over all measured (i.e. smeared generator) particles, including those in the forward regions and at very low p_T , or in a more detector reality inspired way by taking the true generator missing E_T , i.e. the transverse momenta of all unmeasured particles (neutrinos, neutralinos), and smearing it with the experimental missing E_T resolution.

The first approach shows a very narrow missing E_T resolution, significantly better than the one obtained in the smearing method (Fig. 7.13). Hence, the influence of the missing E_T measurement precision can be evaluated comparing scans with either of the methods applied in the Toy MC.

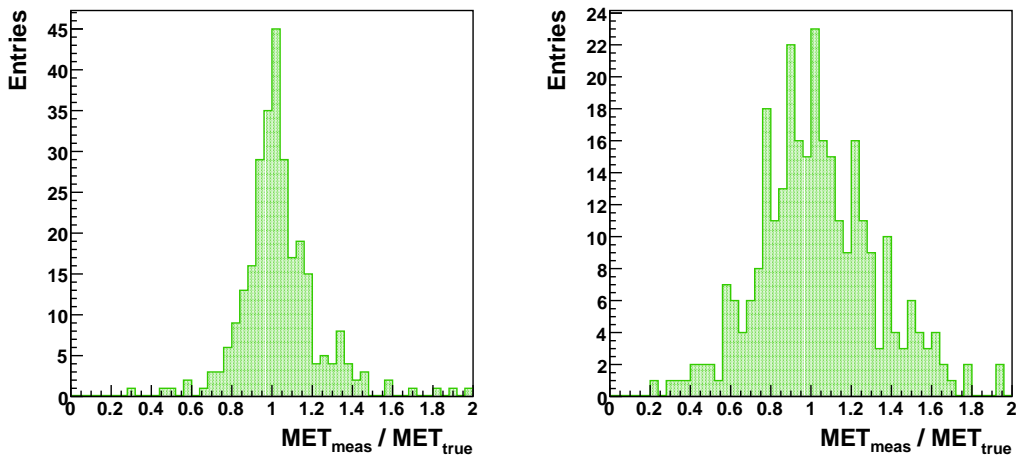


Figure 7.13.: Ratio of generated and measured missing transverse energy in Toy MC signal events. Left: sum of all visible particles. Right: smearing of invisible momenta with the experimental missing E_T resolution.

Using the idealized Toy MC instead of the detector simulation the extremum in a scan of $\tilde{q}_L \tilde{q}_L$ events becomes narrower and more pronounced in $m_{\tilde{\chi}_1^0}$ due to the mentioned differ-

ences (Fig. 7.14, top). Comparing scan results for the actual jet resolution and for a setup with a 50% increase (Fig. 7.14, middle) shows that the power of the LSP mass constraint is strongly dependent on the jet measurement precision, while the other masses are less affected, although their distributions broaden slightly.

The same is observed for a degraded missing E_T resolution, which again negatively influences the shape in the LSP mass variable (Fig. 7.14, bottom).

In both cases of a worse jet resolution and a worse missing E_T resolution the tail towards small slepton masses is enhanced and the distribution broadens very slightly. The effect blurs the maximum originally found close to the true masses so strongly, that only an upper limit can be set on the $\tilde{\chi}_1^0$ mass. We conclude that measurement resolutions are a crucial factor in the mass determination and a minimal precision has to be given for a successful application.

7.4.3 Further Signal and Background Contributions

In the discussion of the event selection several categories of signal events were introduced (cf. Sec. 5.2.2) and their behaviour in the mass scan is studied.

The two reasons for the classification are that either a squark of the signal cascade is not directly produced in the hard interaction but comes from a gluino decay, or that the squark is not one of the (almost) mass degenerate \tilde{u}_L , \tilde{c}_L , \tilde{d}_L or \tilde{s}_L .

Beside the shape of the likelihood contour, which allows a comparison among mass hypotheses, information on the overall compatibility is also provided by the average χ^2/ndf per fitted event (Tab. 7.5). This quantity facilitates the comparison among the event categories,

Category	N_{evts}	$\sum \chi^2/\text{ndf}/N_{\text{evts}}$
$\tilde{q}_L\tilde{q}_L$	117	0.75
$\tilde{g} \rightarrow \tilde{q}_L$	65	0.80
\tilde{b}_1 (incl. \tilde{g} decays)	126	0.84
\tilde{b}_2, \tilde{q}_R (incl. \tilde{g} decays)	26	0.84
All Signal Processes	334	0.85
Background	367	1.07

Table 7.5.: Average χ^2 at optimum of mass scan for including only events of the current category.

each of them containing a different number of events and therefore yielding a different best likelihood value by construction. The values hardly differ among signal categories but a slight increase is observed when including \tilde{g} decays. Peculiarities of individual event classes are discussed in the following.

Gluino Decays

Including events in which one or both \tilde{q}_L are produced in gluino decays yields a similar result as before. However in our sample the tail towards small LSP masses becomes more prominent. The average jet multiplicity is higher than in $\tilde{q}_L\tilde{q}_L$ events because the gluino decay yields an additional jet. This implicates an increased uncertainty on the total transverse momentum balance and hence a worse LSP mass constraint as discussed before.

Right-handed Squarks and Heavier Sbottom

The event sample contains some events with squarks of the nearly mass degenerate \tilde{q}_R or \tilde{b}_2 squarks ($M = 546 \text{ GeV}$). Since only 7 events with squark pair production and 19 with a gluino decay are counted their likelihood distribution shows a very broad extremum that is not sharp enough to reveal new features.

Due to the small number of events and the small mass difference $M_{\tilde{q}_L} - M_{\tilde{q}_R/\tilde{b}_2} = 15 \text{ GeV}$ no second extremum is observed in a combined \tilde{q}_L and \tilde{q}_R/\tilde{b}_2 sample, which in general shows the same properties as discussed for the pure \tilde{q}_L case. The best average χ^2 value also does not change significantly when including these slightly lighter squarks.

Light Sbottom

As expected, the likelihood distribution for a sample containing only events with the lightest squark (\tilde{b}_1 , $M = 517 \text{ GeV}$) is similar to the \tilde{q}_L case with the difference, that the extremum is located at the correct lower squark mass (Fig. 7.15).

Due to the large number of \tilde{b}_1 events (126), making up one third of signal events, and the large mass gap of almost 50 GeV with respect to the left-handed squarks, the two extrema are visible also in the inclusive signal sample (cf. Fig. 7.16).

Overall Signal Contribution

Adding the distributions of all types of squarks two separate maxima for heavier and lighter types can be identified in the 2-dimensional projection (Fig. 7.16, top). However, due to the correlations, the extremum coming from \tilde{b}_1 is shifted towards smaller neutralino and slepton masses in this inclusive signal sample.

Small LSP masses fit very well in these combined distributions and it may not be possible to set a lower limit on its mass. However, from the above observations the true LSP mass is expected to be located close to the edge at higher values where the likelihood falls steeply.

Interestingly, the same feature was observed in another mass determination study [83] in which the same cascade is considered, starting from the $\tilde{\chi}_2^0$. The authors construct a system of equations with an equal number of constraints and unknown LSP momenta, using hypotheses for the three involved masses. Mass points for which analytic solutions can be found lie in a three dimensional region, which for the LSP mass reaches from the true mass value down to zero.

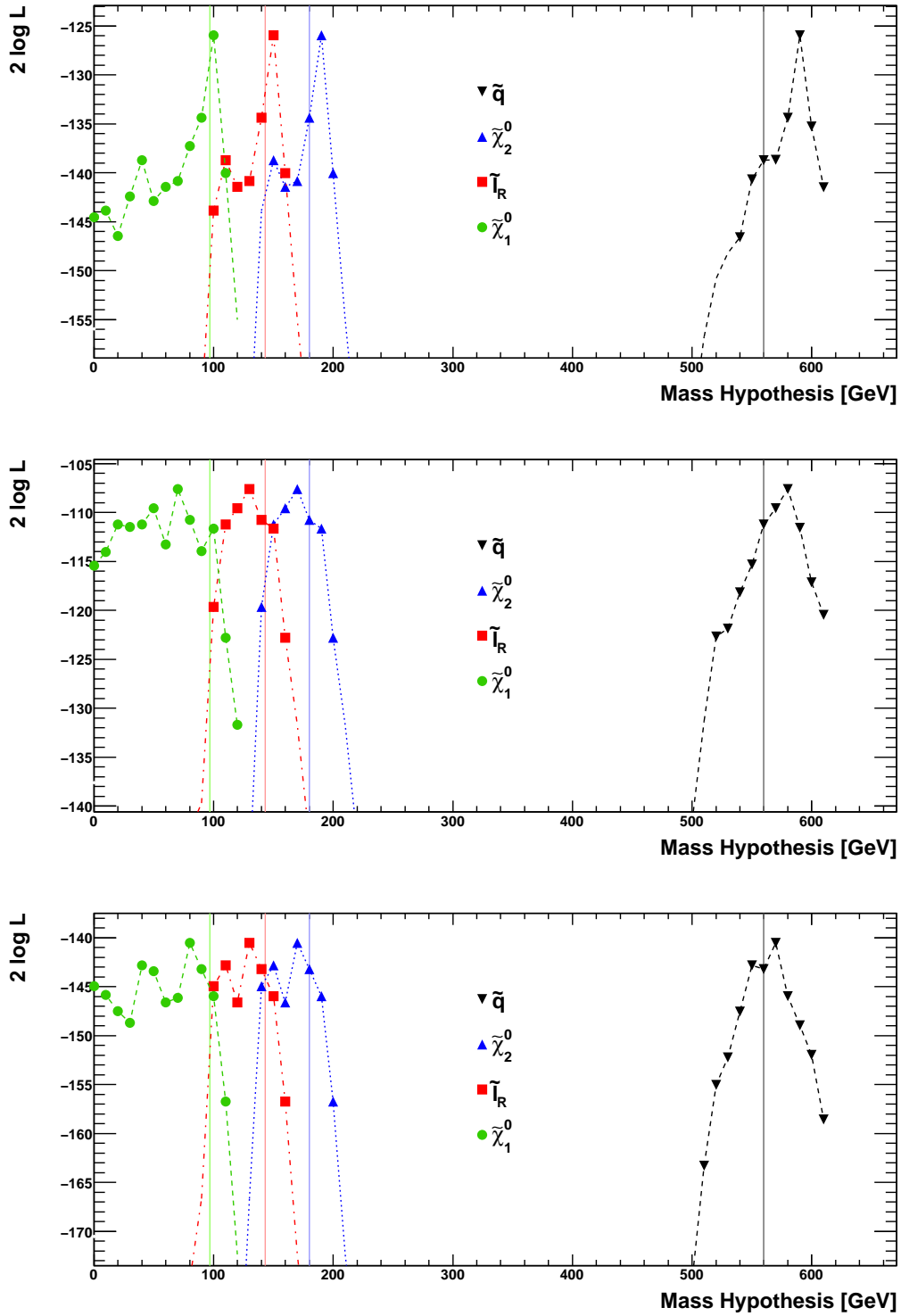


Figure 7.14.: Projections of the Toy MC mass scan on $\tilde{q}_L\tilde{q}_L$ signal events into 1-dimension for each of the four masses. Top: Standard Toy MC setup. Middle: jet p_T resolution worsened by a factor of 1.5. Bottom: Simulation of missing E_T by taking the true value and smearing it with experimental resolution.

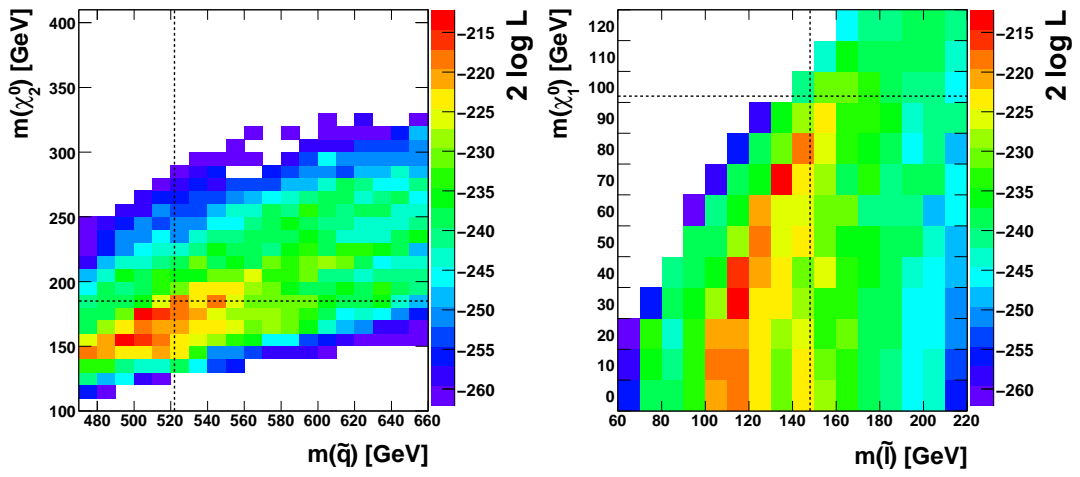


Figure 7.15.: Projections of mass scan for signal events containing a \tilde{b}_1 in detector simulation sample with full combinatorics. True values of SUSY masses are indicated by black dashed lines.

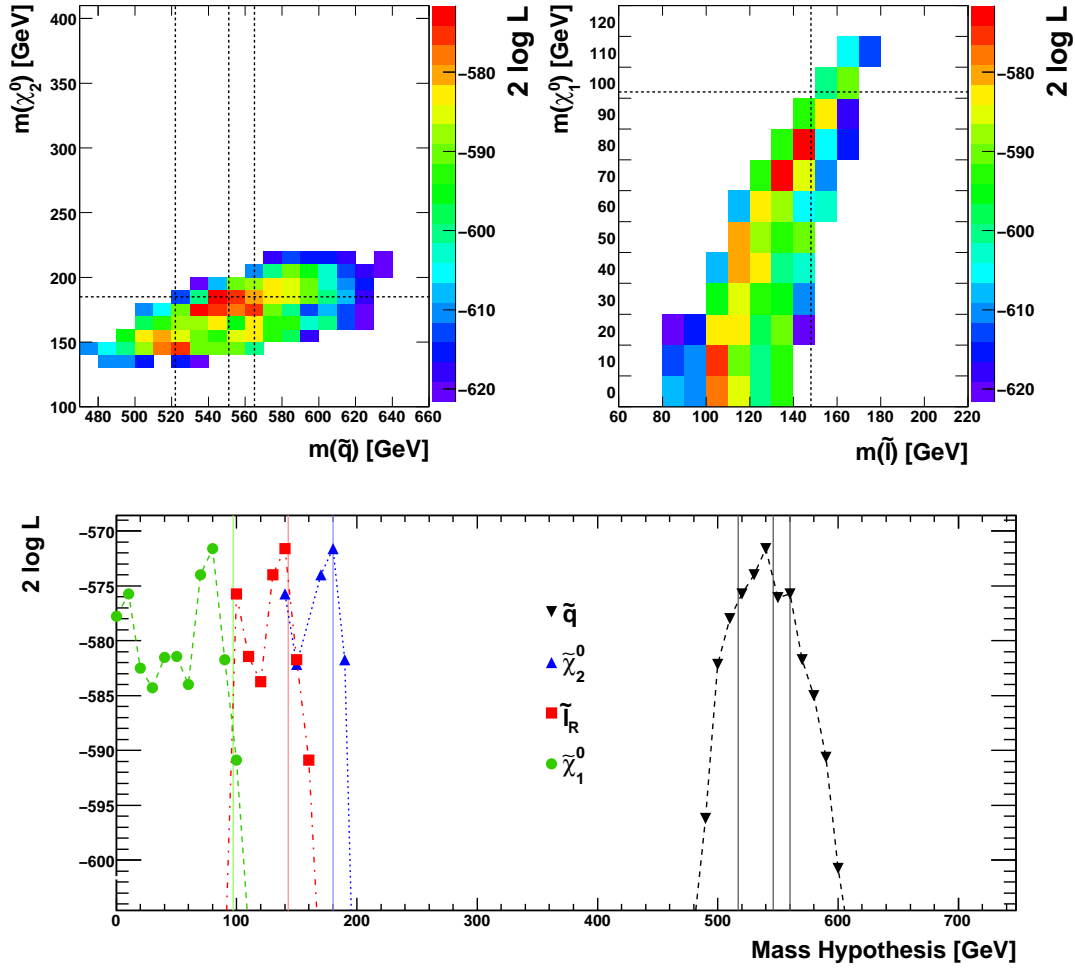


Figure 7.16.: Projections of the mass scan for all signal events in detector simulation sample with full combinatorics. Top: 2-dimensional mass planes. True values of SUSY masses are indicated by black dashed lines. All three squark types (\tilde{q}_L , \tilde{q}_R/\tilde{b}_2 , \tilde{b}_1) contribute. Bottom: 1-dimensional likelihood projection for all four masses (\tilde{q} , $\tilde{\chi}_2^0$, \tilde{l} , $\tilde{\chi}_1^0$).

SUSY Background Effects

All processes at SPS1a which are not contained in the signal categories Tab. 7.5 constitute the SUSY background (cf. Tab. 5.9). The best fitting mass values for the combination of all background events lie close to a zero LSP mass and at higher squark masses, well above the true value (Fig. 7.17, left). Small values for the LSP are preferred since this

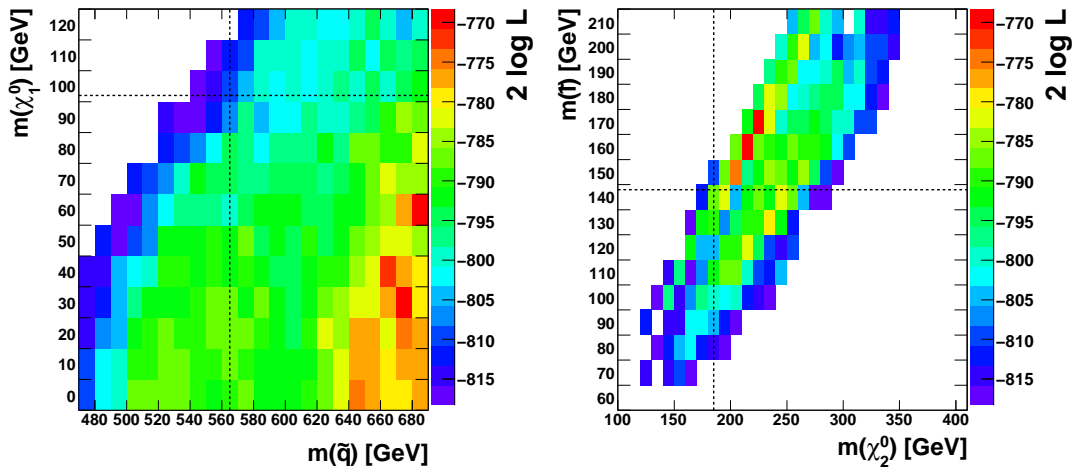


Figure 7.17.: Projections of the mass scan for background events in detector simulation sample. True values of signal cascade masses are indicated by black dashed lines.

leaves more freedom in the adjustment of its momentum components in the fit, where of course the assumed event topology does not match the actual decay chain. High squark masses appear to be an effect of arbitrary jets being combined with a lepton pair and LSP, often coming from a leptonic part of the decay chain which is identical to signal events (cf. Sec. 5.2.2).

In the $m_{\tilde{\chi}_2^0}$ and $m_{\tilde{l}_R}$ plane two bands are visible (Fig. 7.17, right). The upper one stretches along the true mass difference and comes from events having the correct lower part of the decay chain ($\tilde{\chi}_2^0 \rightarrow \tilde{l} \rightarrow \tilde{\chi}_1^0$) on one or even both of their decay branches. A broad second extremum is found at a larger neutralino-slepton mass difference. Events not containing branches with the correct lower part of the decay chain contribute, especially those with a $\tilde{\tau}$ instead of smuon or selectron.

The overlay of both distributions leads to the observed structure. The average χ^2 at the best mass hypothesis is larger than for signal events (cf. Tab. 7.5). Increasing the number of events (integrated luminosity) does not significantly change the observed likelihood distribution.

Full Event Sample

In the full event sample the background dominates and strongly distorts the likelihood distribution (Fig. 7.18). Several maxima emerge due to contributions from left-handed squarks, light sbottoms and the background, which prefers larger squark masses. Overall, the best squark mass hypotheses still lie close to the true \tilde{q} mass but $\tilde{\chi}_2^0$ and \tilde{l}_R masses show a second extremum at relatively low values. The LSP mass cannot be constrained from below and a zero mass appears to be compatible.

A determination of all masses with the present signal to background ratio of ~ 0.91 is not feasible, although the heavier particles in the chain are still reasonably met. A reduction of the background contribution is necessary for a precise measurement and beside a further event selection, one option is the inclusion of a dilepton mass edge measurement.

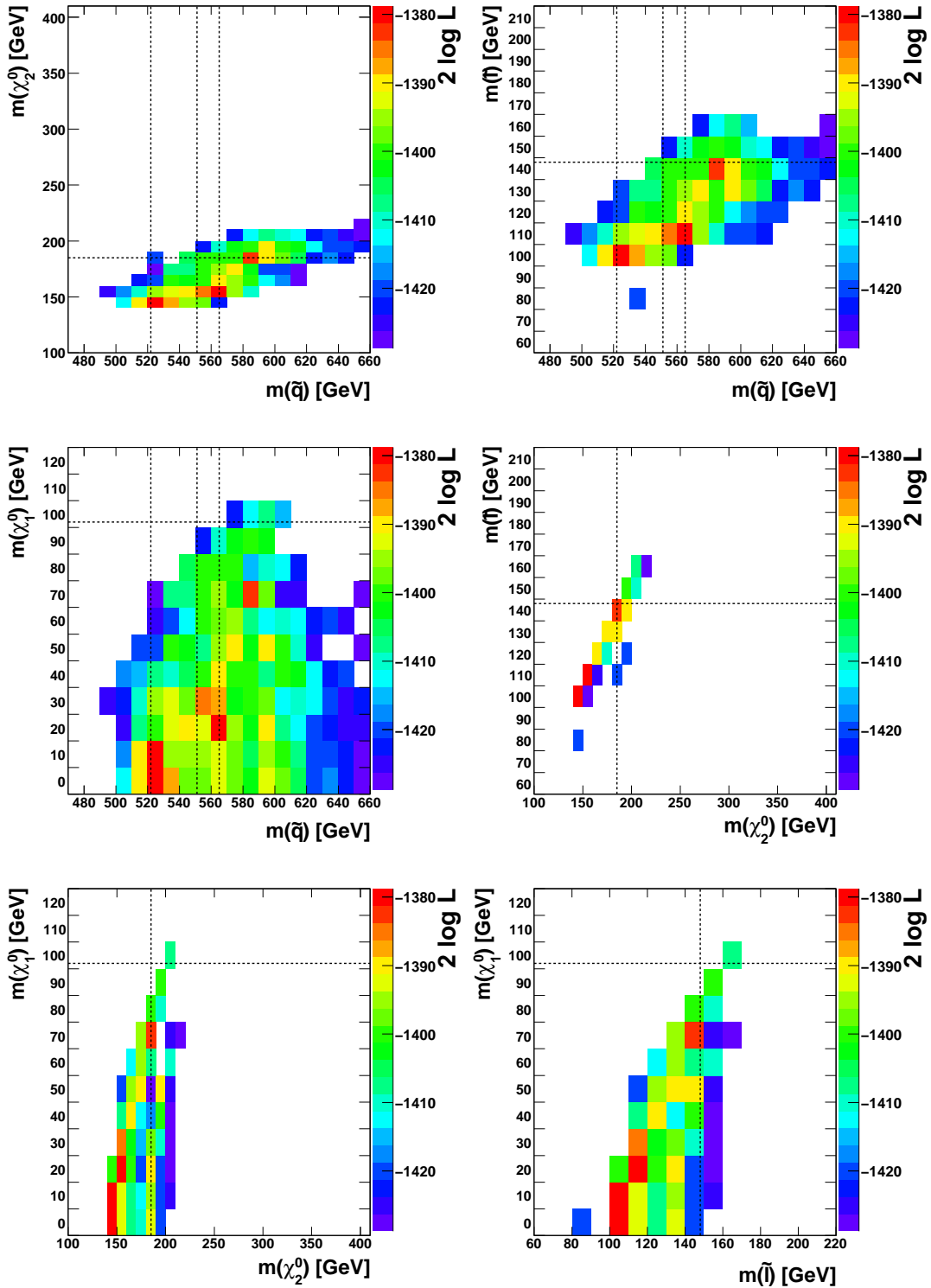


Figure 7.18.: Projections of the mass scan for signal and background events in detector simulation sample with full combinatorics. True values of signal cascade masses are indicated by black dashed lines.

7.5 Inclusion of the Dilepton Mass Edge

One of the best studied approaches to mass determination is the method of kinematic endpoints (cf. Sec. 4.2). The measurement of the dilepton mass edge was studied in detail elsewhere and for low mass mSUGRA scenarios it becomes visible with rather little integrated luminosity at the LHC. Certainly a measurement of the endpoint will be available early if it exists.

As pointed out above, the kinematic edge has a large impact on the shape of the likelihood contour. However, also hypotheses which are not compatible with the exact kinematic endpoint are fitted with good likelihood mainly due to the discussed resolution effects.

The inclusion of a measured endpoint for the dilepton invariant mass will increase the power of the fit by reducing the dimensionality of the mass space and excluding certain mass combinations. Having the relation Eq. 7.4 between the three masses of $\tilde{\chi}_2^0$, \tilde{l}_R and $\tilde{\chi}_1^0$, the measurement of m_{ll}^{max} allows the substitution of one of the mass variables, e.g. $m_{\tilde{\chi}_2^0}$, which is then given by the expression

$$m_{\tilde{\chi}_2^0}^2 = m_{\tilde{l}_R}^2 \cdot \left(1 + \frac{(m_{ll}^{max})^2}{(m_{\tilde{l}_R}^2 - m_{\tilde{\chi}_1^0}^2)} \right). \quad (7.5)$$

In a scan of all categories of signal events, where for each combination of slepton and LSP mass only the $m_{\tilde{\chi}_2^0}$ value fulfilling Eq. 7.5 is considered, the distribution in the slepton-LSP plane is reduced to a narrow, curved band (Fig. 7.19, top). The result is expected because still the hypotheses close to the true $\tilde{\chi}_2^0$ - \tilde{l}_R mass difference yield the best fits, but by enforcing the mass edge relation only hypotheses on the observed band are compatible to these preferred $\tilde{\chi}_2^0/\tilde{l}_R$ values.

The determination of the LSP mass is improved because the masses competing with the true value were all lying slightly below this band (cf. lower right plot Fig 7.9). The squark mass extremum becomes narrower, is stretched due to the \tilde{b}_1 contribution and stronger correlated to the slepton mass. The best hypothesis has an average χ^2/ndf per event of 0.91, which is slightly larger than in the scans without a mass edge measurement because now certain mass combinations are excluded.

Projecting the likelihood into one dimension a clear peak is visible for each of the four masses (Fig. 7.19). In order to estimate the precision of the measurement the likelihood contour is interpreted in terms of confidence intervals for a joint estimation of the four masses (cf. Tab. 7.3).

The distance between the scan points is rather large compared to the width of the maxima for the three lighter particles. Therefore, a parabola is determined such, that it fits the point of best likelihood and the two neighboring points, since in principle the log-likelihood should have a parabolic shape in the vicinity of the extremum. The 1σ interval, corresponding to a decrease of the parabola by 4.72 with respect to the peak, is determined

and taken as an estimate of the statistic uncertainty of the mass determination.

The squark mass peak is strongly asymmetric and a parabola does not resemble its shape. Therefore, the 1σ interval is approximated by taking the point at which the connecting line between the scan points reaches the desired distance of $\Delta(2 \ln L) = 4.72$ to the maximum. Incidentally this happens very close to actual scan points. Results are summarized in Tab. 7.6.

As mentioned before, various effects may cause the true statistical uncertainty to deviate from the value obtained in this procedure and the result should be treated carefully. Nevertheless this estimate gives a hint at the precision which is reachable with this mass determination method.

	Scan Result [GeV]	MC value [GeV]
$M_{\tilde{q}}$	560^{+10}_{-20}	562/568
$M_{\tilde{\chi}_2^0}$	175 ± 5	180
$M_{\tilde{l}}$	140 ± 5	143
$M_{\tilde{\chi}_1^0}$	90 ± 5	97

Table 7.6.: Result of the mass determination method including the mass edge measurement for all signal events with full combinatorics. Uncertainties are estimated from the 1σ likelihood intervals.

An inclusion of SUSY background events alters the distribution and leads to a separate second extremum around the light sbottom mass (Fig. 7.20, top). Due to the ridge structure of the likelihood contour in the \tilde{l} - $\tilde{\chi}_1^0$ mass plane this second extremum is found at a slepton mass of only 115 GeV and consequently a too low LSP mass (60 GeV).

In the 1-dimensional projections of the likelihood distribution the double peak structure is even better visible (Fig. 7.20, bottom). Interpreting the observation in terms of confidence intervals as before, disconnected 1σ regions are obtained for the two maxima in $\tilde{\chi}_2^0$, \tilde{l} and $\tilde{\chi}_1^0$, whereas the two maxima in the squark mass are less separated.

While in principle the visibility of a second squark mass peak nicely demonstrates the precision of the method, it might be difficult to tell from real data which of the extrema is the correct one for any of the other three masses.

In summary, we find that by the inclusion of the mass edge information the intrinsic weakness of the kinematic fits method concerning the restriction of the LSP mass is cured, and a determination of all four involved masses is possible, if backgrounds are not too large.

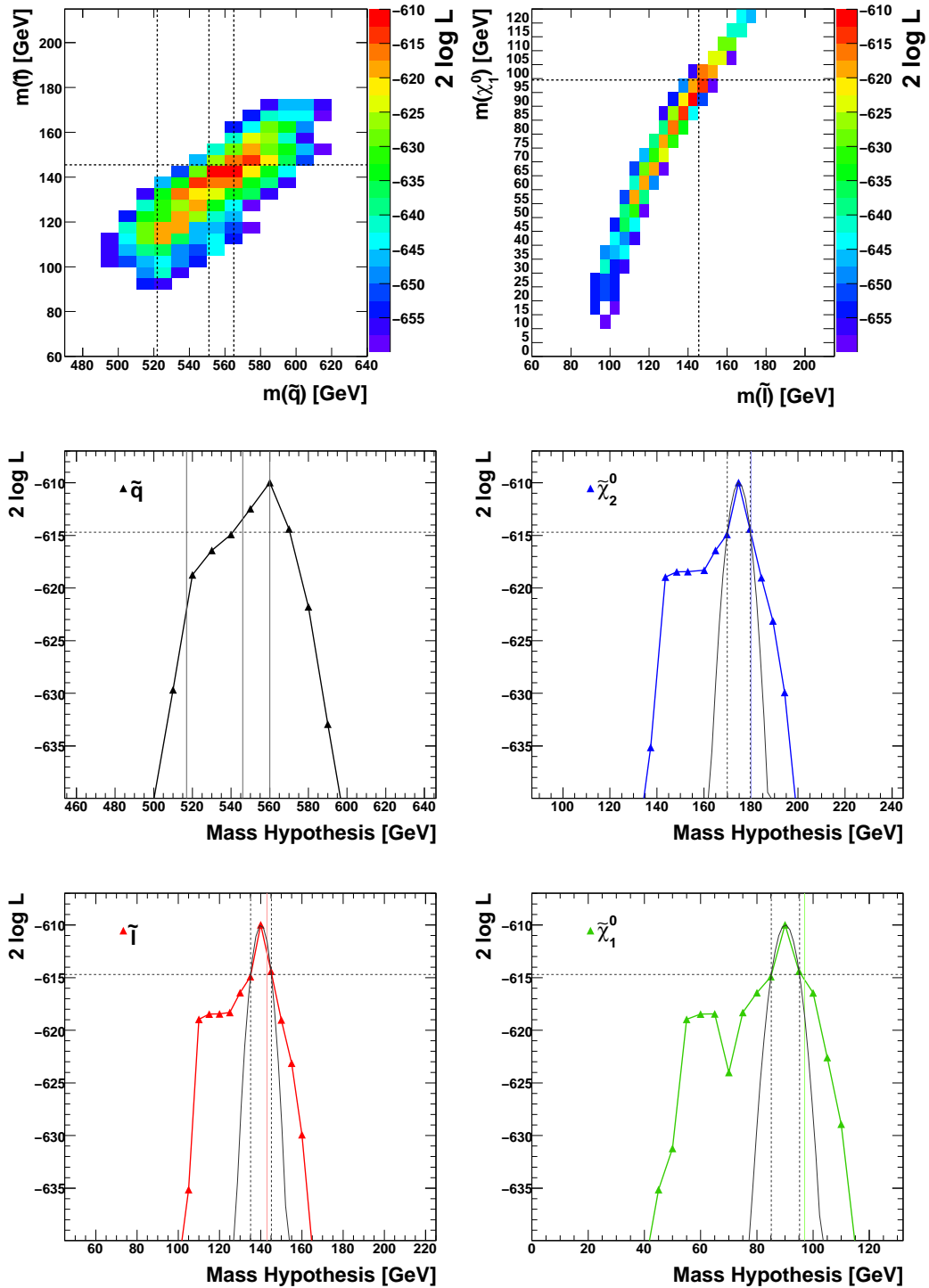


Figure 7.19.: Projections of the mass scan for all signal events in detector simulation sample with full combinatorics and a perfectly fulfilled mass edge (Eq. 7.5). Top: 2-dimensional projections. True values of SUSY masses are indicated by gray dashed lines. Middle and bottom: 1-dimensional projections and adjusted parabola. True masses are indicated by vertical colored lines. The 1σ uncertainty interval is indicated by gray vertical and horizontal lines.

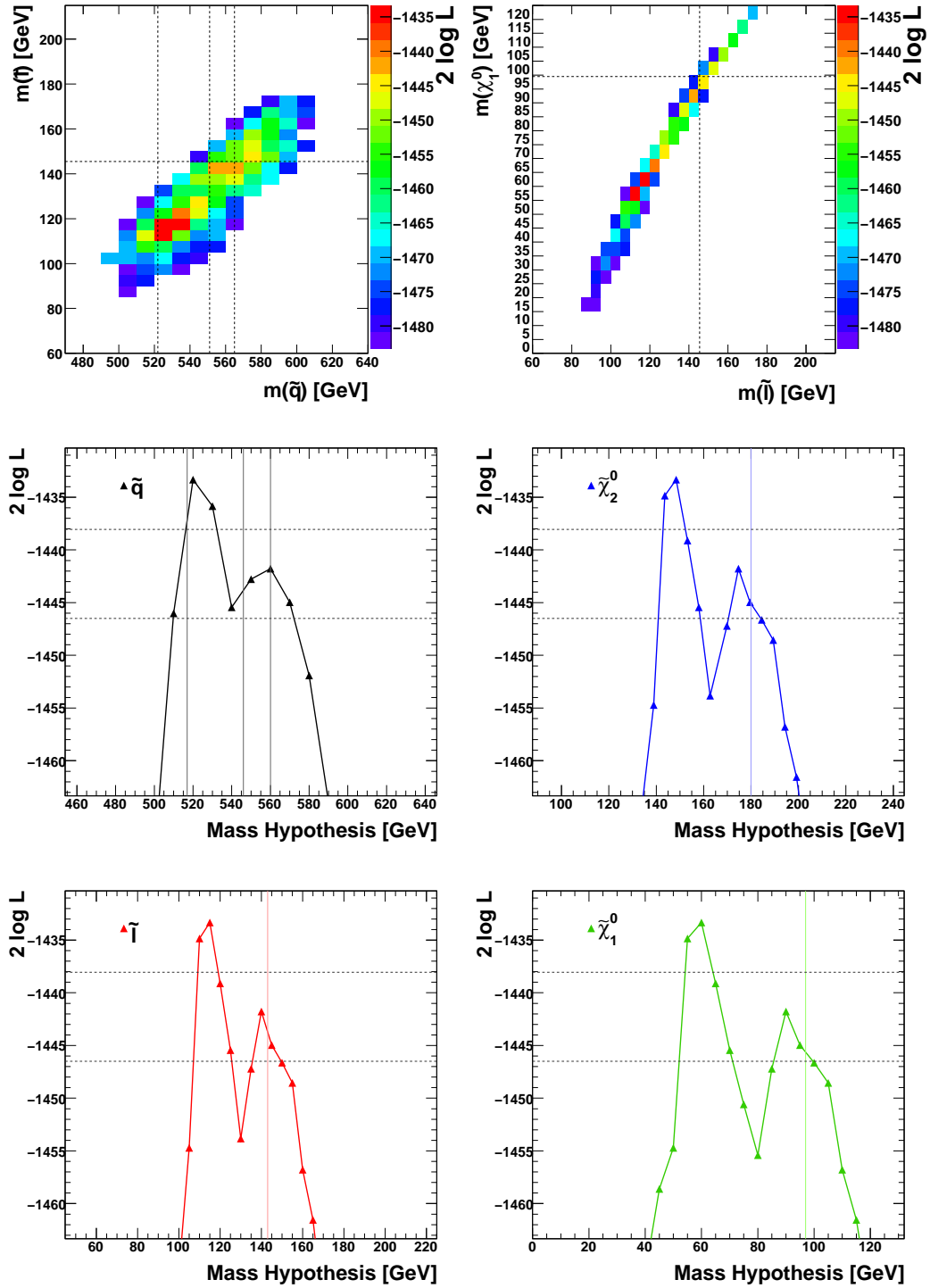


Figure 7.20.: Projections of the mass scan for signal and background events in detector simulation sample with full combinatorics and a perfectly fulfilled mass edge (Eq. 7.5). Top: 2-dimensional projections. True values of SUSY masses are indicated by black dashed lines. Middle and bottom: 1-dimensional projections for all four masses. True masses are indicated by vertical colored lines. The likelihood corresponding to a 1σ uncertainty interval is indicated for both maxima by gray horizontal lines.

7.6 Comparison to Other Studies

In several publications dealing with SUSY mass determination the SPS1a was chosen as reference point, which allows a comparison of our results with the published studies. We focus here on two polynomial methods which have some aspects in common with the Kinematic Fits Method and were already introduced in Sec. 4.2.1: the ansatz by Webber [75], which also consists of a test of mass hypotheses and which was exploited for the calculation of the initial LSP momenta for our fit (cf. Sec. 6.2), and the numeric solution of the system of equations for pairs of events by Cheng et al. [74]. Both use exactly the same signal cascade.

Mass Hypothesis Method

In the publication by Webber only signal events are considered, including left-handed squarks from gluino decays but none from the third generation. Furthermore the leptons pairs are required to have different flavor, which minimizes combinatorics. The event treatment is an even more rudimental version of our Toy Monte Carlo and consists of a gaussian smearing of the final-state particle fourvectors and the true LSP momenta to obtain a missing E_T value. Different resolutions were studied by the authors and results applying a $\delta p/p = 5\%$ smearing to all particles and the missing E_T are shown in Fig. 7.21 and quoted in Tab. 7.7. They were obtained from a sample corresponding to an integrated luminosity of $L_{int} = 300 \text{ fb}^{-1}$.

	Mass Hypothesis Method [75]		Kinematic Fits Method	
	Determined Mass [GeV]	MC value [GeV]	Scan Result [GeV]	MC value [GeV]
\tilde{q}	539 ± 9	540	582 ± 8	562/568
$\tilde{\chi}_2^0$	178 ± 3	177	188 ± 5	180
\tilde{l}	144 ± 2	143	148 ± 5	143
$\tilde{\chi}_1^0$	96 ± 4	96	98 ± 5	97

Table 7.7.: Left columns: Result of the mass determination method [75] for a measurement resolution of $\delta p/p = 10\%$. Given are the mean and RMS from a set of 100 subsamples, each consisting of 25 events. Right columns: Result of mass scan on Toy MC sample.

In order to have a comparable setup for our method the Toy Monte Carlo scan on an event sample corresponding $L_{int} = 280 \text{ fb}^{-1}$ is chosen and only \tilde{q}_L events, including gluino decays, are considered. The resulting 1-dimensional likelihood projections (Fig. 7.21) show sharp peaks close to the true masses, although all masses except the LSP are slightly overestimated. The numerical result (Tab. 7.7) is obtained as before by adjusting a parabola through the maximum and its two neighboring points.

From our observations in Sec. 7.4.3 it can be suspected that the compared method also

profits from the use of a Toy MC with its stronger constraints on the LSP mass due to a well measured momentum balance (missing E_T) and fewer jets.

Therefore, a degradation in the LSP mass determination might occur in Webber's method when studying full detector simulation samples because more viable solutions with small LSP masses may be found. Actually, the plot of best mass values (Fig. 7.21) shows already some event samples with a best LSP mass close to zero and this effect might become stronger in a more realistic scenario.

Comparing results (Tab. 7.7) we find that the precision of the methods is of the same order of magnitude in case of an idealized Toy MC scenario. For a final evaluation the cited method would have to be tested with full detector simulation and including backgrounds.

Event Pair Method

The second result in our comparison is based on an ATLAS detector simulation for an SPS1a sample corresponding to $L_{int} = 300 \text{ fb}^{-1}$ [74]. The event selections are similar, despite the fact that a lower jet transverse momentum cut ($p_T > 100 \text{ GeV}$) is applied and b-tagging is used to exclude events containing b-jets. With a b-tagging efficiency around 50% for high p_T jets, the authors claim to reach a signal to background ratio of 2. The published mass determination result shows a good agreement with the generator level masses and very small statistical uncertainties (Tab. 7.8).

	Event Pair Method [74]		Kinematic Fits Method	
	Determined Mass [GeV]	MC value [GeV]	Scan Result [GeV]	MC value [GeV]
\tilde{q}	561.5 ± 4.1	564.8/570.8	567 ± 11	562/568
$\tilde{\chi}_2^0$	179.0 ± 3.0	180.3	174 ± 6	180
\tilde{l}	138.8 ± 2.8	142.5	139 ± 7	143
$\tilde{\chi}_1^0$	94.1 ± 2.8	97.4	89 ± 7	97

Table 7.8.: Results of the mass determination method [74] and a mass scan in a comparable setup (cf. Fig. 7.22).

In order to provide a basis for comparison our selection has to be adapted to exclude b-jets. A simple emulation of b-tagging is used in which events are kept only if a random number from a uniform distribution in the interval $(0, 1]$ lies below the probability not to identify a b-jet. This non-identification probability is calculated assuming a constant b-tag efficiency of 50% and counting b-partons on generator level with a transverse momentum of more than 20 GeV, i.e. Toy MC b-jets.

As expected the contribution of sbottom signal processes is reduced by about a factor of 4 (two b-jets per event) and also the background is further suppressed, yielding a signal to background ratio of about 1.1 (cf. Tab. 7.9).

	Original Selection	After b-tag emulation
$\tilde{q}_L \tilde{q}_L$	217	209
$\tilde{g} \rightarrow \tilde{q}_L$	132	132
\tilde{b}_1	216	50
\tilde{b}_2, \tilde{q}_R	54	26
Total Signal	619	417
Background	754	405
S/B	0.82	1.03

Table 7.9.: Event selection result for detector simulation (280 fb^{-1}) sample with b-tagging emulation. An b-tagging of efficiency of 50% was assumed.

Despite a very similar event selection, a $S/B = 2$ is by far not reached because the number of signal events is only 60% of the quoted value, while the background is about 15% larger. Most probably this is an effect of yet unidentified differences in e.g. lepton reconstruction, identification and isolation efficiencies. Therefore a further assimilation step is made and the background in our sample is artificially reduced by randomly discarding 50% of background events, yielding the desired S/B ratio.

Since the result Tab. 7.8 has very small statistical uncertainties, we only compare the Kinematic Fits Method with inclusion of the dileptonic mass edge measurement, in order to maximize its precision.

The numerical result of this scan (Fig. 7.22) closely resembles the true mass values. The estimated statistical uncertainties (Tab. 7.8) are at least twice as large as in the compared study.

We conclude that in case of an almost sbottom free sample with $S/B = 2$ our method performs very well, if use is made of the mass edge measurement. However, a finer mass scan and a precise estimate of the statistical uncertainties are necessary to find out whether the final precision can reach the excellent performance of the reference method. Furthermore systematic effects are to be considered for both methods.

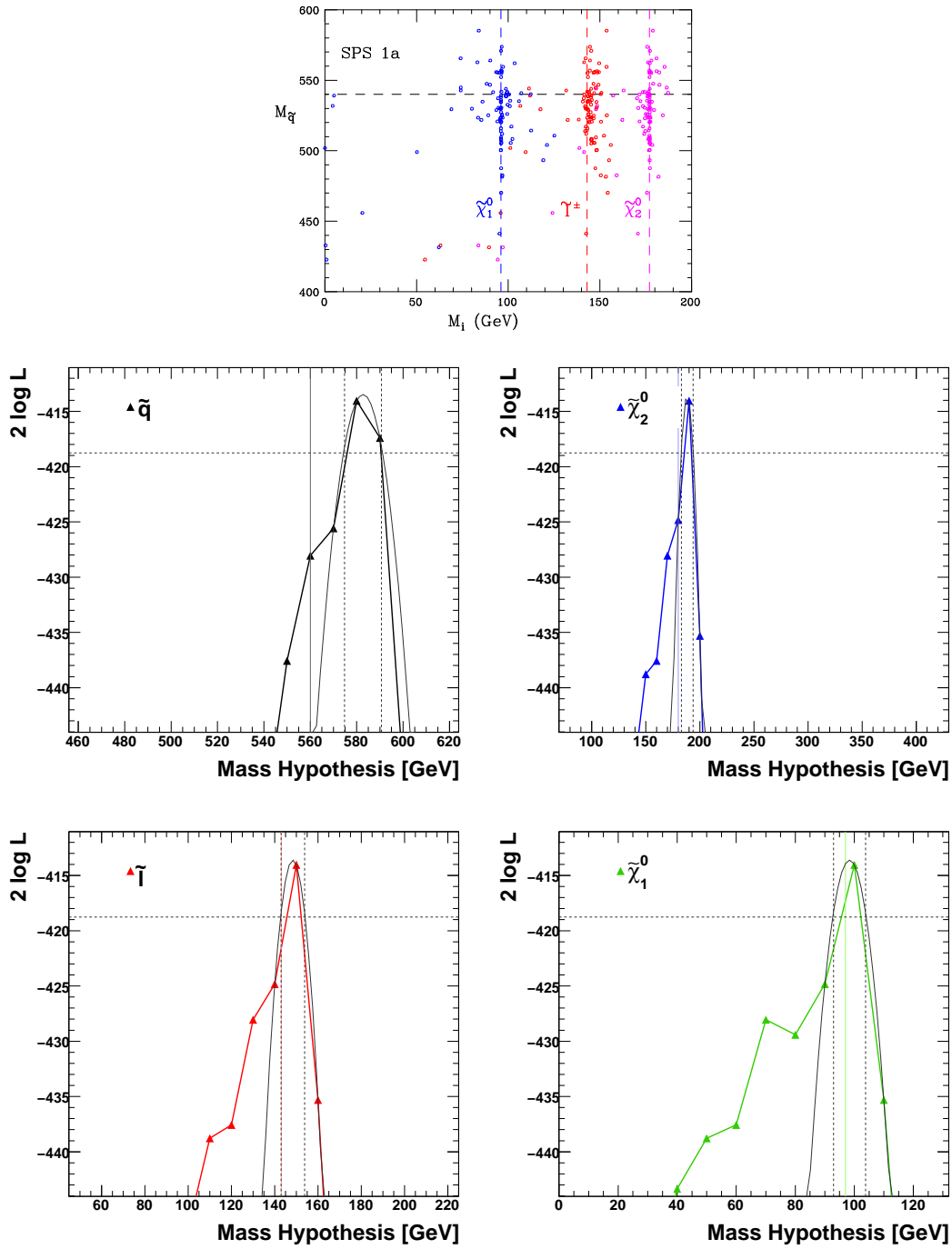


Figure 7.21.: Top: Distribution of best mass values for samples of 25 events [75]. Bottom: projection of likelihood for all scanned masses in Toy MC. Dashed lines indicate the 1σ uncertainty obtained from the parabola through the maximum and neighboring points. In both plots only signal events with left-handed squarks of the first and second generation are shown.

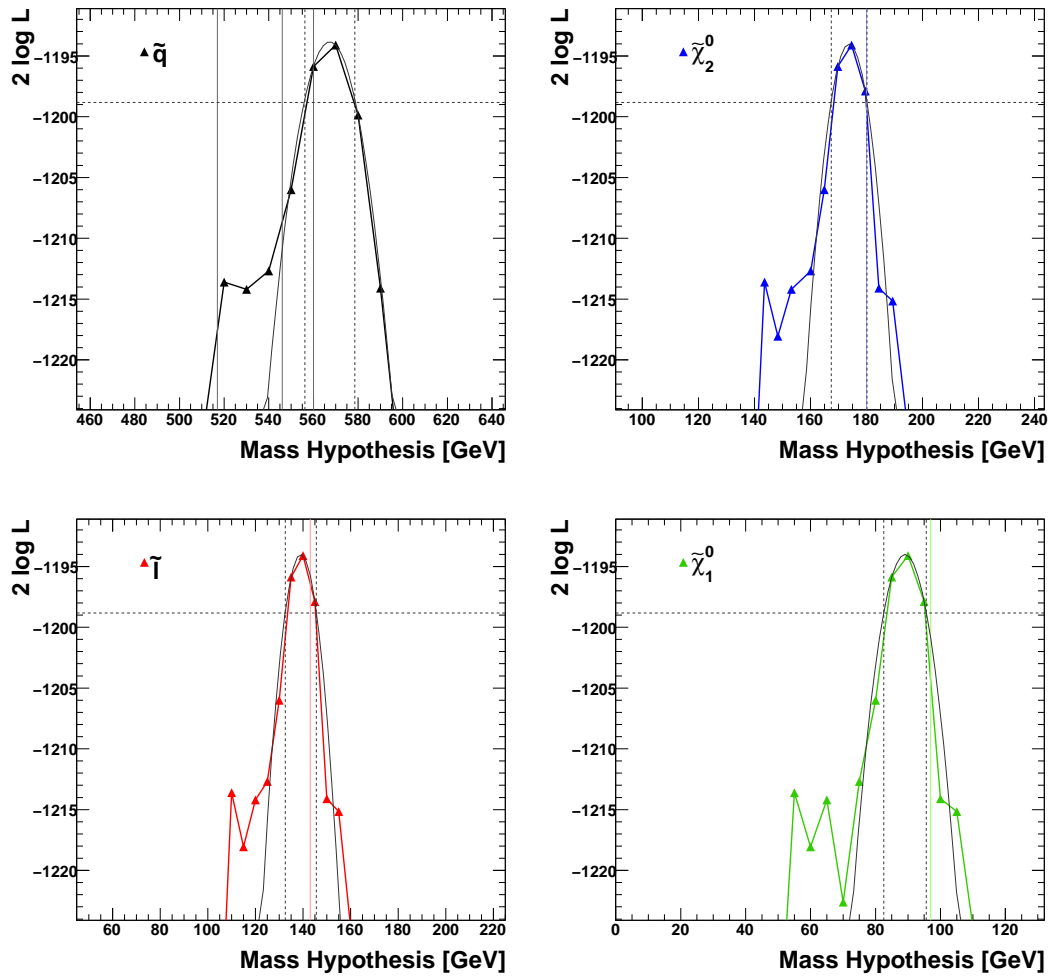


Figure 7.22.: Projection of scan result on detector simulation sample for signal and background, using dilepton mass edge, b-tag emulation and an artificial background suppression. Dashed lines indicate the 1σ uncertainty obtained from the parabola through the maximum and neighboring points.

7.7 Conclusions

The constrained kinematic fit of the signal cascade containing two unmeasured neutralinos works well if the SUSY masses are known and yields reasonable fit probability and pull distributions. Event reconstruction and resolution effects in detector simulation slightly degrade the performance with respect to the Toy MC. In most events the fit correctly finds the jet and lepton pair on the same branch but the association of leptons to their position on the branch is less successful due to their similar kinematics.

Combining the fit result of all events allows the definition of a likelihood variable for each tested set of masses and an exploration of the compatible masses via a scan. The obtained 4-dimensional likelihood can be projected into fewer dimensions for analysis.

In principle the mass determination method works and the scan yields the best likelihood values around the true particle masses if considering identical decay chains. The likelihood shape in dependence of the lower three masses in the decay chain is understood from lepton kinematics.

Constraining the mass of the lightest SUSY particle is challenging, since it is rather weakly restricted by the kinematics and the crucial p_T balance constraint is weakened by jet and missing E_T measurement resolutions. Improved measurements of the LSP mass are observed if jet or missing E_T resolution are assumed to improve.

Events containing light sbottom squarks yield a second extremum at an accordingly lower squark mass. In combination of all signal events this leads to smaller neutralino and slepton mass due to the shape of the added distributions. Therefore a sample containing only squarks of the same type is desirable for a precise measurement.

SUSY backgrounds at SPS1a dominate if considering the full event sample and have to be reduced further for a successful measurement.

Exploiting knowledge on the maximum invariant lepton mass from an endpoint measurement complements the method and reduces the dimensionality of the scan. It strengthens the determination of the LSP mass, improves the precision of the result, and reduces the influence of backgrounds.

In comparison to competing methods, the performance looks comparable at first sight but a proper evaluation of uncertainties is necessary to draw final conclusion.

Chapter 8

Summary

Mass determination of SUSY particles is an important step after a possible discovery of supersymmetry at the LHC and may contribute in a fit of observations to SUSY model predictions.

The main challenge in mass determination in R-parity conserving SUSY is the existence of two unmeasured particles in each event, which makes a full kinematic reconstruction difficult. The diversity of possible decay chains leads to large SUSY backgrounds and requires a powerful event selection if a single event topology has to be isolated for the measurement.

Several methods were proposed and studied in recent years. In this thesis a further method for determination of SUSY masses was introduced, which combines a scan over possible mass values with a rating by an event-by-event constrained kinematic fit on a set of topologically identical events.

In the kinematic fit a sufficient number of constraints have to be imposed to compensate for the six unknown LSP momentum components. This requires cascades to contain at least three intermediate states on each decay branch. If the particle masses are known the full event kinematics can be reconstructed in the over-constrained fit.

Studying the low mass mSUGRA reference point SPS1a a decay chain containing four leptons but only two jets is chosen as signal process, because it has small combinatorics, a clear signature and basically no Standard Model backgrounds.

An implementation of the methods of Lagrangian multipliers is used for the kinematic fit. Since the covariance matrix for all measured particles is needed, jet and lepton transverse momentum as well as angular resolutions are determined.

Several options for a generation of initial values of the LSP momenta were compared. In the chosen approach they are calculated from measured objects by solving a system of equations derived from the kinematic constraints. This way the starting point for the fit was shown to be already close to the true solution if the correct masses are assumed and the fit reliably finds a minimum despite the complex χ^2 landscape from linearized constraints and many fit parameters.

A successful application of the constrained kinematic fit on a SUSY event topology containing two unmeasured particles at SPS1a was shown and a good performance observed for the case that masses of intermediate particles are known. Unmeasured momenta were reliably reconstructed with good precision and the assignment of jets and leptons to their position in the cascade is correctly found for a large fraction of events, although similar kinematics make a distinction of leptons on the same branch difficult.

A scan on a grid of hypothetical mass values and the combination of fit results in a likelihood distribution allows the determination of particle masses in events with identical decay topology. The mass of the last and escaping particle in the cascade is least constrained in the fit and hypotheses below its true mass may be found with good likelihood. Jet and missing E_T measurement resolution play a crucial role in the determination of this lightest mass, since it is mainly constrained by the p_T balance in the event and the smaller the measurement uncertainties the more precise the mass determination. The shape of the likelihood for the lower three masses and their correlations is determined by the lepton kinematics and is consistent with the well-known dilepton mass edge. The mass of lighter third generation squarks could be resolved in the tested setup.

Standard Model contributions are negligible but SUSY backgrounds at the SPS1a are large, especially cascades including a $\tilde{\tau}$ or stop squarks, since the branching ratios are rather unfortunate for a four lepton (i.e. electron/muon) topology.

The inclusion of a dilepton mass edge measurement strengthens the constraints on the LSP mass and increases the power of the method. A precise measurement of all masses in the decay chain seems possible if backgrounds can be kept small. The actual precision is yet to be evaluated with a finer scanning and an estimation of statistical and systematic uncertainties.

The method performs well in comparison to other mass determination methods using Toy Monte Carlo and even in the detector simulation case, if including the dilepton endpoint information and assuming a reduced background.

In summary, the kinematic fits method was shown to work in principle but reveals some interesting and not necessarily expected features. One distinguishing characteristic with respect to other methods is the inclusion of experimental uncertainties (jet/lepton resolutions) in the mass determination. Unfortunately the impact of these resolutions is large and their size turned out to be a crucial factor in the measurement. The underlying reason was identified to be the constraint on the LSP mass, which had to be improved by the inclusion of the dilepton mass edge measurement. Another drawback is the susceptibility to background from other SUSY cascades.

8.1 Outlook

Several possibilities exist to improve and extend the kinematic fit method. A first possible improvement for the studied scenario is the further reduction of SUSY backgrounds, e.g. by using tau-tagging in order to eliminate $\tilde{\tau}$ decays and b-tagging to reduce \tilde{t} and \tilde{b} contributions.

On the other hand the $\tilde{\chi}_2^0$ decay via a τ could also be included in the signal, despite the difficulties in tau reconstruction.

Variables like the angle between decay products in the rest-frame of the decaying particle could be used to improve the treatment of combinatorics by weighting combinations with their likelihood to yield the observed angle [76].

A large data set and smaller step size in the mass scan is necessary to evaluate the masses with full precision. However, the number of mass hypothesis grows quickly with a fixed grid in four dimensions. A more clever way to cover the relevant sections of the mass space and keep CPU consumption reasonable would be desirable.

From a more general point of view it may be interesting to extend the fit to a variety of decay topologies and test each event not only for its masses but also for its compatibility with each of the different decay chains.

Appendix A

Linearization and Iterative Solution in the Kinematic Fit

The algorithm for an iterative solution of the fit problem Sec. 6.1 is described [86] [87]. Using the same conventions as in Sec. 6.1 the n measured parameters are labelled \vec{y} and have a covariance matrix \mathbf{V} . The vector of residuals of the measured parameters w.r.t. their optimized values \vec{y}' are $\Delta\vec{y} = \vec{y}' - \vec{y}$. The squared sum of residuals can be expressed as

$$S(\vec{y}) = \Delta\vec{y}^T \mathbf{V}^{-1} \Delta\vec{y}.$$

The m unmeasured parameters are denoted by \vec{a} and each of the l constraints f_k is a function of the measured as well as the unmeasured parameters and can be written as an equality equation

$$f_i = f_i(\vec{y}, \vec{a}) \stackrel{!}{=} 0.$$

Introducing the Lagrange Multipliers λ the extremum of

$$L(\vec{y}, \vec{a}, \vec{\lambda}) = S(\vec{y}) + 2 \cdot \sum_{k=1}^l \lambda_k f_k(\vec{y}, \vec{a})$$

has to be determined. In the case of linear constraints the differentiation of L leads to linear equation for the optimal values of measured (\vec{y}') and unmeasured parameters (\vec{a}'). Otherwise a linearization of the constraints is necessary and the extremum can only be determined iteratively. In addition to the start values of the parameters (\vec{y}/\vec{a}) and their current optimized values (\vec{y}'/\vec{a}') also their values after the previous iteration (\vec{y}^*/\vec{a}^*) appear in the approximation

$$f_k(\vec{y}', \vec{a}') \approx f_k(\vec{y}^*, \vec{a}^*) + \sum_{i=1}^n \frac{\partial f_k}{\partial y_i} (\Delta y_i - \Delta y_i^*) + \sum_{j=1}^m \frac{\partial f_k}{\partial a_j} (\Delta a_j - \Delta a_j^*) \approx 0, \quad (\text{A.1})$$

where $\Delta\vec{y}^* = \vec{y}^* - \vec{y}$ and $\Delta\vec{a}^* = \vec{a}^* - \vec{a}$ denote the residuals after the previous iteration.

This equation can be rewritten in vector notation,

$$\vec{f}^* + \mathbf{B}(\Delta\vec{y}_i - \Delta\vec{y}_i^*) + \mathbf{A}(\Delta\vec{a}_j - \Delta\vec{a}_j^*) \approx 0 \quad (\text{A.2})$$

introducing the matrices of first derivatives for measured and unmeasured parameters (\mathbf{B} , \mathbf{A}), with components

$$(B)_{ki} = \frac{\partial f_k}{\partial y_i} \quad (\text{A.3})$$

$$(A)_{kj} = \frac{\partial f_k}{\partial a_j} \quad (\text{A.4})$$

Separating the terms which depend only on the values of the last iteration the constraint becomes

$$\mathbf{B}\Delta\vec{y} + \mathbf{A}\Delta\vec{a} - \vec{c} = 0 \quad \text{with} \quad \vec{c} = \mathbf{B}\Delta\vec{y}^* + \mathbf{A}\Delta\vec{a}^* - \vec{f}^* \quad (\text{A.5})$$

and the expression to be minimized reads

$$L = \Delta\vec{y}^T \mathbf{V}^{-1} \Delta\vec{y} + 2\vec{\lambda}^T (\mathbf{B}\Delta\vec{y} + \mathbf{A}\Delta\vec{a} - \vec{c}). \quad (\text{A.6})$$

After this linearization the differentiation w.r.t. \vec{y} , \vec{a} and $\vec{\lambda}$ can be carried out, yielding $n+m+l$ equations:

$$\mathbf{V}^{-1} \Delta\vec{y} + \mathbf{B}^T \vec{\lambda} = 0 \quad (\text{A.7})$$

$$\mathbf{A}^T \vec{\lambda} = 0 \quad (\text{A.8})$$

$$\mathbf{B}\Delta\vec{y} + \mathbf{A}\Delta\vec{a} = \vec{c}. \quad (\text{A.9})$$

These conditions can be expressed in matrix notation

$$\begin{pmatrix} \mathbf{V}^{-1} & 0 & \mathbf{B}^T \\ 0 & 0 & \mathbf{A}^T \\ \mathbf{B} & \mathbf{A} & 0 \end{pmatrix} \begin{pmatrix} \Delta\vec{y} \\ \Delta\vec{a} \\ \vec{\lambda} \end{pmatrix} = \begin{pmatrix} 0 \\ 0 \\ \vec{c} \end{pmatrix}. \quad (\text{A.10})$$

Since the matrix consists of several blocks of entries a procedure for the inversion of such partitioned matrices can be applied. The inverse matrix is written with the same partitions

$$\begin{pmatrix} \mathbf{V}^{-1} & 0 & \mathbf{B}^T \\ 0 & 0 & \mathbf{A}^T \\ \mathbf{B} & \mathbf{A} & 0 \end{pmatrix}^{-1} = \begin{pmatrix} C_{11} & C_{21}^T & C_{31}^T \\ C_{21} & C_{22} & C_{32}^T \\ C_{31} & C_{32} & C_{33} \end{pmatrix}. \quad (\text{A.11})$$

Using the abbreviations $\mathbf{V}_B = (\mathbf{B}\mathbf{V}\mathbf{B}^T)^{-1}$ and $\mathbf{V}_A = (\mathbf{A}^T \mathbf{V}_B \mathbf{A})$ the submatrices of the

inverse are given as

$$C_{11} = \mathbf{V} - \mathbf{V}\mathbf{B}^T\mathbf{V}_B\mathbf{B}\mathbf{V} + \mathbf{V}\mathbf{B}^T\mathbf{V}_B\mathbf{A}\mathbf{V}_A^{-1}\mathbf{A}^T\mathbf{V}_B\mathbf{B}\mathbf{V} \quad (\text{A.12})$$

$$C_{21} = -\mathbf{V}_A^{-1}\mathbf{A}^T\mathbf{V}_B\mathbf{B}\mathbf{V} \quad (\text{A.13})$$

$$C_{22} = \mathbf{V}_A^{-1} \quad (\text{A.14})$$

$$C_{31} = \mathbf{V}_B\mathbf{B}\mathbf{V} - \mathbf{V}_B\mathbf{A}\mathbf{V}_A^{-1}\mathbf{A}^T\mathbf{V}_B\mathbf{B}\mathbf{V} \quad (\text{A.15})$$

$$C_{32} = \mathbf{V}_B\mathbf{A}\mathbf{V}_A^{-1} \quad (\text{A.16})$$

$$C_{33} = -\mathbf{V}_B + \mathbf{V}_B\mathbf{A}\mathbf{V}_A^{-1}\mathbf{A}^T\mathbf{V}_B \quad (\text{A.17})$$

and the corrections to the fit parameters turn out to be

$$\Delta\vec{y} = C_{31}^T\vec{c} \quad (\text{A.18})$$

$$\Delta\vec{a} = C_{32}^T\vec{c} \quad (\text{A.19})$$

$$\Delta\vec{\lambda} = C_{33}\vec{c}. \quad (\text{A.20})$$

The variance of the fitted parameters is obtained from error propagation and one finds

$$\mathbf{V}' \begin{bmatrix} \left(\begin{array}{c} \vec{y}' \\ \vec{a}' \\ \vec{\lambda} \end{array} \right) \end{bmatrix} = \begin{pmatrix} C_{11} & C_{21}^T & 0 \\ C_{21} & C_{22} & 0 \\ 0 & 0 & -C_{33} \end{pmatrix}. \quad (\text{A.21})$$

The squared sum of residuals S can be calculate from

$$S = -\vec{\lambda}^T(\vec{c} - \mathbf{A}\Delta\vec{a}) \quad (\text{A.22})$$

and for a correct model follows a χ^2 distribution with $m - n$ degrees of freedom. For convergence two criteria are required to be fulfilled. On the one hand the change of the sum of residuals w.r.t. the previous iteration should be small

$$\frac{S(n-1) - S(n)}{\text{ndf}} < \varepsilon_S \quad (\text{A.23})$$

and on the other hand the absolute sum of the constraints should be small.

$$F = \sum_{k=1}^l |f_k(\vec{y} + \Delta\vec{y}, \vec{a} + \Delta\vec{a})| < \varepsilon_F \quad (\text{A.24})$$

Furthermore a reduction of F is required in each iteration, otherwise the size of the calculated steps $\Delta\vec{y}/\Delta\vec{a}$ is reduced by a factor of two until F decreases.

Appendix B

Calculations for a Two-Body-Decay

Some calculations for the transformation of a two-body-decay $A \rightarrow B+C$ between different reference frames are summarized. The basic idea is to relate the quantities in A's rest frame with the particle momenta in the laboratory frame. This is done in two steps. First the magnitude of the boost of A is determined and applied along an arbitrary axis. Then the resulting frame is rotated, such that the calculated B-momentum is identical to the measured one.

Formulae for the conversion of fourvectors between the different inertial frames are given for the case, that

- particle B is massless (or its mass is negligible w.r.t A,C masses and typical momenta)
- the masses of A and C are known
- the B momentum was measured in the laboratory system.

The inertial frames used in the following are:

1. Frame * ("Star"): Rest-frame of particle A
2. Frame ' ("Prime"): Frame * boosted along z-Axis, such that the momentum of B has the same magnitude as in the laboratory frame.
3. Lab-frame: Rotated w.r.t frame ', such that the B-momentum coincides with the measured one.

Fourvectors in A's rest-frame

The Metric used here is always $(+, -, -, -)$. Particle A is then given by:

$$p_A^* = \begin{pmatrix} M_A \\ 0 \\ 0 \\ 0 \end{pmatrix}$$

The momentum of the decay products can be described by the magnitude of their momentum and two angles.

- θ^* : angle w.r.t \vec{p}_A' , i.e. its direction after the boost, where the z-axis is chosen here.
- ϕ^* : angle in the plane perpendicular to \vec{p}_A'

Due to 4-momentum conservation the decay products must be back-to-back and particle B is massless.

Particle B

$$p_B^* = \begin{pmatrix} |\vec{p}_B^*| \\ |\vec{p}_B^*| \cos \phi^* \sin \theta^* \\ |\vec{p}_B^*| \sin \phi^* \sin \theta^* \\ |\vec{p}_B^*| \cos \theta^* \end{pmatrix}$$

Particle C

$$p_C^* = \begin{pmatrix} \sqrt{M_C^2 + |\vec{p}_B^*|^2} \\ -p_B^{x*} \\ -p_B^{y*} \\ -p_B^{z*} \end{pmatrix}$$

The magnitude $|\vec{p}_B^*|$ follows from energy conservation as

$$|\vec{p}_B^*| = \frac{M_A^2 - M_C^2}{2 \cdot M_A}$$

While in principle the two angles can take any value in $\cos \theta^* \in [-1, 1]$, $\phi^* \in (-\pi, \pi]$ the magnitude of the measured B momentum may restrict the range of possible $\cos \theta^*$ values. See below for a qualitative statement.

Fourvectors in Boosted Frame '

The first transformation is a boost along the z-axis. Here we need to assume a value for $\cos \theta^*$ so that we know the z- and transverse-component of the B momentum and can adjust the boost such, that the new B-momentum has the same magnitude as in the lab frame.

Momentum of B and restriction of $\cos \theta^*$

The requirement is that $|\vec{p}_B'| = |\vec{p}_B|$, the momentum in the lab-frame. Because the transverse components p_B^{x*} and p_B^{y*} remain unchanged in the boost, this relation gives two solutions for the z-component:

$$p_B^{z'} = \pm \sqrt{|\vec{p}_B|^2 - |p_B^{T'}|^2}$$

A requirement is, that $p_B^{z'}$ should be a real number which defines the range of compatible $\cos \theta^*$ values.

$$|p_B^{T'}|^2 = |\vec{p}_B^*|^2 \cdot \sin^2 \theta^* \leq |\vec{p}_B|^2$$

$$\Leftrightarrow \sin \theta^* \leq \frac{|\vec{p}_B|}{|\vec{p}_B^*|} \text{ and } \sin \theta^* \geq -\frac{|\vec{p}_B|}{|\vec{p}_B^*|}$$

For the case $|\vec{p}_B|/|\vec{p}_B^*| > 1$ this is always fulfilled and there are no limitations on θ^* . For the other case $|\vec{p}_B|/|\vec{p}_B^*| \leq 1$ however we find

$$\arcsin \frac{|\vec{p}_B|}{|\vec{p}_B^*|} \leq \theta^* \leq -\arcsin \frac{|\vec{p}_B|}{|\vec{p}_B^*|}$$

or

$$\pi - \arcsin \frac{|\vec{p}_B|}{|\vec{p}_B^*|} \leq \theta^* \leq \pi + \arcsin \frac{|\vec{p}_B|}{|\vec{p}_B^*|}$$

And with $\cos(\arcsin x) = \sqrt{1-x^2}$ we get

$$\sqrt{1 - \frac{|\vec{p}_B|^2}{|\vec{p}_B^*|^2}} \leq \cos \theta^* \leq 1$$

or

$$-1 \leq \cos \theta^* \leq -\sqrt{1 - \frac{|\vec{p}_B|^2}{|\vec{p}_B^*|^2}}$$

giving us the requirement

$$|\cos \theta^*| \geq \sqrt{1 - \frac{|\vec{p}_B|^2}{|\vec{p}_B^*|^2}}$$

Determination of the Boost

The direction of the boost is chosen along the z-Axis. The magnitude has to be determined from the magnitude of the B momentum in the lab-frame. Only the component parallel to the boost direction (i.e. p_B^z) and the energy will change:

$$p_B' = \begin{pmatrix} E_B' \\ p_B^{x'} \\ p_B^{y'} \\ p_B^{z'} \end{pmatrix} = \begin{pmatrix} \gamma E_B^* - \gamma \beta p_B^{z*} \\ p_B^{x*} \\ p_B^{y*} \\ \gamma p_B^{z*} - \gamma \beta E_B^* \end{pmatrix},$$

with $\gamma = \frac{1}{\sqrt{1-\beta^2}}$. Either of the two equations from the 1st and 4th component is quadratic in β and yields two solutions

$$\beta_{1/2} = \frac{E_B^* \cdot p_B^{z*} \pm E_B' \cdot p_B^{z'}}{E_B^{*2} + p_B^{z'2}}$$

Here the invariance of the transverse component was exploited to rewrite the invariant mass expression as

$$\begin{aligned} M_B^{*2} &= M_B'^2 \\ E_B^{*2} - p_B^{T*2} - p_B^{z*2} &= E_B'^2 - p_B^{T'2} - p_B^{z'2} \\ E_B^{*2} + p_B^{z'2} &= E_B'^2 + p_B^{z*2} \end{aligned}$$

and this expression was used to simplify the result. Note, that the two solutions for $p_B^{z'}$ lead to only two different solutions for β .

From a physics point of view one could just choose the smaller $|\beta|$ value, because smaller boosts are more likely to appear in heavy particle production.

It can be shown that the absolute smaller value is always given by

$$\beta = \frac{E_B^* \cdot |p_B^{z*}| - E_B' \cdot |p_B^{z'}|}{E_B^{*2} + p_B^{z'2}} \cdot \text{sgn}(\cos \theta^*),$$

and that then $p_B^{z'}$ has the same sign as $\cos \theta^*$ and therefore also as p_B^{z*} .

Momenta of A,C

Knowing the boost and its direction one can just apply it to the two particles A,C to obtain their fourvector in the "prime" frame.

$$\begin{aligned} p_A' &= \begin{pmatrix} E_A' \\ p_A^{x'} \\ p_A^{y'} \\ p_A^{z'} \end{pmatrix} = \begin{pmatrix} \gamma E_A^* - \gamma \beta p_A^{z*} \\ p_A^{x*} \\ p_A^{y*} \\ \gamma p_A^{z*} - \gamma \beta E_A^* \end{pmatrix} \\ p_C' &= \begin{pmatrix} E_C' \\ p_C^{x'} \\ p_C^{y'} \\ p_C^{z'} \end{pmatrix} = \begin{pmatrix} \gamma E_C^* - \gamma \beta p_C^{z*} \\ p_C^{x*} \\ p_C^{y*} \\ \gamma p_C^{z*} - \gamma \beta E_C^* \end{pmatrix} \end{aligned}$$

The fourvectors of B and C can again be expressed via parameters like $p^{T'}$, $\cos \theta'$ and ϕ' in this new frame. Obviously the $\cos \theta'$ values is given by

$$\cos \theta' = \frac{\vec{p}_{B'} \cdot \vec{p}_{A'}}{|\vec{p}_{B'}| \cdot |\vec{p}_{A'}|} = \frac{p_{B'}^z \cdot p_{A'}^z}{|\vec{p}_{B'}| \cdot |p_{A'}^z|} = \pm \frac{p_{B'}^z}{|\vec{p}_{B'}|}$$

Rotation to the Lab-System

The last step is to rotate the boosted system ' to the lab frame, such that the 3-momentum vector of B has its components equal to the measured ones.

There is not a unique solution to this problem because an arbitrary rotation of a coordinate system has 4 parameters.

- 3 for the direction of the rotation axis
- 1 for the rotation angle.

So in our case, where we have 3 equations from the momentum components, one degree of freedom remains. In the way the rotation will be done, this degree of freedom just corresponds to a free choice of our ϕ' parameter, as will be shown below. We anyway have to choose or dice this variable in our usecase, so this is no further problem.

The procedure is the following. On the one hand we start from the ' system:

1. Rotate the system ' around the z-axis, such that $\vec{p}_{B'}$ lies in the x-z plane
2. Rotate the system around the new y-axis, such that $\vec{p}_{B'}$ lies along the new (positive) z-axis

The matrices of these rotations will be labelled R_1 and R_2 , respectively. Note that the first rotation does not change $\vec{p}_{A'}$ and the second one rotates it into the x-z-plane, which will be shown explicitly below.

On the other hand we do the same, starting from the lab-system:

1. Rotate the system around the z-axis, such that \vec{p}_B lies in the x-z plane
2. Rotate the system around the new y-axis, such that \vec{p}_B lies along the new (positive) z-axis

The matrices of these rotations will be labelled S_1 and S_2 , respectively.

Rotation Matrices

Here matrices describing the above rotations are given. I use a different (generic) notation for the momentum now. First we rotate the the "prime" system, writing the momentum components of B as $\vec{v} = (v_1, v_2, v_3)^T$. The rotation around the z-axis can be written as:

$$\vec{v}' = R_1 \cdot \vec{v} = \begin{pmatrix} \cos \alpha_1 & \sin \alpha_1 & 0 \\ -\sin \alpha_1 & \cos \alpha_1 & 0 \\ 0 & 0 & 1 \end{pmatrix} \cdot \begin{pmatrix} v_1 \\ v_2 \\ v_3 \end{pmatrix} = \begin{pmatrix} v'_1 \\ 0 \\ v'_3 \end{pmatrix}$$

From the second component we get the equation

$$-\sin \alpha_1 \cdot v_1 + \cos \alpha_1 \cdot v_2 = 0$$

and the solution for the angle

$$\alpha_1 = \arctan \frac{v_2}{v_1}$$

The next rotation around the y-axis looks similar

$$\vec{v}'' = R_2 \cdot \vec{v}' = \begin{pmatrix} \cos \alpha_2 & 0 & \sin \alpha_2 \\ 0 & 1 & 0 \\ -\sin \alpha_2 & 0 & \cos \alpha_2 \end{pmatrix} \cdot \begin{pmatrix} v'_1 \\ v'_2 \\ 0 \end{pmatrix} = \begin{pmatrix} 0 \\ 0 \\ v''_3 \end{pmatrix}$$

and from the third component we get the rotation angle as

$$\alpha_2 = \arctan -\frac{v'_1}{v'_3}$$

Then these two rotations can be combined by multiplying the matrices $R_{21} = R_2 \cdot R_1$. Inserting the solutions for $\alpha_{1/2}$ and using the relations $\sin(\arctan x) = \frac{x}{\sqrt{1+x^2}}$ and $\cos(\arctan x) = \frac{1}{\sqrt{1+x^2}}$ the combined matrix becomes

$$R_{21} = \begin{pmatrix} \frac{v_1 v_3}{v \cdot \sqrt{v_1^2 + v_2^2}} & \frac{v_2 v_3}{v \cdot \sqrt{v_1^2 + v_2^2}} & -\frac{\sqrt{v_1^2 + v_2^2}}{v} \\ -\frac{v_2}{\sqrt{v_1^2 + v_2^2}} & \frac{v_1}{\sqrt{v_1^2 + v_2^2}} & 0 \\ \frac{v_1}{v} & \frac{v_2}{v} & \frac{v_3}{v} \end{pmatrix}$$

with $v = |\vec{v}| = \sqrt{v_1^2 + v_2^2 + v_3^2}$. (In this parametrization $v_1^2 + v_2^2$ must be non-zero, which means $|\cos \theta^*| \neq 1$)

Starting from the lab-frame with a vector $\vec{w} = (w_1, w_2, w_3)^T$ one gets an equivalent result

for the two-rotation-matrix S_{21} . We are interested in the rotation from \vec{v} to \vec{w} , that means we need the inverse rotation of this second step

$$S_{21}^{-1} = S_{21}^T = \begin{pmatrix} \frac{w_1 w_3}{w \cdot \sqrt{w_1^2 + w_2^2}} & -\frac{w_2}{\sqrt{w_1^2 + w_2^2}} & \frac{w_1}{w} \\ \frac{w_2 w_3}{w \cdot \sqrt{w_1^2 + w_2^2}} & \frac{w_1}{\sqrt{w_1^2 + w_2^2}} & \frac{w_2}{w} \\ -\frac{\sqrt{w_1^2 + w_2^2}}{w} & 0 & \frac{w_3}{w} \end{pmatrix}$$

The Additional Degree of Freedom

After these two operations both B-vectors lie along the z-axis in their own coordinate-system. So actually we know how to transform B from the "prime" to the lab frame, i.e. with the combined rotations

$$\vec{w} = S_{21}^T \cdot R_{21} \cdot \vec{v}$$

Next we take a look at the behaviour of the A (and C) momenta. Therefore we choose a parametrization:

$$\vec{p}_B' = |\vec{p}_B'| \cdot \begin{pmatrix} \sin \theta' \cos \phi' \\ \sin \theta' \sin \phi' \\ \cos \theta' \end{pmatrix} \hat{=} \begin{pmatrix} v1 \\ v2 \\ v3 \end{pmatrix}$$

and apply the rotation R_{21} to A

$$\begin{aligned} R_{21} \cdot \vec{p}_A' &= \begin{pmatrix} \cos \theta' \cos \phi' & \cos \theta' \sin \phi' & -\sin \theta' \\ -\sin \phi' & \cos \phi' & 0 \\ \sin \theta' \cos \phi' & \sin \theta' \sin \phi' & \cos \theta' \end{pmatrix} \cdot \begin{pmatrix} 0 \\ 0 \\ p_A^{z'} \end{pmatrix} \\ &= \begin{pmatrix} -\sin \theta' \\ 0 \\ \cos \theta' \end{pmatrix} \cdot p_A^{z'} \end{aligned}$$

The vector of A now lies in the x-z plane and so does the momentum of C, due to momentum conservation. (One can also calculate it using the above formulae).

$$\vec{p}_C' = \vec{p}_A' - \vec{p}_B' = \begin{pmatrix} -\sin \theta' \cdot p_A^{z'} \\ 0 \\ \cos \theta' \cdot p_A^{z'} - |\vec{p}_B'| \end{pmatrix}$$

Note that all three momentum vectors are independent of any former choice of the azimuthal angle ϕ^* or ϕ' , which is an effect resulting from the choice of the A momentum as first rotation axis.

Now an angle ϕ'' , describing a rotation around the z-axis (which is now identical to the B-momentum direction) can be used to parametrize the additional degree of freedom. From a physics point of view it is important that it follows the same (flat) distribution as ϕ^* in the rest-frame of A.

Such a rotation does not affect the angle between B and A or B and C and therefore the invariant masses are unchanged. However, it changes A's (and C's) orientation in space and leads to different transverse/longitudinal components of their fourvectors in the lab-frame. This additional rotation is included via a matrix P

$$P = \begin{pmatrix} \cos \phi'' & \sin \phi'' & 0 \\ -\sin \phi'' & \cos \phi'' & 0 \\ 0 & 0 & 1 \end{pmatrix}$$

and the entire rotation to the lab-system for any momentum \vec{x}' becomes:

$$\vec{x} = S_{21}^T \cdot P \cdot R_{21} \cdot \vec{x}'.$$

Appendix C

Additional Pull Distributions

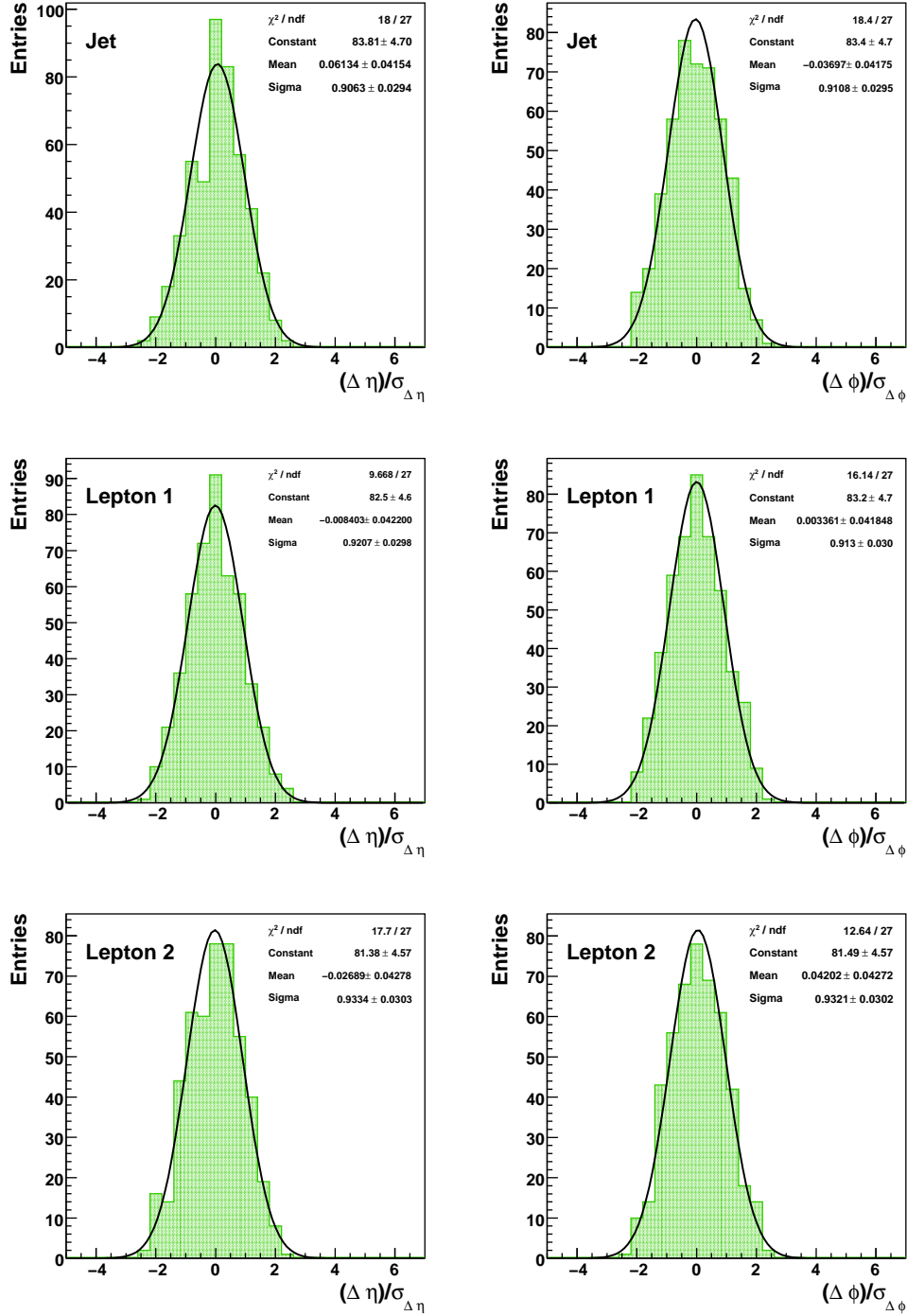


Figure C.1.: Pull distributions with fitted gaussian for jet and lepton η and ϕ in Toy Monte Carlo events with $\text{Prob}(\chi^2) > 0.05$. The correct lepton and jet positions are used.

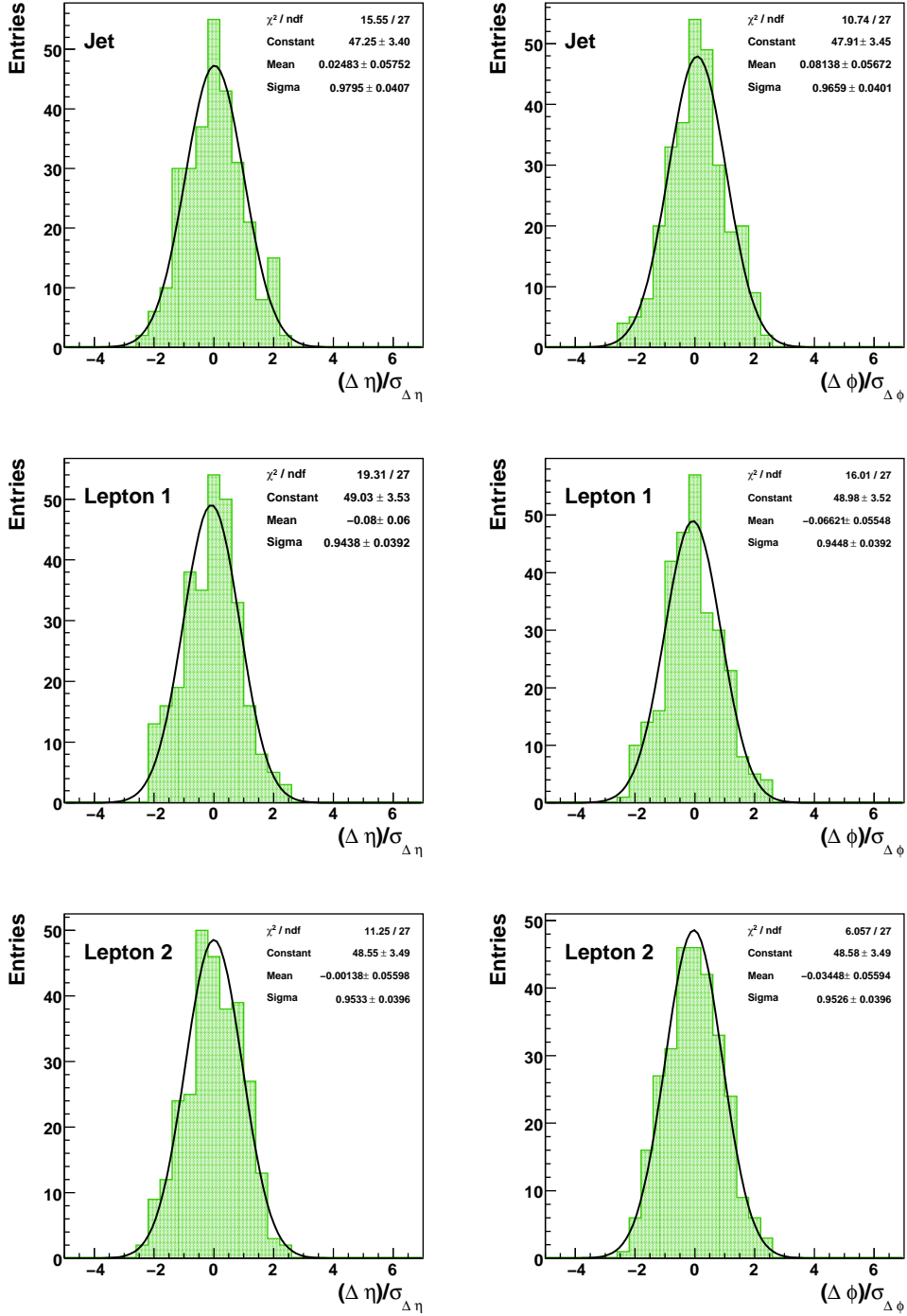


Figure C.2.: Pull distributions with fitted gaussian for jet and lepton η and ϕ in detector simulation sample with $\text{Prob}(\chi^2) > 0.05$. The correct lepton and jet positions are used.

Danksagung

Ich danke Prof. Peter Schleper für die Möglichkeit diese Arbeit in seiner Arbeitsgruppe anfertigen zu können, für seine Diskussionsbereitschaft, Unterstützung und Motivation.

Ebenfalls danke ich Prof. Johannes Haller und Dr. Philip Bechtle für ihre Mitwirkung als Gutachter der Dissertation und Disputation.

Christian Sander gilt mein besonderer Dank für seine jahrelange, geduldige Anleitung und Betreuung bei der Erstellung dieser Arbeit.

Ich bedanke mich bei Christian, Christian, Friederike, Georg, Gero, Gordon, Hartmut, Holger, Jan, Julia, Kolja, Matthias, Michael, Niklas, Roger, Sebastian, Torben, Ulla, Uwe und allen anderen (ehemaligen) Mitgliedern der Arbeitsgruppe für sehr schöne Jahre am Institut, gute Zusammenarbeit, hart umkämpfte Partien am Kicker, vollen Einsatz auf dem Beachvolleyballplatz, spannende Fußballabende und leckeres Grillgut.

Insbesondere sage ich Danke an meine Bürokollegen während des letzten Jahres, Julia, Jan und Ulla, für Ablenkung und Ermunterung in den richtigen Momenten.

Nicht vergessen möchte ich Lena, meine Familie und meine Freunde, die mir immer Rückhalt gegeben haben.

Bibliography

- [1] S. P. Martin, *A Supersymmetry Primer*, [hep-ph/9709356].
- [2] I. J. R. Aitchison, *Supersymmetry in particle physics: An elementary introduction*, . SLAC-R-865.
- [3] M. J. Herrero, *The standard model*, [hep-ph/9812242].
- [4] B. Mura, *Determination of Neutralino Masses with the CMS Experiment*, Diploma thesis, RWTH Aachen University, 2006, [<http://web.physik.rwth-aachen.de/~feld/RWTH/Diplomarbeiten/Mura.pdf>].
- [5] M. K. Trenkel, *Phenomenology of supersymmetric particle production processes at the LHC*. PhD thesis, Technische Universität München, 2009. [<http://nbn-resolving.de/urn/resolver.pl?urn:nbn:de:bvb:91-diss-20090730-796678-1-6>].
- [6] S. L. Glashow, *Partial Symmetries of Weak Interactions*, Nucl. Phys. **22** (1961) 579–588.
- [7] S. Weinberg, *A Model of Leptons*, Phys. Rev. Lett. **19** (1967) 1264–1266.
- [8] A. Salam, *Weak and Electromagnetic Interactions*, . Originally printed in *Svartholm: Elementary Particle Theory, Proceedings Of The Nobel Symposium Held 1968 At Lerum, Sweden*, Stockholm 1968, 367-377.
- [9] S. L. Glashow, J. Iliopoulos, and L. Maiani, *Weak Interactions with Lepton-Hadron Symmetry*, Phys. Rev. **D2** (1970) 1285–1292.
- [10] R. K. Ellis, W. J. Stirling, and B. R. Webber, *QCD and collider physics*, Camb. Monogr. Part. Phys. Nucl. Phys. Cosmol. **8** (1996) 1–435.
- [11] P. W. Higgs, *Broken Symmetries and the masses of Gauge Bosons*, Phys. Rev. Lett. **13** (1964) 508–509.
- [12] P. W. Higgs, *Spontaneous Symmetry Breakdown without Massless Bosons*, Phys. Rev. **145** (1966) 1156–1163.
- [13] F. Englert and R. Brout, *Broken Symmetry and the Mass of Gauge Vector Mesons*, Phys. Rev. Lett. **13** (1964) 321–322.
- [14] T. W. B. Kibble, *Symmetry breaking in non-Abelian gauge theories*, Phys. Rev. **155** (1967) 1554–1561.

- [15] The ALEPH, DELPHI, L3, OPAL, SLD Collaborations, the LEP Electroweak Working Group, and the SLD Electroweak and Heavy Flavour Groups, *Precision Electroweak Measurements on the Z Resonance*, Phys. Rept. **427** (2006) 257.
- [16] **Particle Data Group** Collaboration, C. Amsler *et. al.*, *Review of particle physics*, Phys. Lett. **B667** (2008) 1.
- [17] N. Cabibbo, *Unitary Symmetry and Leptonic Decays*, Phys. Rev. Lett. **10** (1963) 531–533.
- [18] M. Kobayashi and T. Maskawa, *CP Violation in the Renormalizable Theory of Weak Interaction*, Prog. Theor. Phys. **49** (1973) 652–657.
- [19] R. N. Mohapatra *et. al.*, *Theory of neutrinos: A white paper*, Rept. Prog. Phys. **70** (2007) 1757–1867.
- [20] T. Hambye and K. Riesselmann, *Matching conditions and Higgs mass upper bounds revisited*, Phys. Rev. **D55** (1997) 7255–7262.
- [21] **LEP Working Group for Higgs boson searches** Collaboration, R. Barate *et. al.*, *Search for the standard model Higgs boson at LEP*, Phys. Lett. **B565** (2003) 61–75.
- [22] **CDF and D0** Collaboration, *Combined CDF and D0 Upper Limits on Standard Model Higgs- Boson Production with up to 6.7 fb^{-1} of Data*, [arXiv:1007.4587].
- [23] **WMAP** Collaboration, J. Dunkley *et. al.*, *Five-Year Wilkinson Microwave Anisotropy Probe (WMAP) Observations: Likelihoods and Parameters from the WMAP data*, Astrophys. J. Suppl. **180** (2009) 306–329.
- [24] V. C. Rubin, N. Thonnard, and W. K. Ford, Jr., *Rotational properties of 21 SC galaxies with a large range of luminosities and radii, from NGC 4605 / $R = 4 \text{ kpc}$ / to UGC 2885 / $R = 122 \text{ kpc}$ /*, Astrophys. J. **238** (1980) 471.
- [25] J. Wess and B. Zumino, *A Lagrangian Model Invariant Under Supergauge Transformations*, Phys. Lett. **B49** (1974) 52.
- [26] J. Wess and B. Zumino, *Supergauge Transformations in Four-Dimensions*, Nucl. Phys. **B70** (1974) 39–50.
- [27] **CDF** Collaboration, T. Aaltonen *et. al.*, *Inclusive Search for Squark and Gluino Production in $p\bar{p}$ Collisions at $\sqrt{s} = 1.96\text{-TeV}$* , Phys. Rev. Lett. **102** (2009) 121801.
- [28] **D0** Collaboration, V. M. Abazov *et. al.*, *Search for squarks and gluinos in events with jets and missing transverse energy using 2.1 fb^{-1} of $p\bar{p}$ collision data at $\sqrt{s} = 1.96\text{-TeV}$* , Phys. Lett. **B660** (2008) 449–457.
- [29] *LEP SUSY Workinggroup: ALEPH, DELPHI, L3, and OPAL Collaborations*. [<http://lepsusy.web.cern.ch/lepsusy>].
- [30] J. L. Feng, J.-F. Grivaz, and J. Nachtman, *Searches for Supersymmetry at High-Energy Colliders*, Rev. Mod. Phys. **82** (2010) 699–727.
- [31] **CMS** Collaboration, G. L. Bayatian *et. al.*, *CMS technical design report, volume II: Physics performance*, J. Phys. **G34** (2007) 995–1579.

-
- [32] **The ATLAS** Collaboration, G. Aad *et. al.*, *Expected Performance of the ATLAS Experiment - Detector, Trigger and Physics*, [arXiv:0901.0512].
- [33] A. Duperrin, *Review of searches for Higgs bosons and beyond the standard model physics at the Tevatron*, Eur. Phys. J. **C59** (2009) 297–334.
- [34] CMS Collaboration.
[<https://twiki.cern.ch/twiki/bin/view/CMSPublic/PhysicsResultsSUS>], Original publications are linked from the webpage.
- [35] L. Evans, (ed.) and P. Bryant, (ed.), *LHC Machine*, JINST **3** (2008) S08001.
- [36] D. Acosta, M. Della Negra, L. Foà, A. Hervé, and A. Petrilli, *CMS physics: Technical Design Report*, CERN-LHCC-2006-001 (2006).
- [37] **CMS** Collaboration, R. Adolphi *et. al.*, *The CMS experiment at the CERN LHC*, JINST **3** (2008) S08004.
- [38] G. L. Bayatyan, M. Della Negra, Foà, A. Hervé, and A. Petrilli, *CMS: The computing project. Technical design report*, . CERN-LHCC-2005-023.
- [39] I. Bird, (ed.) *et. al.*, *LHC computing Grid. Technical design report*, . CERN-LHCC-2005-024.
- [40] V. Chetluru, F. Pandolfi, P. Schieferdecker, and M. Zielinski, *Jet Reconstruction Performance at CMS*, CMS AN **2009/067** (2009).
- [41] **CMS** Collaboration, *Particle-flow event reconstruction in cms and performance for jets, taus, and met*, CMS-PAS-PFT-09-001 (Apr, 2009).
- [42] M. Cacciari, G. P. Salam, and G. Soyez, *The anti-kt jet clustering algorithm*, JHEP **04** (2008) 063.
- [43] **CMS** Collaboration, *Plans for Jet Energy Corrections at CMS*, CMS-PAS-JME-07-002 (Jul, 2008).
- [44] *Jet Energy Resolution in CMS at $\sqrt{s}=7$ TeV*, CMS-PAS-JME-10-014 (2011).
- [45] H. Held, P. Schieferdecker, and M. Voutilainen, *Update of the Measurement of the Jet p_T Resolution in $\sqrt{s} = 7$ TeV Collision Data with the Asymmetry Method*, CMS AN **2010/0371** (2011).
- [46] W. Adam, S. Baffioni, F. Beaudette, D. Benedetti, C. Broutin, D. Chamont, C. Charlot, E. DiMarco, D. Futyan, S. Harper, D. Lelas, A. Martelli, P. Meridiani, M. Pioppi, I. Puljak, D. Sabes, R. Salerno, M. Sani, C. Seez, Y. Sirois, P. Vanlaer, and D. Wardrope, *Electron Reconstruction in CMS*, CMS AN **2009/164** (2009).
- [47] S. Baffioni, F. Beaudette, D. Benedetti, J. Branson, G. Daskalakis, E. D. Marco, C. Campagnari, C. Charlot, S. Harper, P. Kalavase, J. Keller, D. Lelas, P. Meridiani, M. Pieri, I. Puljak, R. Ranieri, N. Rompotis, C. Rovelli, R. Salerno, M. Sani, C. Seez, Y. Sirois, Y. Tu, and A. Yagil, *Electron Identification in CMS*, CMS AN **2009/178** (2009).
- [48] J. Branson, M. Gallinaro, P. Ribeiro, R. Salerno, and M. Sani, *A cut based method for electron identification in CMS*, CMS AN **2008/082** (2008).

- [49] G. Abbiendi, N. Adam, J. Alcaraz, N. Amapane, E. Antillon, R. Bellan, I. Belotelov, I. B. C. Campagnari, T. Cox, A. Everett, A. Grelli, J. Goh, V. Halyo, A. Hunt, E. James, P. Kalavase, S. Kao, M. Konecki, D. Kovalskyi, V. Krutelyov, C. Liu, P. Martinez, D. Miller, M. Mulders, N. Neumeister, D. Pagano, J. Pivarski, J. Ribnik, S. Stoynev, P. Traczyk, D. Trocino, J. Vlimant, and R. Wilkinson, *Muon Reconstruction in the CMS Detector*, CMS AN **2008/097** (2008).
- [50] M. Mulders, I. Bloch, E. James, A. Everett, D. Barge, C. Campagnari, P. Kalavase, V. Krutelyov, D. Kovalskyi, J. Ribnik, and N. Amapane, *Muon Identification in CMS*, CMS AN **2008/082** (2008), no. 098.
- [51] T. Sjostrand *et. al.*, *High-energy physics event generation with PYTHIA 6.1*, Comput. Phys. Commun. **135** (2001) 238–259.
- [52] M. L. Mangano, M. Moretti, F. Piccinini, R. Pittau, and A. D. Polosa, *ALPGEN, a generator for hard multiparton processes in hadronic collisions*, JHEP **07** (2003) 001.
- [53] T. Gleisberg *et. al.*, *Event generation with SHERPA 1.1*, JHEP **02** (2009) 007.
- [54] M. Dobbs and J. B. Hansen, *The HepMC C++ Monte Carlo event record for High Energy Physics*, Comput. Phys. Commun. **134** (2001) 41–46.
- [55] **GEANT4** Collaboration, S. Agostinelli *et. al.*, *GEANT4: A simulation toolkit*, Nucl. Instrum. Meth. **A506** (2003) 250–303.
- [56] **CMS** Collaboration, D. Orbak, *Fast simulation of the CMS detector*, J. Phys. Conf. Ser. **219** (2010) 032053.
- [57] N. Arkani-Hamed, G. L. Kane, J. Thaler, and L.-T. Wang, *Supersymmetry and the LHC inverse problem*, JHEP **08** (2006) 070.
- [58] R. Lafaye, T. Plehn, and D. Zerwas, *SFITTER: SUSY parameter analysis at LHC and LC*, [hep-ph/0404282].
- [59] P. Bechtle, K. Desch, M. Uhlenbrock, and P. Wienemann, *Constraining SUSY models with Fittino using measurements before, with and beyond the LHC*, Eur. Phys. J. **C66** (2010) 215–259.
- [60] *Mastercode Homepage*. [<http://mastercode.web.cern.ch/mastercode/>].
- [61] O. Buchmueller, R. Cavanaugh, D. Colling, A. De Roeck, M. Dolan, *et. al.*, *Frequentist Analysis of the Parameter Space of Minimal Supergravity*, Eur.Phys.J. **C71** (2011) 1583.
- [62] G. Brooijmans *et. al.*, *New Physics at the LHC. A Les Houches Report: Physics at TeV Colliders 2009 - New Physics Working Group*, [arXiv:1005.1229].
- [63] A. J. Barr and C. G. Lester, *A Review of the Mass Measurement Techniques proposed for the Large Hadron Collider*, [arXiv:1004.2732].
- [64] I. Hinchliffe, F. E. Paige, M. D. Shapiro, J. Soderqvist, and W. Yao, *Precision SUSY measurements at CERN LHC*, Phys. Rev. **D55** (1997) 5520–5540.
- [65] D. R. Tovey, *Measuring the SUSY mass scale at the LHC*, Phys. Lett. **B498** (2001) 1–10.

-
- [66] C. G. Lester and D. J. Summers, *Measuring masses of semiinvisibly decaying particles pair produced at hadron colliders*, Phys. Lett. **B463** (1999) 99–103.
- [67] W. S. Cho, K. Choi, Y. G. Kim, and C. B. Park, *Gluino Stransverse Mass*, Phys. Rev. Lett. **100** (2008) 171801.
- [68] H. Bachacou, I. Hinchliffe, and F. E. Paige, *Measurements of masses in SUGRA models at CERN LHC*, Phys. Rev. **D62** (2000) 015009.
- [69] B. C. Allanach, C. G. Lester, M. A. Parker, and B. R. Webber, *Measuring sparticle masses in non-universal string inspired models at the LHC*, JHEP **09** (2000) 004.
- [70] B. K. Gjelsten, D. J. Miller, 2, and P. Osland, *Measurement of SUSY masses via cascade decays for SPS 1a*, JHEP **12** (2004) 003.
- [71] M. M. Nojiri, G. Polesello, and D. R. Tovey, *A hybrid method for determining SUSY particle masses at the LHC with fully identified cascade decays*, JHEP **05** (2008) 014.
- [72] I.-W. Kim, *Algebraic Singularity Method for Mass Measurement with Missing Energy*, Phys. Rev. Lett. **104** (2010) 081601.
- [73] CMS Collaboration, *Discovery potential and measurement of a dilepton mass edge in SUSY events at sqrt s = 10 TeV*, CMS PAS SUS-09-002 (Jul, 2009).
- [74] H.-C. Cheng, D. Engelhardt, J. F. Gunion, Z. Han, and B. McElrath, *Accurate Mass Determinations in Decay Chains with Missing Energy*, Physical Review Letters **100** (2008) 252001.
- [75] B. Webber, *Mass determination in sequential particle decay chains*, JHEP **09** (2009) 124.
- [76] C. Autermann, B. Mura, C. Sander, H. Schettler, and P. Schleper, *Determination of supersymmetric masses using kinematic fits at the LHC*, [arXiv:0911.2607].
- [77] B. C. Allanach *et. al.*, *The Snowmass points and slopes: Benchmarks for SUSY searches*, Eur. Phys. J. **C25** (2002) 113–123.
- [78] M. Battaglia *et. al.*, *Proposed post-LEP benchmarks for supersymmetry*, Eur. Phys. J. **C22** (2001) 535–561.
- [79] M. Battaglia *et. al.*, *Updated post-WMAP benchmarks for supersymmetry*, Eur. Phys. J. **C33** (2004) 273–296.
- [80] W. Beenakker, R. Hopker, and M. Spira, *PROSPINO: A program for the PROduction of Supersymmetric Particles In Next-to-leading Order QCD*, [hep-ph/9611232].
- [81] B. C. Allanach, S. Kraml, and W. Porod, *Theoretical uncertainties in sparticle mass predictions from computational tools*, JHEP **03** (2003) 016.
- [82] G. Belanger, S. Kraml, and A. Pukhov, *Comparison of SUSY spectrum calculations and impact on the relic density constraints from WMAP*, Phys. Rev. **D72** (2005) 015003.
- [83] H.-C. Cheng, J. F. Gunion, Z. Han, G. Marandella, and B. McElrath, *Mass determination in SUSY-like events with missing energy*, JHEP **0712** (2007) 076.

- [84] M. M. Nojiri, K. Sakurai, and B. R. Webber, *Reconstructing particle masses from pairs of decay chains*, JHEP **06** (2010) 069.
- [85] A. Djouadi, M. M. Muhlleitner, and M. Spira, *Decays of Supersymmetric Particles: the program SUSY-HIT (SUspect-SdecaY-Hdecay-InTerface)*, ActaPhys.Polon. **B38** (2007) 635–644.
- [86] V. Blobel and E. Lohrmann, *Statistische und numerische Methoden der Datenanalyse*. Teubner, 1998.
- [87] J. D’Hondt, S. Lowette, O. Buchmuller, S. Cucciarelli, F.-P. Schilling, M. Spiropulu, S. P. Mehdibadi, D. Benedetti, and L. Pape, *Fitting of Event Topologies with External Kinematic Constraints in CMS*, CMS AN **2005/025** (2005).
- [88] P. Schleper, *Private communication*. .